The First Direct Limit on the t Quark Lifetime

A dissertation presented
by

Ayana Tamu Holloway

to
The Department of Physics
in partial fulfillment of the requirements
for the degree of
Doctor of Philosophy
in the subject of

Physics

Harvard University
Cambridge, Massachusetts
May 2006

Thesis advisor Author

M.E.B. Franklin **Ayana Tamu Holloway**

The First Direct Limit on the t Quark Lifetime

Abstract

This dissertation presents the first direct limit on the t quark lifetime, measured in $t\bar{t}$ pair production candidate events from a 318 pb^{-1} sample of $p + \bar{p}$ collisions recorded by the Collider Detector at Fermilab (CDF). Candidate events are identified by a leptonically decaying $W^{\pm}$ boson and three or more jets, at least one of which contains a secondary vertex. In each event we measure the transverse track-to-beam displacement (impact parameter) of the lepton from the $W^{\pm}$ decay, and compare the distribution to templates constructed from $t\bar{t}$ event simulations with a variable t lifetime. Anticipated background distributions are measured with a combination of Monte Carlo event simulation and control samples, and included in the templates.

We determine the following limits:

$$c\tau_t < 52.5\mu\text{m} \;@\, 95\% \text{ C.L.}$$

$$c\tau_t < 43.5\mu\text{m} \;@\, 90\% \text{ C.L.}$$

We thus conclude that the top mean lifetime is less than 145 fs (175 fs) at 90% (95%) C.L.

Contents

List of Figures

List of Tables

Acknowledgments

I am grateful to my family, especially my parents Russell and Karla, for so much loving and patient support. Their courageous spirits through tragedy and adversity have been my example, and their celebrations and joyful traditions have been my refuge. I hope my life and career reflect their values as clearly as theirs reflect the virtues and principles of the families that raised them.

Besides thanking Melissa for her confidence in me and for everything she has taught me, I should take this opportunity to express my admiration for her keen perspective on physics, her strength, and her sensitivity to her students' interests and needs. I am especially proud to claim her as a mentor and a friend.

At Fermilab I was lucky to have friends who were also inspired teachers and role models, including Aseet Mukherjee, Michael Schmitt, Jaco Konigsberg, Robin Erbacher, and the Quiggs. I will always remember the kindness of Kris Chaisanguantham, Tomasso Dorigo, and Maria Spiropulu during the summer of 1999. Abraham Gallas, Kevin Burkett, Stephen Bailey, Carter Hall, and Robyn Madrak must also be mentioned by name for the funny, friendly, and talented people that they are.

I was also lucky to return "home" to the friendly community at HEPL, lately known as LaPaPhyCo. George and Robyn made it embarrassingly easy and fun to be a graduate student there. Joao did his best to compensate for this, but mostly managed to teach me a lot about being a physicist. I owe Andy and Alexey special thanks for inspiring this work. And I owe thanks, loyalty, and Spa cookies to everyone who shared the attic with me, but especially Ingyin, Daniel, and Sal.

This dissertation – and most of what I accomplished before starting it – would not be possible without the loving companionship of my partner Javier. I thank him

for so many things: his perceptive wisdom, his friendship and humor, his care and concern, his wielding of the *chinche* hammer, his doorway dancing, his chicken soups and smoked duck wings, and his brilliant example.

For Bem Kayin.

Chapter 1

Introduction

In this thesis we describe the first direct measurement of the top (t) quark lifetime, performed with the Collider Detector at Fermilab (CDF) at the Tevatron collider. This measurement addresses two important hypotheses of contemporary high-energy physics: the interpretation of the top quark candidates observed in Tevatron collisions as the weak isospin partners of b quarks, and the prediction of the standard theory of elementary particle interactions that $\tau_t < 10^{-24}$ s. Our measurement, $\tau_t < 1.8 \times 10^{-13}$ s, demonstrates that the lifetime of top quark candidates produced in $p+\bar{p}$ interactions is consistent with that of theoretical t quarks.

1.1 Making and finding top

The story of t begins in the early 1970s, when the idea that quarks come in *pairs* was first introduced [1]. Only three quarks (u, d, and s) were known at the time, and the subsequent discovery of the predicted c quark was convincing validation of the theory [2]. When the b quark was discovered in 1977 [3], it thus implied the existence of yet another quark, the t.

Top was finally detected in experiments at the Fermilab Tevatron in 1995 by the CDF and DØ collaborations [4]. At the contemporary Tevatron, protons accelerated to 980 GeV are directed by magnetic fields to collide with antiprotons accelerated to the same energy. These collisions take place at the center of the CDF and DØ detectors, so that the properties of the particles produced in the reaction can be recorded by various instruments. In a very small fraction of the proton-antiproton collisions, constituents of the proton and antiproton annihilate and pairs of top quarks are produced. This process is depicted schematically in Figure 1.1.

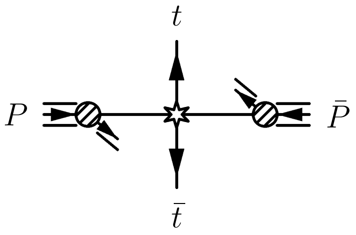

Figure 1.1: Schematic diagram of t and $\bar{t}$ quarks being produced in a proton-antiproton collision.

According to our theoretical understanding, when each t quark decays, it almost always produces a $W^{\pm}$ boson and a b quark. The latter quickly forms a *jet* of nearly collinear particles in a narrow cone. The $W^{\pm}$ boson can decay in many ways: *leptonically* to an electron, muon or tau lepton and a neutrino, or *hadronically* to a pair of quarks which also form jets. Top quark candidates were first found by searching for $W^{\pm}$ bosons decaying to electrons or muons, produced in association with jets. Now top quarks are reconstructed with every kind of $W^{\pm}$ decay.

Both CDF and DØ have made several measurements of the production rate of t

quark pairs in $p\bar{p}$ collisions. The most precise measurements generally use the same event topology used to discover t: events with electrons or muons and multiple jets. The experiments have also studied the relative probability of different decay modes in top pair events, and the polarization of the $W^{\pm}$ produced in top decay. So far none of these measurements conflict with the claim that the top candidate events at the Tevatron represent the pair-production of a theoretical t quark. Theoretical calculations also predict the probability of producing t or $\bar{t}$ quarks alone via a weak interaction between quarks in the proton. This process is very rare and has never been observed, so the strength of the weak interaction for t quarks has not yet been experimentally verified.

1.2 Is the lifetime short?

An elementary particle like the top is identified by its intrinsic quantum numbers and its interactions. The probability that a particle decays is generally increased by each kind of interaction it participates in, as long as that interaction enables a decay that conserves energy. This makes measuring the lifetime of an elementary particle a good way to identify it, since this lifetime is simply the inverse of the probability that it decays. If the current theory of particle interactions is correct about the number of quarks and their weak interactions, the top quark lifetime cannot be longer than 10^{-24} s. This extremely short lifetime cannot be observed at the Tevatron by directly measuring time intervals or flight distances, which is the method used in this dissertation. Hence the result of this experiment, which is consistent with zero lifetime, does not contradict the standard theory.

Simple extensions to the standard model in which there are more than six species of quarks can accommodate top lifetimes as long as 10^{-22} s. These lifetimes are still very short and do not correspond to top flight distances which could be distinguished from zero with the experimental apparatus used in this measurement. In fact, if the data were inconsistent with zero top lifetime, the more natural explanation would either be an impostor particle which we have mistaken for the top quark, or the creation of heavier, long-lived particles decaying to top quarks. These scenarios are also unexpected, but easier to reconcile with the overwhelmingly successful existing model.

1.3 Detecting “large” top lifetimes

The top quark production process depicted in Figure 1.1 occurs at one geometric point within the CDF detector, termed the collision point. The t quarks subsequently decay, each producing a $W^{\pm}$ boson and a jet with very high energies. The velocity of the top quark in the laboratory, in units of the speed of light (c), averages around 0.6 c, while the average $W^{\pm}$ velocity exceeds 0.7 c and the much lighter b typically travels faster than 0.99 c. The $W^{\pm}$ average lifetime is formally 7×10^{-25} s – it decays where it is produced, while the b quark typically decays later, after traveling a few millimeters in the laboratory. This process is shown in Figure 1.2. Because few known interactions besides top quark production create pairs of $W^{\pm}$ bosons and b quarks, we can use these “signatures” to identify collisions in which t quarks were produced, and study the decay positions of particles in these events.

We choose events in which one $W^{\pm}$ decays to a single lepton and a neutrino. The

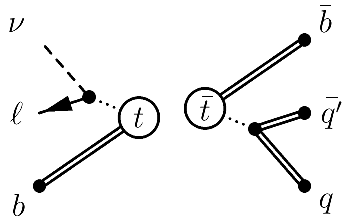

Figure 1.2: Schematic diagram of the observable decay products in a $t\bar{t}$ production event.

lepton interacts with sensors as it travels away from the $W^{\pm}$ decay point, leaving a trail of signals in the detector (Figure 1.3). The neutrino, which has a very small probability of interacting in the detector, is not observed. From the positions of the activated sensors, the lepton's path can be reconstructed. If the top quark traveled away from this interaction point before it decayed, this path will not intersect the collision point. By measuring the distance between the collision point and the lepton's path, we estimate the average top quark flight distance.

1.4 Overview of the thesis

As described above, the measurement technique of this dissertation entails determining the lepton track distance from the interaction point. This distance is tested against various hypotheses: that the lepton was produced from a normal t decay, that it was produced in an anomalous (long-lived) t decay, or that it was produced by an unrelated process. In fact, the comparison is made statistically for the entire sample of top event lepton tracks. The probability of measuring a distance d for a single lepton candidate is

$$Prob(d; c\tau) = (\mathsf{p}_{t\bar{t}}) Prob^{t}(d; c\tau) + (1 - \mathsf{p}_{t\bar{t}}) Prob^{!t}(d) \tag{1.1}$$

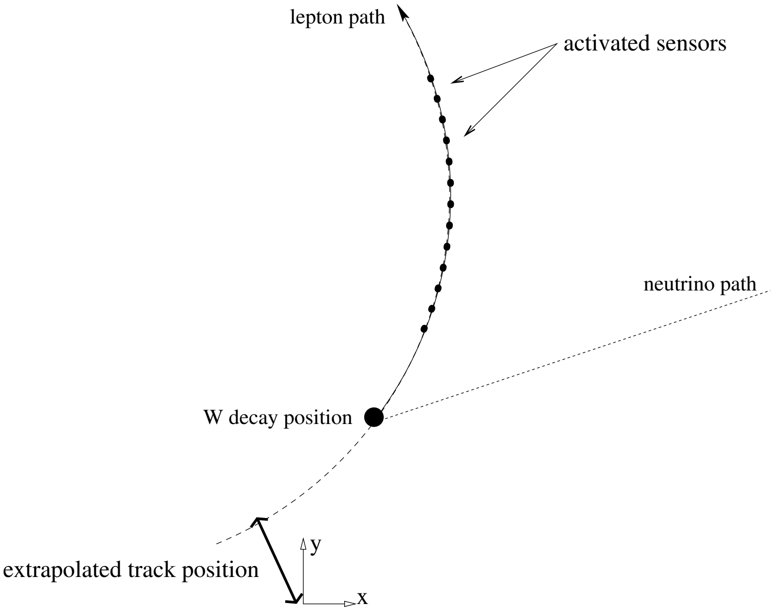

Figure 1.3: Illustration of the $W^{\pm}$ decay products, showing the method for measuring the $W^{\pm}$ decay position.

where $\mathsf{p}_{t\bar{t}}$ is the probability that the lepton came from a $t\bar{t}$ event, $Prob(d;c\tau)$ is the probability of observing a distance d in a $t\bar{t}$ event given the top lifetime $c\tau$, and $Prob^{!t}(d)$ is the probability of observing a distance d in a non-$t\bar{t}$ event from the data sample. Hence we must determine the functions $Prob^{!t}(d)$ and $Prob^{t}(d;c\tau)$, and the probability $\mathsf{p}_{t\bar{t}}$.

For a collection of n similar leptons, the probability of observing the distances $\{d(1), d(2), \ldots d(n)\}$ is $\prod_{i=1}^{n} Prob(d(i);c\tau)$. This total probability is also only a function of the supposed top mean lifetime $c\tau$, and it will be largest at some specific value of $c\tau_t$ which is typically close to the true t lifetime. Collecting the distances $\{d(1), d(2), \ldots d(n)\}$ and determining the unknown components of Equation 1.1 are thus the primary tasks of this lifetime measurement. In determining these components, we are also examining an important collection of top candidate events from a new perspective.

In Chapter 2 we discuss the theoretical context of this measurement. We then describe the experimental apparatus (Chapter 3) and our analysis tools (Chapter 4), and the selection of top candidate events that provide the distances $\{d(1), d(2), \ldots d(n)\}$ (Chapter 5). In Chapter 6, we describe the primary *backgrounds*, or physics processes other than $t\bar{t}$ production that may produce interactions which we erroneously select as top events. This study allows us to calculate $p_{t\bar{t}}$. In Chapter 7 we describe the expected result of the distance measurement for collections of top events and background events, and thus parameterize $Prob^{t}(d; c\tau, \sigma_d)$ and $Prob^{!t}(d; \sigma_d)$. Chapter 8 contains a discussion of the results and the properties of the combined probability function $\prod_{i=1}^{n} Prob(d(i); c\tau)$.

Some appendices are provided. The first describes the characteristics of an important background to $t \to W^{\pm}b$ events with leptonic $W^{\pm}$ decays, and explains a simple method of measuring the number of $t\bar{t}$ events in the data sample when this background event probability is unknown. This method is used in Chapter 6. The second describes another background measurement used in Chapter 6: the number of $t\bar{t}$ candidate events with electrons that were created by photons rather than $W^{\pm}$ bosons. The last appendix describes an experimental control rather than a background calculation. To demonstrate the effectiveness of our methods using a known lifetime signal, we perform the first hadron collider measurement of the tau lepton mean lifetime. This is in many respects similar to the top quark mean lifetime measurement, but measures a non-zero result ($c\tau_{\tau} = 285$ fs) which is consistent with other tau lifetime measurements from more sensitive experiments [5].

Chapter 2

Theoretical Predictions

In this chapter we outline a theoretical model of top quark interactions, and present the indirect evidence that $\tau_t < 10^{-24}$ s. We also briefly describe the strong interactions of a hypothetical long-lived heavy quark. In the concluding section, we describe another theory which could explain an anomalous lepton track d_0 distribution in $t\bar{t}$ candidate events, without modifying the current interpretation of t decay phenomenology.

In the context of this thesis, there are two meanings for the term t quark. The first meaning denotes a quantum state with undetermined mass which is the third-generation up-type quark, expected to decay primarily to b quarks, while the other denotes an empirical object: the particle with a reconstructed mass of around 175 GeV/c^2, pair-produced in $p + \bar{p}$ collisions at the Fermilab Tevatron. Part of the purpose of this thesis is to test whether these two objects are equivalent. In this chapter the notation t or "top" refers to the theoretical object, and "top candidate" to the observed phenomenon.

2.1 Dynamics of the t quark

Our theoretical model for t dynamics is a relativistic spinor field operator with interactions determined by the $SU(3)_{\text{color}} \times SU(2)_{\text{weak}} \times U(1)_{\text{hypercharge}}$ gauge theory known as the Standard Model [6, 7]. We denote this field operator by $\Psi^t(x)$. In the Standard Model, the left-handed helicity projection Ψ^t_L transforms non-trivially under each of the three gauge groups, as shown in Table 2.1. The right-handed counterpart Ψ^t_R is an $SU(2)_{\text{weak}}$ scalar, but otherwise transforms like Ψ^t_L.

Surprisingly, although they are symmetry operations, the $SU(2)_{\text{weak}}$ gauge transformations of the Standard Model mix fields with distinguishable equations of motion (consequences of this symmetry breaking are discussed in Section 2.1.2.). Hence the top weak doublet is usually treated as multiple interacting fields: we will distinguish between the $T_3 = +\frac{1}{2}$ electroweak eigenstate (Ψ^t) and the one with eigenvalue $T_3 = -\frac{1}{2}$ ($\Psi^{b'}$). The gauge index structure of our notation is made explicit in Table 2.1.

Color $SU(3)$	Weak $SU(2)$	Hypercharge $U(1)$
$\begin{pmatrix}\Psi^t_{\mathsf{r}}\\ \Psi^t_{\mathsf{g}}\\ \Psi^t_{\mathsf{b}}\end{pmatrix}_L, \begin{pmatrix}\Psi^t_{\mathsf{r}}\\ \Psi^t_{\mathsf{g}}\\ \Psi^t_{\mathsf{b}}\end{pmatrix}_R$	$\begin{pmatrix}\Psi^t_L\\ \Psi^{b'}_L\end{pmatrix}, \Psi^t_R$	Ψ^t_L, Ψ^t_R

Table 2.1: Transformation properties of the top field under the Standard Model gauge symmetry groups. Lorentz transformations mix the helicity eigenstates Ψ^t_L and Ψ^t_R.

2.1.1 Production

The *chromodynamic* interaction term involving the t quark and the eight $SU(3)_{\text{color}}$ gauge fields (gluons) can be represented by the Feynman diagram in Figure 2.1. There

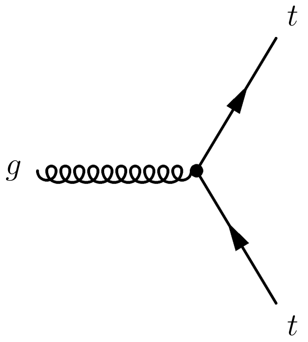

Figure 2.1: Feynman diagram representing the t-gluon interaction term which is responsible for almost all t production at the Tevatron.

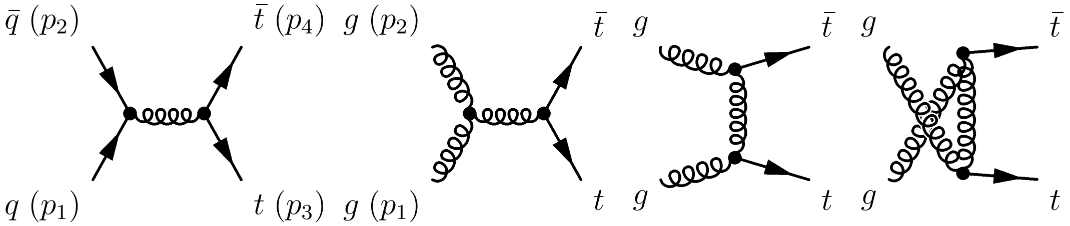

Figure 2.2: Feynman diagrams for leading-order t production processes at the Tevatron.

are five other quarks that transform like t under the $SU(3)_{\text{color}}$ symmetry, so they are all coupled to the gluon fields and a similar diagram exists for each of them. There are also diagrams that only involve gluons. Combining these vertices to represent leading-order transition matrix elements (Figure 2.2), we can describe the production of $t\bar{t}$ at the Tevatron.

Quark-antiquark and gluon-gluon scattering Neglecting all masses except for the top mass (m_t), the differential cross section corresponding to the leftmost diagram can be expressed in terms of $\hat{s} \equiv (p_1 + p_2)^2$, $\hat{t} \equiv (p_1 - p_3)^2$, and $\hat{u} \equiv (p_1 - p_4)^2$ as [8]:

$$\frac{d\sigma^{q\bar{q}\to t\bar{t}}}{d\hat{t}} = \frac{4\pi\alpha_s^2}{9\hat{s}^2}\frac{(\hat{u}-m_t^2)^2 + (\hat{t}-m_t^2)^2 + 2m_t^2 s}{\hat{s}^2}. \tag{2.1}$$

Integrating over the angular phase space, where $(\hat{t} - m_t^2)$ ranges between $\frac{-\hat{s}}{2}(1 + \sqrt{1 - 4m_t^2/\hat{s}})$ and $\frac{-\hat{s}}{2}(1 - \sqrt{1 - 4m_t^2/\hat{s}})$, the total cross section for $q\bar{q} \rightarrow t\bar{t}$ is

$$\sigma_{q\bar{q}\rightarrow t\bar{t}} = \frac{8\pi\alpha_s}{27\hat{s}}\sqrt{1 - \frac{4m_t^2}{\hat{s}}}\left(1 + \frac{2m_t^2}{\hat{s}}\right) \tag{2.2}$$

above the threshold $\sqrt{\hat{s}} = 2m_t$. The cross-section is maximal at $\sqrt{\hat{s}} = 5.8m_t^2$. For the three gluon diagrams, the total cross section is[1] [8]:

$$\sigma_{gg\rightarrow t\bar{t}} = \frac{\pi\alpha_s^2}{3\hat{s}}\left(\left(1 + \frac{4m_t^2}{\hat{s}} + \frac{m_t^2}{8\hat{s}}\right)\ln\frac{1 + \sqrt{1 - \frac{4m_t^2}{\hat{s}}}}{1 - \sqrt{1 - \frac{4m_t^2}{\hat{s}}}} - \left(\frac{7}{4} + \frac{31}{16}\frac{4m_t^2}{\hat{s}}\right)\sqrt{1 - \frac{4m_t^2}{\hat{s}}}\right). \tag{2.3}$$

Hadron-hadron scattering These $q\bar{q}$ and $g\bar{g}$ interaction cross-sections do not predict the size of the top dataset collected at CDF, because the Tevatron beams do not resemble free quark or gluon (generically, *parton*) momentum eigenstates. There is no way to accurately expand the scattering process $p + \bar{p} \rightarrow t\bar{t} + X$ using perturbation theory alone. Instead, the overlap between the incoming bound states and the free parton momentum eigenstates must be determined another way.

Since we know the characteristics of the p and $\bar{p}$ beams at the Tevatron – the center of mass energy $\sqrt{s}$ is 1.96 TeV – we simply need to find the probability that a parton q carrying a fraction x of the hadron's momentum will take part in the collision. The

---

[1] Here we integrated

$$\begin{aligned}
\frac{d\sigma^{gg\rightarrow t\bar{t}}}{d\hat{t}} &= \frac{\pi\alpha_s^2}{8\hat{s}}\left(\frac{6}{\hat{s}^2}(\hat{t} - m_t^2)(\hat{u} - m_t^2) + \frac{4}{3}\frac{(\hat{u} - m_t^2)(\hat{t} - m_t^2) + 2m_t^2(\hat{t} + m_t^2)}{(\hat{t} - m_t^2)^2}\right. \\
&+ 3\frac{(\hat{t} - m_t^2)(\hat{u} - m_t^2) + m_t^2(\hat{u} - \hat{t})}{\hat{s}(\hat{t} - m_t^2)} + \frac{4}{3}\frac{(\hat{u} - m_t^2)(\hat{t} - m_t^2) + 2m_t^2(\hat{u} + m_t^2)}{(\hat{u} - m_t^2)^2} \\
&+ \left. 3\frac{(\hat{t} - m_t^2)(\hat{u} - m_t^2) + m_t^2(\hat{u} - \hat{t})}{\hat{s}(\hat{u} - m_t^2)} - \frac{m_t^2(s - 4m_t^2)}{2(\hat{t} - m_t^2)(\hat{u} - m_t^2)}\right)
\end{aligned}$$

over the same range.

probability naturally depends on the parton species. It also depends slightly on the momentum transfer in of the $t\bar{t}$ production process, because the hadron structure appears increasingly complex to finer probes. The probabilities for every light parton type have been experimentally determined by simultaneously fitting hadronic interaction data from many sources [9]. The parameterizations we use to model the initial state for this measurement have the general form [10]:

$$xf(x,Q^2) = c_1 x^{c_2}(1-x)^{c_3}e^{c_4 x}(1+e^{c_5 x})^{c_6} \tag{2.4}$$

where $Q^2 \simeq \hat{t}$ is the momentum transfer scale. We call $f(x,Q^2)$ the *parton distribution function*, written $f_q(x,\mu^2)$ for a parton of type q. These functions represent an integral over collinear gluon radiation and pair-production processes within the proton, so the scale Q^2 can be understood as the transverse momentum cut-off of this integral. The antiproton parton distribution function is simply related to the proton's: $f_q^{\bar{p}} = f_{\bar{q}}^{p}$.

The cross section for colliding protons and anti-protons at a squared center-of-mass energy s, to produce t quarks is then

$$\begin{aligned}\int dx_{g_1}dx_{g_2}f_g(x_{g_1},Q^2)f_g^{\bar{p}}(x_{g_2},\mu^2)\sigma^{gg\rightarrow t\bar{t}}(x_{g_1}x_{g_2}s)+ \\ \sum_{\{q\}}\int dx_q dx_{\bar{q}} f_q(x_q,Q^2)f_{\bar{q}}^{\bar{p}}(x_{\bar{q}},Q^2)\sigma^{q\bar{q}\rightarrow t\bar{t}}(x_q x_{\bar{q}}s)\end{aligned} \tag{2.5}$$

where $\{q\} \equiv \{u,d,s,c,b\}$. The convolution above has been performed with $\sigma^{q\bar{q}\rightarrow t\bar{t}+X}$ and $\sigma^{gg\rightarrow t\bar{t}+X}$ calculated at next-to-leading order (NLO) with some next-to-next-to-leading order (NNLO) correction terms [11]. Because of the large top mass and the shapes of $f(x,Q^2)$ shown in Figure 2.3, the gluon contribution is much smaller than the quark annihilation contribution at $\sqrt{s}$=1.96 TeV. The value of the total cross section as a function of the top mass is shown in Figure 2.4.

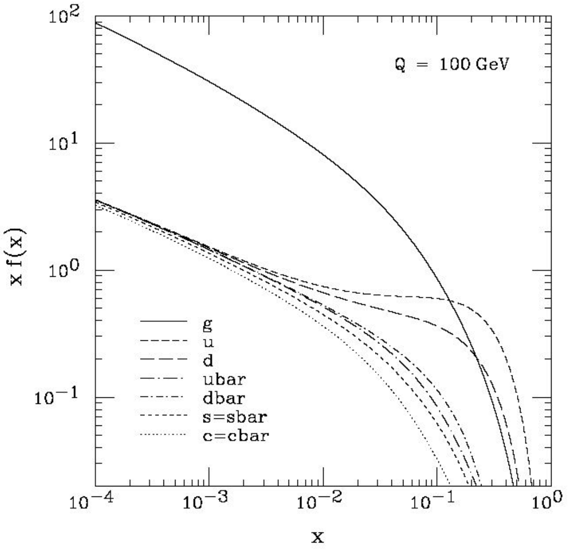

Figure 2.3: Parton distribution functions evaluated at the scale $\mu = 100$ GeV, plotted on a log-log plot [9]. At the threshold for $t\bar{t}$ production at the Tevatron, $f_g(x_g, \mu^2)$ is subordinate to the quark parton distribution functions.

2.1.2 Decay

As noted in the introduction to this section, although $SU(2)_{\text{weak}}$ transformations correspond to a gauged symmetry of the Standard Model, transforming Ψ^t produces a field operator for a quark state with different interactions than t. This symmetry breaking is an artifact that appears in the specific vacuum solutions of the full, symmetric theory [14]: the Standard Model includes one fundamental scalar which is an $SU(2)_{\text{weak}}$ doublet and plays a central role in the organization of matter.

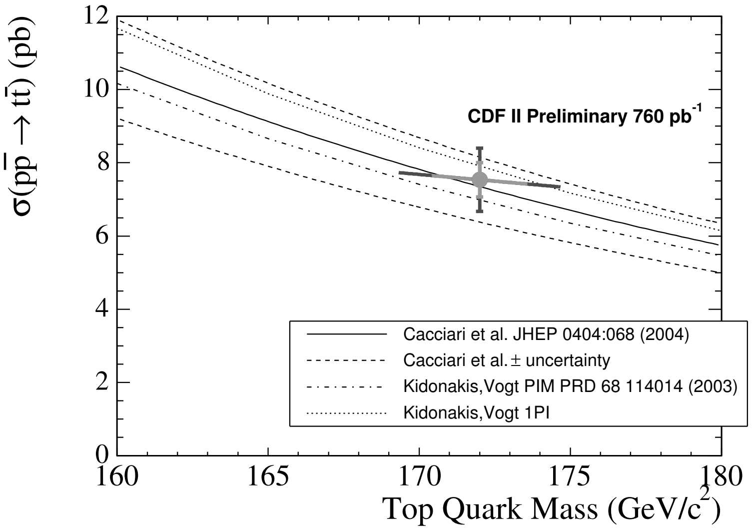

Figure 2.4: Prediction of the total $p + \bar{p} \rightarrow t\bar{t}X$ cross section at $\sqrt{s} = 1.96$ TeV as a function of m_t. The solid line is the calculation at NLO; the dotted and dashed lines are approximate NNLO results using different kinematic approximations [12, 11]. The datapoint represents the best combined CDF measurements [13].

The scalar doublet $\phi(x) \equiv \begin{pmatrix} \phi^+(x) \\ \phi^0(x) \end{pmatrix}$ couples non-universally to the fermions; the quark interaction terms are:

$$\sum_{ij} \left(Y^u_{ij} (\overline{\Psi^{u(i)}_L} \cdot \sigma_2 \phi^\dagger) \Psi^{u(j)}_R + Y^d_{ij} (\overline{\Psi^{d(i)}_L} \cdot \phi) \Psi^{d(j)}_R \right) + \text{h.c.}$$

where the matrices $\mathbf{Y}^u$ and $\mathbf{Y}^d$ are arbitrary. There is also a self-coupling interaction of the form $\mu^2 \phi^\dagger \phi - \frac{\lambda}{2}(\phi^\dagger \phi)^2$, which implies that the lowest energy solutions for the free ϕ field satisfy $\phi^\dagger \phi = \frac{\mu^2}{\lambda} \equiv \frac{v^2}{2}$. Thus ϕ minimizes the potential when it has a non-zero expectation value. If we expand ϕ about this minimumizing v

$$\begin{pmatrix} \phi^+(x) \\ \phi^0(x) \end{pmatrix} \rightarrow \frac{1}{\sqrt{2}} \begin{pmatrix} v^+ \\ v^0 \end{pmatrix} + \begin{pmatrix} H^+(x) \\ H(x) \end{pmatrix}$$

the Lagrangian resembles a theory with a dynamic scalar doublet H, which has "spontaneously generated" mass terms proportional to v from all of the couplings of ϕ to other fields. The mass terms in the effective theory violate electroweak symmetry.

The effects of the symmetry breaking thus include massive gauge bosons as well as quark and lepton mass splittings. Because of these quark mass splittings, a weak isospin rotation of Ψ^t represents the *decay* of a t quark.

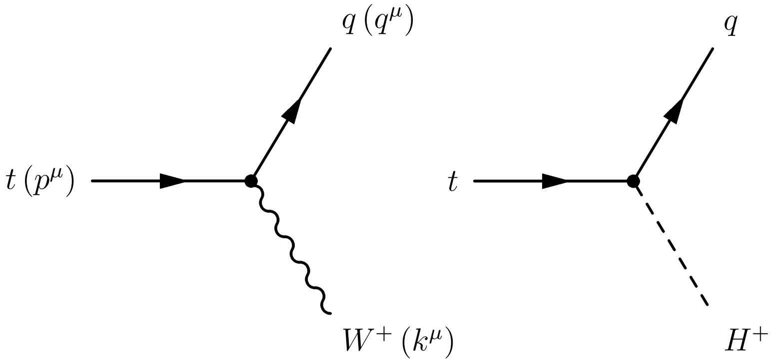

Figure 2.5: Feynman diagrams for t decay at tree level.

The diagrams for t decay are pictured in Figure 2.5. The first diagram corresponds to the matrix element $\mathcal{M}(t \to W\, b) = \frac{ig}{\sqrt{2}}\overline{\Psi^{b'}}\gamma_\mu \epsilon^\mu_W \Psi^t_L$. The second diagram can be ignored in our calculation if we choose a gauge in which $\phi(x)$ everywhere has the form $\begin{pmatrix} 0 \\ v + H(x) \end{pmatrix}$. However, this choice determines the three $W^\pm$ polarization states, which must then satisfy $\sum \epsilon_\mu(k)^* \epsilon_\nu(k) = (g_{\mu\nu} - k_\mu k_\mu / m_W^2)$.

If we assume that t is not in a bound state, no hadronic form factors affect this process (our calculation will validate this assumption, which we return to in Section 2.3.1). Then, with the momentum assignments pictured in the diagram, the squared matrix element for $t \to Wb'$ is

$$\begin{aligned}\sum_{\text{spins}} |\mathcal{M}|^2 &= (p^\mu q^\nu + q^\nu p^\mu - g^{\mu\nu}(p \cdot q))(g_{\mu\nu} - \frac{k_\mu k_\mu}{m_W^2}) \\ &= \frac{g^2}{2}\left((q \cdot p) + \frac{2(k \cdot q)(k \cdot p)}{m_W^2}\right) = \frac{g^2}{4m_W} m_t^4 \left(1 - \frac{m_W^2}{m_t^2}\right)\left(1 + 2\frac{m_W^2}{m_t^2}\right)\end{aligned}$$

where we have used $q \cdot q \simeq 0$. Writing G_F for $\frac{g^2}{8m_W^2}$, the total decay rate is then

$$\Gamma_t \simeq \frac{G_F m_t^3}{8\pi\sqrt{2}}\left(1 - \frac{m_W^2}{m_t^2}\right)^2 \left(1 + 2\frac{m_W^2}{m_t^2}\right) \tag{2.6}$$

If $m_t = 175$ GeV/c^2, $\Gamma_t = 1.56$ GeV and so $\tau_t \equiv \hbar/\Gamma_t \simeq 0.4 \times 10^{-24}$ s. Higher order correction terms give the more precise prediction $\tau_t = 0.47 \times 10^{-24}$ s.

Top decays to lighter quarks

The approximation $q^2 = 0$ affected our numerical calculation of the squared matrix element by less than 0.5%, but it did allow us to sidestep a physical interpretation of the b' state. Since b' is a $T_3 = -\frac{1}{2}$ state, it is natural to identify it with some mixture of the known down-type quarks d, s, and b. Then, insofar as these states are approximately massless, our calculation holds. The distinction between these down-type states is due to the spontaneously generated terms in the Lagrangian density, which take the form $\frac{v}{\sqrt{2}}(\sum_{ij} Y^u_{ij}\Psi^{u(i)}\Psi^{u(j)} + Y^d_{ij}\Psi^{d(i)}\Psi^{d(j)})$. In slightly simpler notation, substituting $\mathbf{M}$ for $\frac{v}{\sqrt{2}}\mathbf{Y}$ and using the vectors $U = \begin{pmatrix} u \\ c \\ t \end{pmatrix}$ and $D = \begin{pmatrix} d \\ s \\ b \end{pmatrix}$,

$$\mathcal{L}_{\text{quark mass}} = \left(\overline{U}_L M^u U_R\right) + \left(\overline{D}_L M^d D_R\right) + \text{h.c.}. \tag{2.7}$$

$\mathbf{M}_d$ is generically a non-diagonal matrix[2]. We can rewrite the isospinor involving t shown in Figure 2.1 in terms of the eigenvectors of $\mathbf{M}_d$, which in the Standard Model

---

[2] The flavor symmetry of the remainder of the Standard Model allows us to rotate U and D together, so we can diagonalize $\mathbf{M}_u$ without loss of generality, but this choice of basis fixes $\mathbf{M}_d$.

are the physical d, s and b quark fields, as

$$\begin{pmatrix} \Psi^t_L \\ V_{tb}\Psi^b_L + V_{ts}\Psi^s_L + V_{td}\Psi^d_L \end{pmatrix}, \tag{2.8}$$

so (neglecting the effects of the light quark masses) the partial widths for $t \to Ws$ and $t \to Wd$ are simply $\Gamma^{t\to Ws} = |V_{ts}|^2\Gamma$ and $\Gamma^{t\to Wd} = |V_{td}|^2\Gamma$.

There are almost no direct experimental constraints on these three coefficients, but powerful indirect limits can be set by assuming that Equation 2.7 is formally correct and that there are no other flavor-mixing terms. In this case, the matrix of all such coefficients,

$$\mathbf{V} \equiv \begin{pmatrix} V_{ud} & V_{us} & V_{ub} & \cdots \\ V_{cd} & V_{cs} & V_{cb} & \cdots \\ V_{td} & V_{ts} & V_{tb} & \cdots \\ \vdots & \vdots & \vdots & \ddots \end{pmatrix} \tag{2.9}$$

satisfies

$$\sum_k V_{ik}V^*_{jk} = \delta_{ij}. \tag{2.10}$$

Thus, direct measurements of V_{ub} and V_{cb} determine V_{tb}. Without limiting the dimension of $\mathbf{V}$ (the number of quark doublets), Equation 2.10 has been shown to imply [15]

$$V_{tb} \geq 0.07. \tag{2.11}$$

If we are certain that there are three quark doublets, all of the coefficients are much more precisely limited [15]:

$$\begin{aligned} V_{td} &\leq 0.011 \pm 0.0009 \\ V_{ts} &\leq 0.044 \pm 0.0010 \\ V_{tb} &\geq 0.9990 \pm 0.0004. \end{aligned}$$

We see that in the Standard Model, almost all t quarks decay as $t \to W^+b$. Tests of this prediction are discussed in Section 2.2.3.

2.2 Indirect evidence for a short-lived t

We calculated the top decay width in Section 2.1.2 with the assumption that $m_t > m_W$, so that the $W^\pm$ is not a virtual particle and the effects of its subsequent decay can be neglected. Otherwise the top decay width would be suppressed. We also assumed that the b' state comprises the three down-type quark mass eigenstates d,s, and b – if there were mixing with another quark more massive than t, some decay channels would be kinematically forbidden and the lower limit on τ_t would be looser (Equation 2.11). The prediction $\tau_t = 0.5 \times 10^{-24}$ s thus rests on the evidence for top's (1) large mass, and (2) exclusive weak coupling to the three lighter down-type quark species. Below, we review this evidence.

2.2.1 Indirect measurements of the t mass

In the Standard Model, both fermions and gauge bosons have mass terms generated by their interactions with the scalar field ϕ described in Section 2.1.2. While the quark mass matrices M^u and M^d are arbitrary, the gauge boson couplings are entirely prescribed by the form of the gauge-covariant derivative. That is to say, since the $W^{\pm}$ and Z^0 bosons simply couple to ϕ as gauge fields, their masses are proportional to weak interaction rates.

The relation between the electroweak couplings and the boson masses can be read[3] from the Higgs kinetic energy term in the Lagrangian of the symmetric theory. When ϕ is replaced by $v + H$, the mass coefficients appear:

$$(D_\mu \phi_0)^\dagger (D_\mu \phi_0) = \frac{v^2}{8} g^2 W^\mu W_\mu + \frac{v^2}{8}(g^2 + g'^2) Z^\mu Z_\mu + (D_\mu H_0)^\dagger (D_\mu H_0) \tag{2.12}$$

The masses thus satisfy

$$m_W^2 = M_Z^2 \frac{g^2}{g^2 + g'^2} = m_Z^2 \cos^2\theta_W. \tag{2.13}$$

However, the observable self-energy of the $W^{\pm}$ is expressed in a perturbative expansion which includes loop corrections like those pictured in Figure 2.6 (left panels). The Z^0 mass is similarly corrected, by the loop diagrams on the right. When the up- and down-type fermions in the loop have different masses, the relative correction to each boson mass is different. For $m_b \simeq 0$, the correction from the four diagrams leads to [17]

$$\delta \frac{m_W^2}{m_Z^2 cos^2\theta_W} \equiv \delta\rho \simeq \frac{3G_F}{8\sqrt{2}\pi^2}\left(\frac{m_t^2}{m_W^2} - \frac{\sin^2\theta_W}{cos^2\theta_W}\ln\left(\frac{m_H^2}{m_W^2} - \frac{5}{6}\right)\right). \tag{2.14}$$

Corrections from the other, light fermions are very small. We can thus determine m_t by comparing the observed mass ratio to the value of θ_W^{eff} directly measured in weak interactions (once radiative corrections to θ_W^{eff} from other diagrams have been

---

[3] It is only this easy to read with a fortuitous choice of basis for the mixed $W^3 - B$ state, which diagonalizes the mass terms – most textbooks begin the derivation from $\frac{v^2}{8}\left[g^2 * (W_1^2 + W_2^2) + (g'B + gW_3)^2\right]$ [16].

constrained). Although the correction depends on the still-unknown mass m_H in Equation 2.14, the logarithm allows us to determine the t mass fairly precisely for an assumed range of values for m_H. The comparison depends on the assumption that no other unknown particles cause radiative corrections to m_W or m_Z.

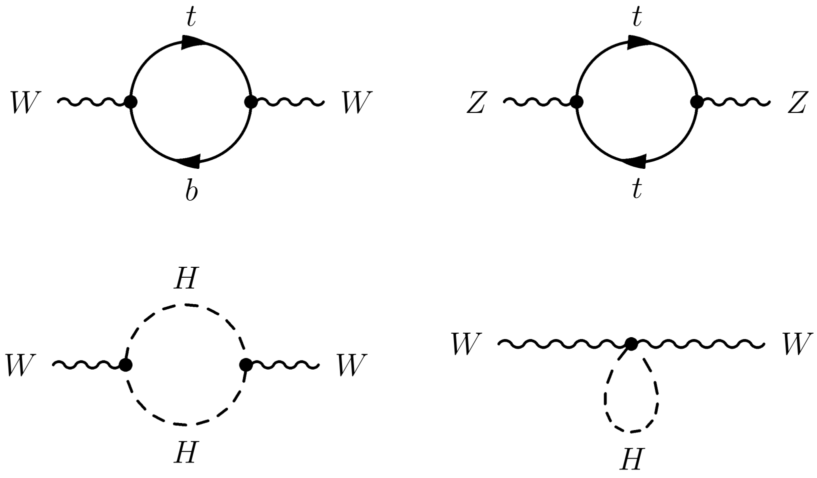

Figure 2.6: Radiative corrections to electroweak boson mass terms.

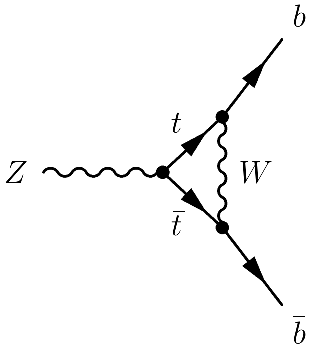

Figure 2.7: Radiative correction to the $Z^0 \to b\bar{b}$ partial decay width.

s shown in Figure 2.7, the Z^0 partial width to $b\bar{b}$ also depends on m_t through radiative corrections, of order $\frac{G_F m_t^2}{2\sqrt{2}\pi^2}$. Several experiments have contributed to the precision measurement of $\sin^2\theta_W^{\mathrm{eff}}$, the $W^\pm$ mass, and other electroweak model parameters sensitive to m_t. Z^0 production and decay were studied by four experiments at the Large Electron-Positron collider (LEP), and by the SLD collaboration at the Staford Linear Collider [17]. $W^\pm$ bosons have been produced and studied at LEPII [18], as well as at the Tevatron [19]. The resulting constraints on m_T as a function of m_H are shown in Figure 2.8. The best limit comes from a global fit to the Standard Model, which determines $m_t = 178.9^{+12}_{-9}$ GeV/c^2 [17].

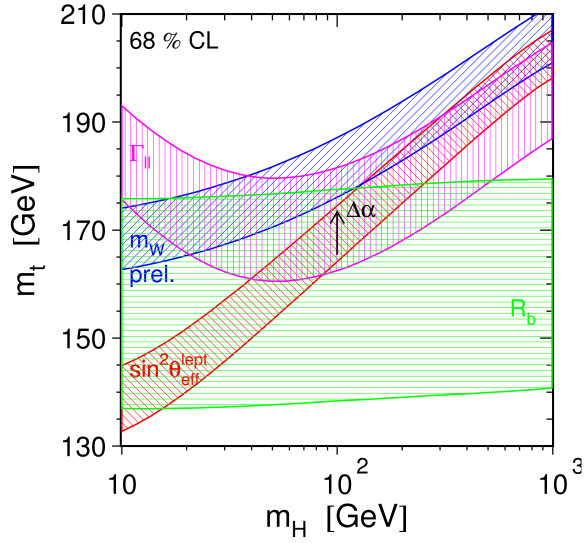

Figure 2.8: Sensitivity of electroweak observables to m_t and m_H. The constraints from measurements of $\sin^2\theta_{lept}^{\mathrm{eff}}$, the Z^0 total leptonic width and hadronic branching fraction to $b\bar{b}$, and the W mass are shown [17].

.

2.2.2 Direct measurements of the t mass

The Tevatron experiments have also measured m_t directly by reconstructing the momenta of the leptons, neutrinos, and jets in $t\bar{t}$ candidate events. One strong indication that these top samples are indeed mostly composed of Standard Model t events is that the experimenters find excellent agreement with the precision electroweak data fit to m_t. The most recent average of CDF and DØ Run II results is

$$m_t = 172.5 \pm 2.3 \mathrm{GeV}/c^2 [20]. \tag{2.15}$$

There is a complementary direct measurement, designed to avoid some of the systematic uncertainty due to the measurement of jet energies[4], which is especially interesting in the context of this dissertation. This method exploits the relatively low velocity of t quarks produced in 1.96 TeV collisions: in this regime, the velocity of the b produced in t decay depends mostly on m_t. The b velocity β_b can be measured without the calorimeter using the average b flight distance in the laboratory frame, which is sensitive to the boost.

The measurement at CDF constructs a projection of the b flight distance, L_{xy}^b, and compares it to templates to find

$$m_t = 185.5^{+15.7}_{-13.9}(\mathrm{stat}) \pm 5.6(\mathrm{syst}) \mathrm{GeV}/c^2 [21]. \tag{2.16}$$

Although the statistical power of this method is still limited, the results are currently in agreement with the result in Equation 2.15 (this measurement is not included in the Tevatron average). Better precision is desirable, because the technique is also

---

[4] See Section 4.1.2 for a discussion.

sensitive to unexpected top quark dynamics. For example, a measurably large t lifetime would bias this determination of m_t toward larger values.

2.2.3 Indirect measurements of the t weak couplings

The Cabbibo-Kobayashi-Maskawa (CKM) matrix [22] has already been introduced: it is $\mathbf{V}$ in Equation 2.9. This matrix describes the strength of the weak interactions between t and other quarks, and precise measurements of its parameters can reveal whether t is coupled to a fourth generation, or if our description of weak flavor mixing is coherent. As Equation 2.10 expresses, $\mathbf{V}$ must be unitary if the Standard Model description of weakly interacting particles is complete. Violation of this condition, which would be an automatic conclusion if t had an observably long lifetime, would imply that $\mathbf{V}$ is not a mixing matrix after all.

The first six CKM matrix elements The *measured* CKM matrix, constructed entirely from directly observed couplings, currently has the form [15]:

$$\begin{pmatrix} 0.9738 \pm 0.0005 & 0.2200 \pm 0.026 & 0.00367 \pm 0.00047 & \\ 0.224 \pm 0.012 & 0.97 \pm 0.09 & 0.0413 \pm 0.0015 & \\ \vdots & \vdots & \vdots & \ddots \end{pmatrix} \tag{2.17}$$

(the relative phases of the matrix elements are not shown). These measurements mostly come from hadronic branching fractions, although V_{cs} is constrained by tagged $W^{\pm}$ decays to charm.

The last(?) row There are some direct measurements (using identified t candidates) involving the elements of the third row of the matrix – both CDF and DØ have measured the ratio of $|V_{tb}|^2$ to $(|V_{tb}|^2+|V_{ts}|^2+|V_{td}|^2)$ using the fraction of $t\bar{t}$ candidate events with zero, one, and two identified b jets in the final state. Both experiments support the same conclusion:

$$\frac{|V_{tb}|^2}{|V_{tb}|^2+|V_{ts}|^2+|V_{td}|^2} > 0.61 \text{ [23]}. \tag{2.18}$$

at 95% C.L.

This limit is the only direct constraint on V_{tb}, but it cannot be included in Equation 2.17 without direct measurements of $|V_{tu}|^2$ and $|V_{ts}|^2$ or other assumptions.

Indirect measurements (assuming no unknown flavor-changing interactions of b) imply $V_{tb} \geq 0$, and the limits above support the Standard Model prediction that V_{tb} is the largest CKM matrix element of the third row. We will often treat V_{tb} as the only non-negligible element of the third row for simplicity.

2.2.4 The top width and electroweak top production

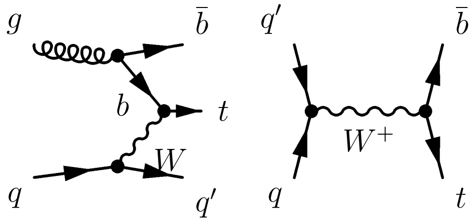

Figure 2.9: Important parton interactions diagrams for "single top" production at the Tevatron. The diagram on the left is termed "t-channel" production, and the one on the right is "s-channel" production, which has a smaller cross section.

The vertex pictured in Figure 2.5 describes t decay but also relates to the electroweak t production mechanisms at the Tevatron that are shown in Figure 2.9. These $t\bar{b}$ production cross sections, like $\Gamma^{t\to Wb}$, are proportional to $|V_{tb}|^2$. Because of the small probability of finding a b in the $p + \bar{p}$ initial state, and the large difference between m_t and m_W, these cross sections are predicted to be fairly small: $\sigma^{\text{t-channel}} \simeq$ 1.98 pb, while $\sigma^{\text{s-channel}} \simeq 0.88$ pb.

Any imaginable suppression of the Standard Model weak couplings of top would decrease its electroweak production rate as well as its decay width: for example, if t were long-lived because it mixed strongly with a heavier fourth generation, the down-type quark in this generation would be too massive to participate much in s- or t-channel single-top production, so $\sigma^{p\bar{p}\to\text{single t}}$ would still be driven by $|V_{tb}|^2$. For this reason, we consider the single-top production cross sections to be inversely proportional to the top mean lifetime in this study.

2.3 Evolution of a long-lived t state

The predictions of the previous sections imply that the Standard Model t quark decays before forming a color-neutral bound state, since QCD becomes confining on longer timescales than τ_t. Hence a long-lived t quark will have different strong interaction phenomenology than the Standard Model t, a difference which could eventually lead to observable effects.

2.3.1 Hadronization and spin correlations

From dimensional analysis, we can argue that the time required to confine a top quark is of order $\frac{1}{\Lambda_{QCD}} \simeq 10^{-23}$ s. Hence intuitively, a top quark with a longer lifetime would hadronize into a bound state before it decayed. We can describe this timescale boundary in another way, without referring to the time-sequence of non-perturbative QCD interactions: only when the self-energy of the t is less uncertain than the splitting of top hadron energy levels does the description as a bound state make sense.

Hadronization of top quarks would be difficult to observe at the Tevatron. A $t\bar{q}$ meson would have very similar kinematics to a free t quark after production because the light degrees of freedom in the hadronized system would hardly affect the t momentum. A $t\bar{t}$ "toponium" resonance would have a more distinguishable signature in its decays to $\gamma\gamma$ or $\ell^+\ell^-$ [24], but such states would be difficult to detect. The production cross section for heavy quarkonium in $p+\bar{p}$ collisions at 2 TeV is less than 2 pb for $m_{Q\bar{Q}} \geq 100$ GeV, and the branching ratio to leptons or photons would be smaller than 10% [24].

Although a T meson would behave on average much like a t quark, its spin state could be greatly affected by soft QCD degrees of freedom. While t quarks should be produced unpolarized in QCD processes at the Tevatron, the t and anti-$\bar{t}$ spins in $t\bar{t}$ production events are correlated. Since the weak decay of t violates parity, this effect is observable in correlated t-anti-t decay distributions [25].

2.3.2 Soft gluon radiation

Naturally, the Standard Model t radiates gluons, but its width acts as an early cutoff of the perturbatively calculable parton shower at a scale $\mathcal{O}(1GeV)$ instead of $\mathcal{O}(\Lambda_{QCD})$. The cutoff can be seen in $\bar{t}tg$ cross-section calculations[5], by the destructive interference of soft gluons radiated from the t and the $\bar{t}$ [26]. As $\Gamma^t \rightarrow \infty$, the cancellation becomes exact, which corresponds to the intuitive statement that a short-lived top has no time to radiate. The width-dependence of the radiation spectrum is most pronounced when there is a large angle between the t and the b direction – in this case, the weak decay has a large effect on the kinematics of the color charge.

Figure 2.10 shows the dependence of the $e^+ + e^- \rightarrow t\bar{t}g$ differential cross section when the b goes backward in the t frame, for a 5 GeV gluon threshold [26]. Any observable top lifetime would correspond to a curve overlying $\Gamma = 0$ in this plot, while the Standard Model prediction should lie near the $\Gamma = 0.7$ result. Because evidently this difference as well as the potential hadronization effects discussed above are all small, we neglect the modified QCD interactions of the long-lived t when we construct a toy model for its production and decay.

2.4 Secondary t quarks

Since this analysis does not distinguish between the t quark production position and the primary $p + \bar{p}$ interaction point, events containing t quarks produced away from this point would resemble long-lived t quark events. While the discussion of

---

[5] This is easiest to analyze in $e^+ + e^- \rightarrow t\bar{t}g$, since initial-final state radiation interference is not present in the case of lepton collisions.

the previous sections points out the difficulty in developing any coherent model that predicts long-lived t quarks, a mechanism to produce *displaced* top quarks has already been explored. Although this measurement is not designed to test such a theory, we describe relevant features of the model below.

Supersymmetry with massive scalars Supersymmetric models extend the Standard Model by postulating that both matter and gauge fields exist in mixed multiplets comprising fermions and bosons. Unbroken supersymmetry predicts the observation of of particles with the same mass and couplings, but different spins. Consequently, realistic supersymmetry models are broken.

Besides all of the extra particles, supersymmetric theories differ from the Standard Model in the behavior of scalar energies: in the Standard Model radiative corrections to the energies imply that they should be consistent with the largest mass scale in the theory, while in supersymmetry the corrections cancel in pairs. Hence some of the strongest motivations for supersymmetry are its potential explanation of the small Higgs mass and the small vacuum energy [27]. To explain the Higgs mass, the supersymmetry breaking scale is often set near 1 TeV in models[6]. However, such a low scale implies that the supersymmetry-breaking interactions should have effects on low energy experiments, and this generally leads to predicted phenomena that have not been observed. Supersymmetry-breaking models at the TeV scale must be carefully constructed to avoid over-predicting the rate of flavor-changing interactions among Standard Model states.

These "flavor problems" can be avoided with very heavy fermion superpartners

---

[6] Such a scale does not naturally explain the small cosmological constant.

[28] and conserved R-parity. When the sfermions are heavy and the gauginos are relatively light, the gluino ($\tilde{g}$) decays are restricted by R-parity and $SU(3)_{\text{color}}$ charge conservation. The gluino can only decay via loops or virtual squarks, as pictured in Figure 2.11, so its mean lifetime is related to the mass of the sfermions.

In useful units, the gluino lifetime can be written

$$c\tau_{\tilde{g}} \simeq 1 \text{ mm} \times \left(\frac{m_s}{10^6 GeV}\right)^4 \left(\frac{1TeV}{m_{\tilde{g}}}\right)^5 [29]. \tag{2.19}$$

Gluinos in this scenario could decay via $q\bar{q}\tilde{\chi}^0$, $g\tilde{\chi}^0$, or $q\bar{q'}\tilde{\chi}^{\pm}$. In many constructions of the model, the branching fraction to $t\bar{t}\tilde{\chi}^0$ would be enhanced because the $\tilde{t}$ tends to be lighter than the other sfermions and makes a larger contribution to the loop diagrams of Figure 2.11. Hence $t\bar{t}X$ events with enhanced missing transverse energy and some evidence of late $t\bar{t}$ production could be a fruitful search channel for some region of "split" supersymmetry parameter space.

The pair-production of a such a gluino by strong interactions in this model is only suppressed by the gluino mass. At the Tevatron, a gluino massive enough to decay to real t pairs would have a production cross section less than 10 fb. The branching fractions depend strongly on the masses in the model: for pair-produced 500 GeV gluinos in a model with $m_s = 10^6$ GeV/c, the final state $q\bar{q}g\chi^0\chi^0$ might be expected in about 25% of $\tilde{g}\tilde{g}$ production events [29, 30]. In such a scenario, $c\tau_g$ would be around 37 μm, and the g velocity would be 0.4 c at the Tevatron on average [31].

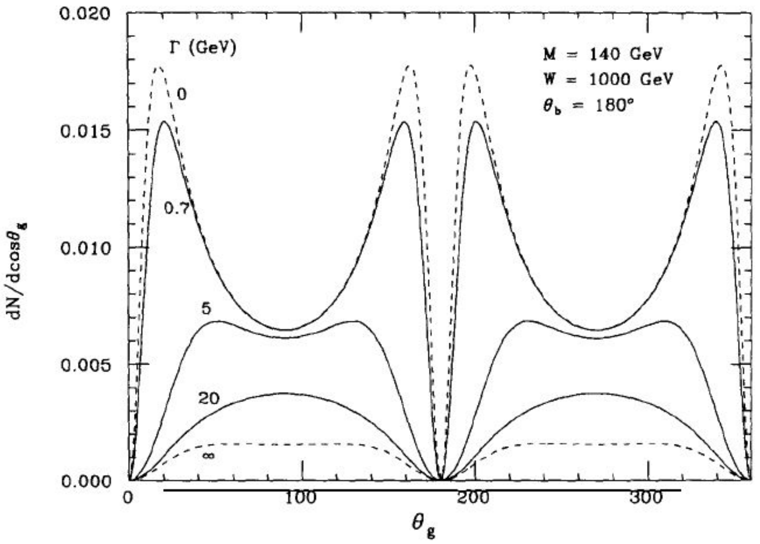

Figure 2.10: Top width dependence of the differential cross section for gluon radiation from $t\bar{t}$ final states in $e^+e^- \to t\bar{t}X$ [26].

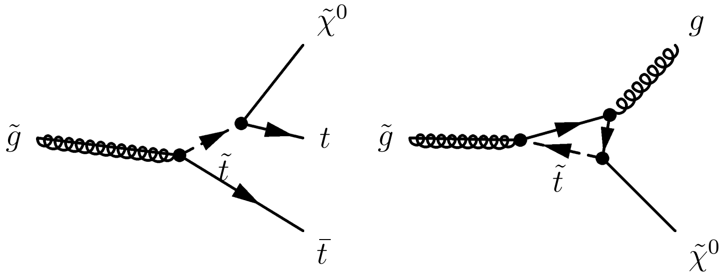

Figure 2.11: Feynman diagrams representing the leading contributions to gluino decay in “split” supersymmetry models.

Chapter 3

Experimental Apparatus

> Protons circulating clockwise in the Tevatron collide with antiprotons that are circulating counterclockwise. They collide at two large experiments that hang like parasites around the Tevatron beam pipe.
>
> **Fermilab Today, November 2004**

This experiment was conducted at the Collider Detector at Fermilab (CDF), a facility designed to study many aspects of proton-antiproton collisions produced by the Fermilab Tevatron accelerator. Both CDF and the Tevatron have been operating since 1989, but the data collected for this experiment was taken during *Run II*, after the accelerator was renovated to produce more intense particle beams at higher energies. CDF was also extensively upgraded during this period. In this chapter, we describe the accelerator and detector apparatus used in the early Run II data collection period from 2001 to 2005.

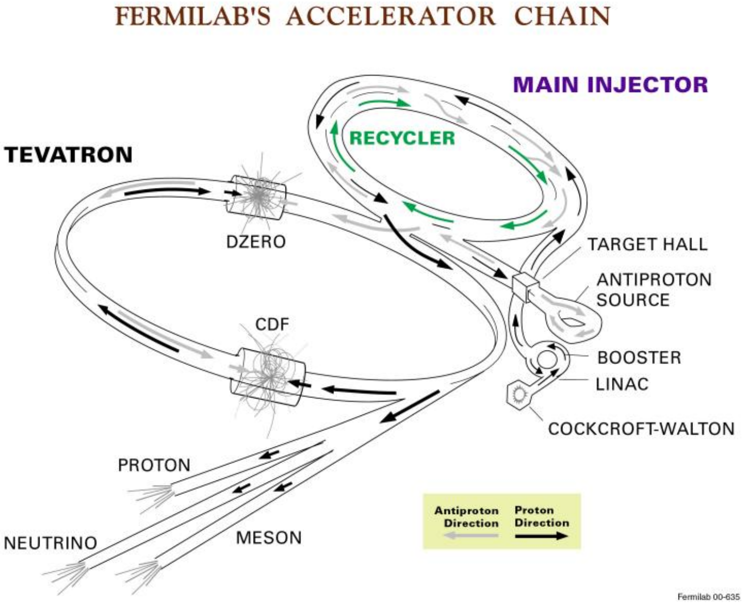

Figure 3.1: The Fermilab accelerator system [32]. The accelerators and detectors are not drawn to scale.

3.1 The Fermilab Tevatron accelerator

The *Tevatron* is a circular synchrotron collider designed to accelerate counter-rotating beams of protons and antiprotons, which are produced by other instruments in the Fermilab accelerator complex. The entire accelerator system is depicted in Figure 3.1, which illustrates the apparatus used to produce a *store* of 980 GeV protons and 980 GeV anti-protons from a bottle of hydrogen gas. These proton and anti-proton beams, each composed of 36 *bunches*, can collide in the Tevatron for several days, with inelastic proton/anti-proton interactions occurring over 6 million times per second. During this time, the density of particles in each beam is gradually diminished until the store is ended or accidentally lost. The data used in this thesis were collected over 523 stores with an average duration of 17.5 hours [33].

3.1.1 Proton beam

Within an enclosure held at a potential of -750 kV by a Cockcroft-Walton voltage multiplier, neutral hydrogen gas is ionized to create H^- ions. These ions drift through 750 kV toward ground, guided by coaxial charged titanium disks. The stream of accelerated ions is subsequently chopped into bunches with 5 ns spacing, to match the RF frequency of the *linac* (linear accelerator). The Fermilab linac is in fact a series of two linear accelerators, one drift-tube (Alvarez) accelerator and one side-coupled cavity accelerator, which ultimately brings the H^- to an energy of 400 MeV. After the linac, the ions pass through a carbon foil which removes the two electrons from each ion. The resulting proton beam is transferred into a synchrotron accelerator, the booster, which bunches the beam and accelerates it to 8 GeV. Groups of bunches are then passed to the Main Injector, and accelerated to 120 GeV. At this stage, the bunches can extracted to the antiproton source described below. In "Tevatron mode," however, the beam is further accelerated to 150 GeVand released into the Tevatron accelerator. This transfer is repeated until there are 36 bunches circulating at 150 GeV in the Tevatron.

3.1.2 Antiproton beam

In antiproton production mode, the Main Injector releases the 120 GeV protons toward a nickel target. Just before reaching the target the proton bunches are focused spatially at the expense of coherence in momentum space. In a small fraction of beam-target collisions, antiprotons are created with a wide spread in momenta. The cone of ejected antiprotons is focused into a beam by a lithium lens, and then separated from other collision products by a magnetic filter, which accepts particles with $E \simeq 8$ GeV and negative charge. Nearly 10^5 protons from the Main Injector collide with the target before one antiproton is accepted. The antiprotons are then stochastically cooled in the *debuncher* before being transfered to the accumulator, in the same tunnel. When sufficient antiprotons are stored in the accumulator they are passed to the Main Injector, accelerated with the protons to 150 GeV and finally injected into the Tevatron.

3.1.3 Collisions

Upon reaching 150 GeV the proton and antiproton beams are coalesced and transferred from the Main Injector to the Tevatron, a 1 km-radius accelerator with superconducting magnets that allows each beam to be accelerated up to 1000 GeV. The proton and antiproton beams, traveling in non-intersecting orbits engineered by electrostatic separators, are then simultaneously accelerated from 150 to 980 GeV. Each beam is formed of 36 bunches with essentially Gaussian density profiles, arranged in three trains: the trains contain twelve bunches separated by 396 ns and each train is separated by 2.6 μs gaps. After the bunches reach 980 GeV the orbits are modified to collide at two points in the Tevatron ring, BØ and DØ.

Since the circumference of the Tevatron is 6.28 km, the 36 relativistic bunches circle the ring in approximately 21 μs, and the average collision frequency is 1.7 MHz. The particles in the beam do not follow exactly circular orbits: a series of focusing and defocussing magnetic "lenses" constrain oscillations of a single particle about the nominal orbit. These oscillations cause the spatial density of the beams to vary in space and time, but because the system of magnets and electric fields is ideally a conservative mechanical system, the phase space density of the beam ensemble for any pair of conjugate coordinates is constant. This density is related to the probability that beam particles interact, and also to the spatial extent of the beams.

If the beam average direction is denoted $\hat{z}$ and x is a transverse (orthogonal to $\hat{z}$) coordinate, the area A of $(x, \frac{dx}{dz})$ phase space that encloses all beam orbits determines the r.m.s. of x in the interaction region. The area is used to define the *emittance*, $\epsilon \equiv A/\pi$. In a real accelerator like the Tevatron, the emittance gradually increases due to beam-gas scattering, beam-beam interactions, and other dissipative effects.

The collision probability is proportional to the spatial density of each beam, so to provide a high interaction rate, quadrupole magnets near CDF focus the beams in position space and create a waist in the beam profile[1]. Thus the nearly Gaussian density of each beam near CDF has a z-dependence: for one bunch the time-dependent density at position z, expressed in terms of the number of particles N and the central axis coordinates $(x_0(z), y_0(z))$, is

$$\rho_p(x,y,z,t) = \frac{N}{(\sqrt{2\pi})^2 \sigma_x(z) \sigma_y(z) \sigma_z} e^{-\frac{1}{2}\left((x-x_0(z))^2/\sigma_x^2 + (y-y_0(z))^2/\sigma_y^2 + (z-ct)^2/\sigma_z^2\right)}. \qquad (3.1)$$

The bunch length ($\sim \sigma_z$) is long with respect to the position resolution of CDF, so the luminous region appears extended. We will use the term *beamline* to refer to $(x_0(z), y_0(z))$, the central axis of this region. The axis generally forms a very small angle –less than 1 mrad for all of the stores used in this measurement– with the geometric central axis of the detector.

---

[1] The minimum width is optimally located at the center of the CDF detector, but in fact the x and y minima are slightly offset from one another and typically fall on opposite sides of the center.

The widths $\sigma_x(z)$ and $\sigma_y(z)$ also vary (by $\simeq 80\%$) in the CDF luminous region, so the distribution of collisions in z is not Gaussian. The beam widths have a quadratic shape with a minimum in each coordinate that depends on the emittance: $(\sigma_{x,y}(z))^2 = \epsilon_{x,y}\beta^* \left(1 + \left(\frac{z - z_{\rm min}}{\beta^*}\right)^2\right)$. CDF has measured $\beta^* \simeq 38$ cm and $\epsilon_x \simeq \epsilon_y \sim 1.2 \times 10^{-7}$ cm. The measured values correspond to a z-averaged beam width of about 26 μm in both transverse directions [34].

During the transfer of proton and antiproton beams into the Tevatron the experimenters begin to activate and test various detector systems of CDF. Preparation for data-taking continues in the BØ control room while the beams are being accelerated and focused. The experiment's high voltage systems and sensitive detectors can be powered after the beams are collimated and the losses are low. At this point the experiment begins to record collision data.

3.2 The Collider Detector at Fermilab

The CDF detector is designed to measure the beam luminosity, the initial positions and momenta of most outgoing charged particles, the energies of electrons, photons, and jets, and to rapidly distinguish electrons, muons, and hadrons. Hence it comprises a high-rate luminosity counter, a magnetic spectrometer, electromagnetic and hadronic calorimeters, and drift chambers behind thick iron absorbers for detecting muons. A cross section of the detector is shown in Figure 3.2. The spectrometer system is discussed in Section 3.2.2, the electromagnetic and hadronic calorimeters in Section 3.2.4, and the muon systems in Section 3.2.5. The data from the primary detector systems are collected and quickly analyzed with dedicated hardware to give

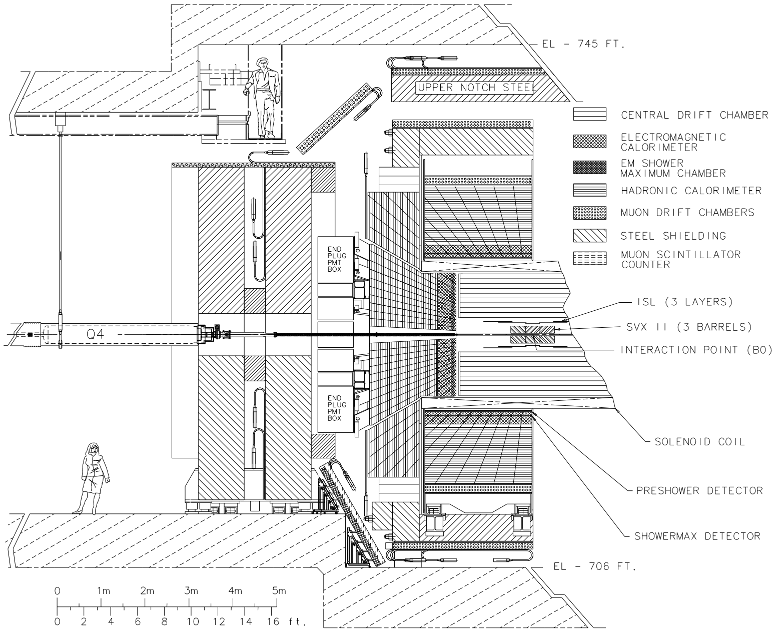

Figure 3.2: The CDF detector. Visitors to the collision hall are usually required to wear safety helmets.

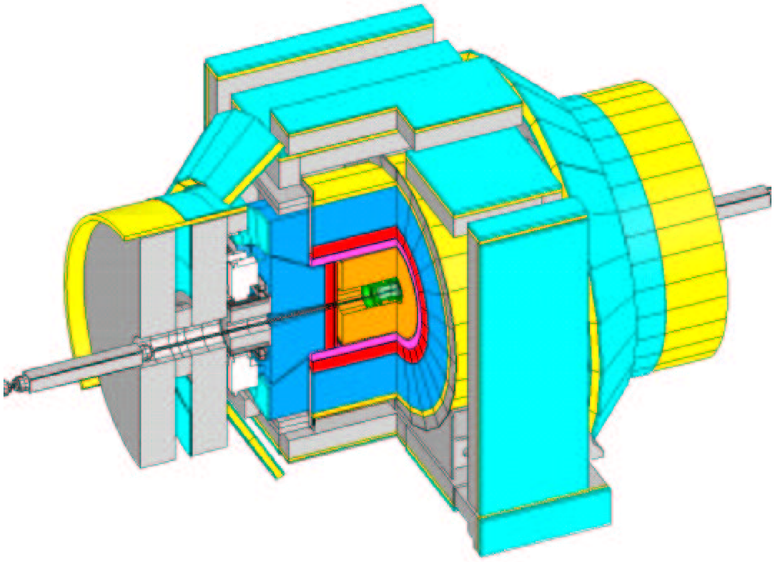

Figure 3.3: An isometric cutaway view of the CDF detector.

a preliminary classification of the collision interaction. Based on this classification, the data is either recorded for further analysis or discarded. This fast filtering system is described in Section 3.2.6. Finally, data passed by this filter is stored and analyzed with custom software modules, to reconstruct as much of the kinematics of the collision as possible. Chapter 4 describes some of the functions of the offline reconstruction software.

3.2.1 Detector geometry

Many detector modules are designated by their geographic location, so both internal Cartesian or polar coordinate systems and external cartographic coordinates (N,S,E,W) are useful. CDF is approximately north of the center of the Tevatron ring, with the beam crossing the detector from east to west. Protons at CDF move eastward. Geometric positions are described in a right-handed coordinate system, with the x axis directed toward the center of the ring, the y axis pointing vertically upward, and the z axis in the proton direction.

The most commonly used coordinates are polar:

$$\begin{aligned} \phi &= \cot^{-1}\left(\frac{y}{x}\right) \\ r &= \sqrt{x^2+y^2} \\ \theta &= \cot^{-1}\left(\frac{z}{r}\right) \qquad (3.2) \end{aligned}$$

with the origin at the nominal center of the detector, within the beampipe enclosure. The convenient variable

$$\eta = -\ln\left(\tan\frac{\theta}{2}\right) \qquad (3.3)$$

is frequently used instead of θ. Many of the fragments of $p+\bar{p}$ collisions do not participate in the hard scattering interaction and escape undetected though the uninstrumented regions near the beam axis, so the observed system of particles does not have zero net p_z. In such systems η is preferred over θ: unlike intervals in θ, differences of the form $\eta_1 - \eta_2$ are invariant under Lorentz boosts in the z direction, when particle masses are neglected. This property has several useful consequences that can be derived by considering the symmetries of a process with $\eta = 0$. For instance, the density distribution of particles in a jet is circular about its central axis in $\eta - \phi$ coordinates, and independent of η. This largely motivates the segmentation of the calorimeters pictured in Figure 3.2.

The region $|\eta| \lesssim 1$ is commonly referred to as "central." The $r - \phi$ plane is referred to as the *transverse* plane, and vectors[2] projected into this plane are usually subscripted with "T." Because the unobserved proton remnants have small momentum projections in this plane, the observed $\sum \vec{p}_T$ vanishes.

3.2.2 Trackers

The spectrometer system, or tracking, measures the trajectory and momentum $\vec{p}$ of charged particles traveling from the collision point outward. It effectively makes one long-exposure snapshot of the charged particles in every collision, recording paths with high accuracy and limited timing information. The tracking system is depicted in Figure 3.4. Positions are measured by the silicon strip detectors and the Central Outer Tracker, a large drift chamber with concentric layers of cells for up to 96

---

[2] The scalar "projection" E_T is very common as well.

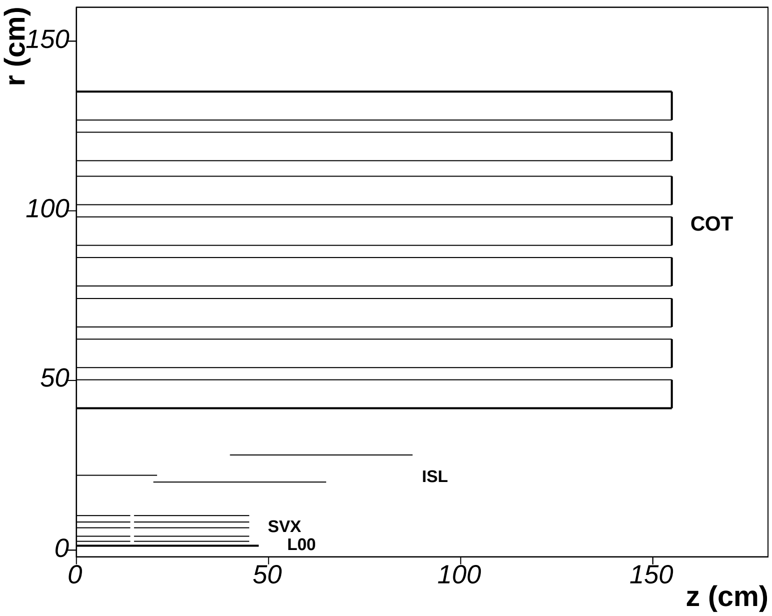

Figure 3.4: One quadrant of the CDF tracking subsystems. Tracks from the nominal origin with $|\eta| \lesssim 1$ will traverse all 8 COT layers.

independent position measurements per track. The superconducting solenoid creates a uniform 1.4 T magnetic field aligned with the z axis. In this field charged particles travel along a helix with radius $R = \frac{|p_T|}{qB}$. Multiple measurements of the (x, y) position along the trajectory of the same charged particle allow a precise measurement of R and hence an accurate transverse momentum determination. These can be combined with measurements of the trajectory's slope, $\cot\theta \equiv \frac{\partial z}{\partial r}$, to calculate p_z and hence the particle's total momentum:

$$\begin{aligned} p_z &= p_T \cot\theta \\ |p| &= p_T \sqrt{1 + \cot^2\theta} \end{aligned} \tag{3.4}$$

This slope is reconstructed mostly from *small-angle stereo* z measurements, which combine the $r - \phi$ measurements of slightly unaligned detectors to triangulate the

z position of a particle. However, a few of the silicon strip arrays are arranged to measure z positions more independently. The angle between a stereo detector's local z axis and the global z direction is its stereo angle (α_s).

A track is an extrapolated path, so we do not know the initial position of the particle along its trajectory[3]. Instead, this initial position is generally taken as the trajectory's closest approach to the collision point. The smallest two-dimensional distance between a trajectory's circular projection onto the $x - y$ plane and the collision point is called the impact parameter, or d_0, and is commonly used to distinguish "primary" tracks from the decay products of long-lived particles.

At least three position measurements are required to reconstruct the trajectory and momentum of a charged particle. The CDF detector can make more than 100 such measurements, to determine track curvature with 0.15% accuracy. The curvature is inversely related to the track radius[4], so this resolution indicates that transverse momentum can be measured with 0.15% accuracy per GeV/c. CDF tracking systems can also measure track initial positions with $\sim 30\mu$m accuracy in the transverse plane. The instruments for making these precise measurements are described in the following sections.

Silicon tracking detectors

The three silicon detectors are each concentric arrays of silicon strip sensors, long electrodes on a thin, reverse-biased $p - n$ junction which detect the charge liberated

---

[3] Some knowledge about a particle's position at the time of the collision can be determined using the temporal information of the drift chamber tracking with specific tracking algorithms such as cosmic ray tracking [35].

[4] The curvature at CDF, $\kappa = \frac{1}{2R_{\mathrm{helix}}}$, is elsewhere referred to as the half-curvature.

when fast charged particles cross the semiconductor crystal. The applied bias voltage removes free charge carriers from the sensitive region until an ionization event takes place, and causes liberated electron-hole pairs to drift toward the sensor strips. Interpolation between the activated electrodes based on the charge that each collects allows a local measurement of the ionization position in the plane of the wafer perpendicular to the strips. The resolution of this measurement is mostly determined by the strip size and separation, and by the diffusive spreading of charge in the crystal as it approaches the readout strips. When the strips run parallel to the z axis, this measurement and the chip location are combined into a ϕ measurement. Double-sided detectors have two sets of strips with different orientations on each side of the silicon, so that ϕ and z can be measured in the same crystal.

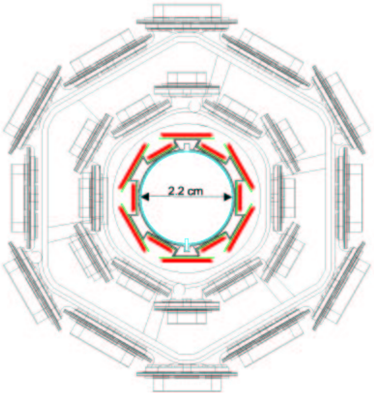

Figure 3.5: Transverse cross-section of the L00 detector, pictured within the inner SVX II layers.

L00 L00 is a single-sided, radiation-tolerant silicon strip detector very near the collision point. Six readout modules made up of twelve overlapping sensors in a cylindrical array are attached by a cooled support structure to the beam pipe, providing complete coverage in ϕ and spanning 95 cm in z. The readout strips are spaced by 50 μm and measure single "hits" or ionization positions with 6 μm precision [36].

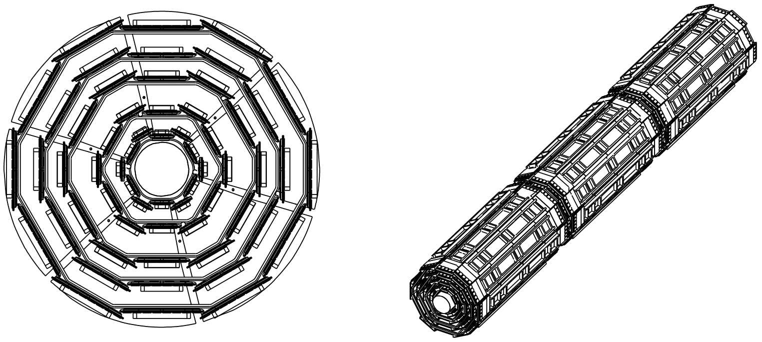

Figure 3.6: A transverse cross section (left) and isometric view (right) of the SVX II detector. The three barrels shown are identical and each carry $12 \times 5 \times 2$ half-ladders.

SVX II SVX II is the primary silicon detector and presents five double sided layers to an outgoing track. There are three mechanical barrels covering the z range -45 cm $< z <$ 45 cm; each barrel is built of 12 identical wedges and supported by beryllium bulkheads at each end. Drawings of this detector are shown in Figure 3.6. Each layer in a wedge makes both a ϕ measurement and a z measurement. Two layers are small-angle stereo (SAS) layers with the strips on the n-side of the junction skewed from parallel to the z direction by $\alpha_s = 1.2°$. The other layers have n-side strips running perpendicular to the z axis ($\alpha_s = 90°$) and make an independent z measurement. The hit resolution of a typical ϕ-side measurement in the innermost SVX layer is about 11 μm for a two-strip cluster [37].

ISL ISL is a double-sided silicon detector between the SVX II and the COT, extending 2 m in length. Its geometry is displayed in Figure 3.7. It provides one additional

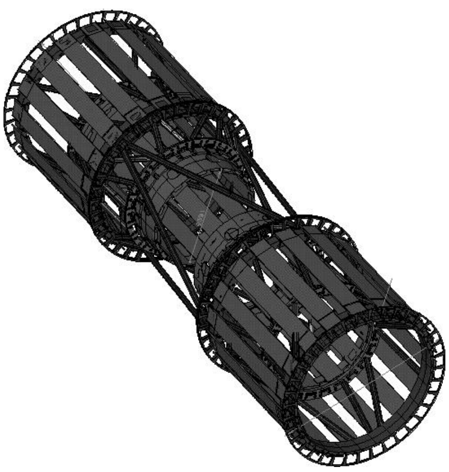

Figure 3.7: The ISL detector.

ϕ measurement at $r = 22$ cm for central tracks and two ϕ measurements, at radii of 20 cm and 28 cm, for tracks at $1.0 < |\eta| < 2.0$ which do not pass through all of the outer tracking detector. Like the SVX II, each ISL ladder has readout strips on both sides; the p-side has axial strips measuring azimuthal angle, and the n-side has $\alpha_s = 1.2^\circ$ SAS strips for determining z. The strip pitch is 112 μm on each side. The average number of strips in a cluster is 1.7 and the average position resolution was measured to be approximately 25 μm in the absence of magnetic field.

Central Outer Tracker

The central outer tracker (COT) [38] is a cylindrical open-cell drift chamber encircling the beam and silicon detectors. An aluminum cylinder enclosing the volume from $r = 40$ to 140 cm and $z = -155$ to 155 cm is filled with an argon-ethane-isopropyl gas mixture at atmospheric pressure. Charged particles create signals by ionizing the gas: for example, a 5 GeV/c pion traversing this volume will create about

100 ionization clusters[5] per cm.

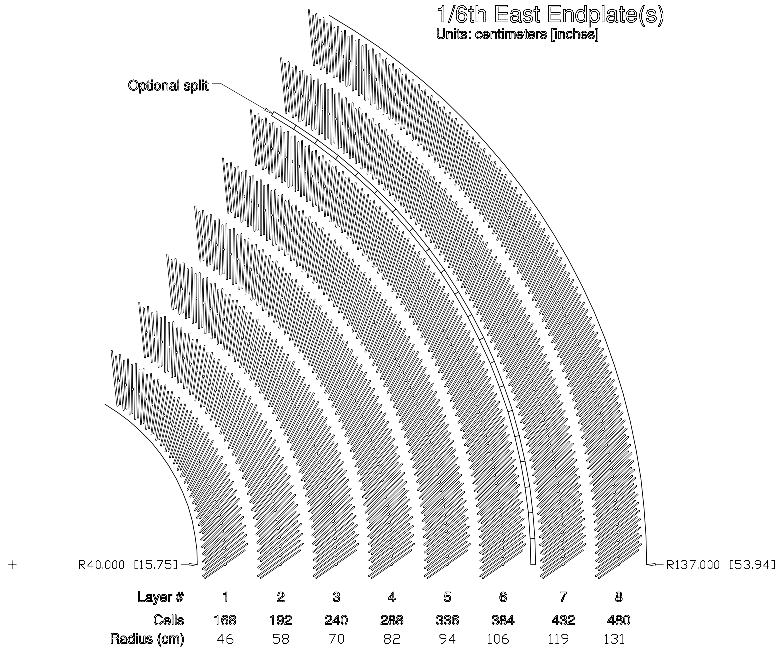

Figure 3.8: One octant of the COT endplate, showing the arrangement of cells in each superlayer.

To detect this liberated charge, the COT volume is crossed by of gold-plated tungsten filaments with a thickness of 40 μm, running along the z axis. The wires are strung through the cylinder in a concentric pattern of 25-wire linear arrays with a pitch of 0.3556 cm. These *wire planes* each have 12 *sense* wires at ~ 3 kV attached to charge readout electronics, and 13 *potential* wires at ~ 2 kV that help maintain a uniform electric field. The wire planes alternate with grounded gold-plated mylar foils –the *field sheets*. The combination of two field sheets and the intermediate wire plane form a *drift cell*, shown in the diagram in Figure 3.9. Cells are arranged in eight concentric radial layers called *superlayers*, which are illustrated in Figure 3.8.

---

[5] Often, the electron liberated by the incident particle will itself ionize a gas molecule, leading to a collection of nearby freed charges called a *cluster*.

Because the COT is immersed in a magnetic field, moving electrons in the cell drift at an angle $\theta_L \simeq 35^\circ$ from the electric field direction. The spread of electron arrival times at a wire from a track is minimal when the track is perpendicular to the drift direction. For this reason, the cells were constructed with a 35° tilt, yielding an approximately azimuthal drift direction and optimal position resolution for high-momentum tracks. At a few wire diameters from the wire surface the field gradient is large, and the accelerated electrons ionize the gas exponentially in an electron avalanche. The COT gas and wire potentials were chosen to attain a *gas gain* of 2×10^4 avalanche electrons per primary ionization electron.

The moving charge of the avalanche electrons and ions induces a pulse on the sense wire which is filtered by a discriminator and charge integrating circuit, so that the signal's size and arrival time can both be recorded for later track reconstruction. Unlike the movement of charge in silicon, drift in a gas chamber is slow, and the signal on the sense wire might follow the initial ionization by as much as 160 ns. A precise position measurement can be determined from the time the electron pulse arrives on a wire, with $\sim 140\ \mu$m precision for a single wire. Each cell records up to twelve signals, and the different drift times are combined to calculate a track segment, as explained in Section 4.1.1. Alternating layers of the COT have a stereo angle offset, allowing pattern recognition algorithms to transform the track segments into three-dimensional helical trajectories. To ensure precise three-dimensional reconstruction, the lepton tracks studied in this analysis must have at least five sense wire hits in three axial layers and two stereo layers.

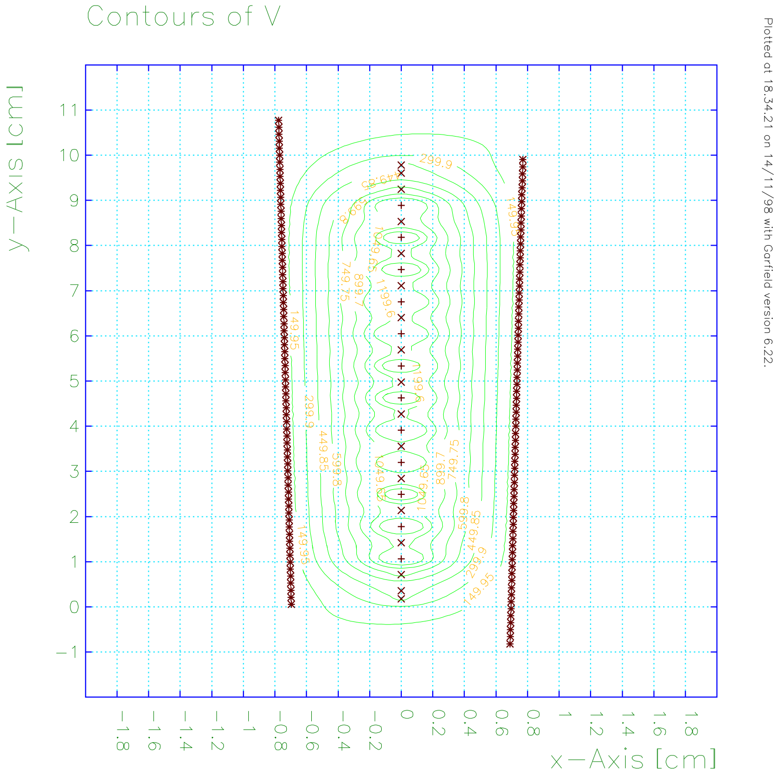

Figure 3.9: Geometry of a COT drift cell in superlayer 4. Note the different axis scales, chosen to better display variations in the equipotential lines.

3.2.3 Time-of-Flight

The time-of-flight (TOF) detector [39] is a barrel of scintillating bars at the outer radius of the COT, before the solenoid. The length of each bar is 279.4 cm, and each has a 40 × 40 mm cross section. The bars are read out on each end by a photomultiplier tube. The time of PMT signals from charged tracks crossing the TOF is recorded, to detect cosmic ray muons and to identify particles by comparing the deduced velocity to the momentum.

The narrow bars have $\sim$ 100 ps timing resolution and an approximately 35% occupancy in CDF events. If a TOF bar is hit by two nearby tracks in the same event, it will naturally record the flight time of the higher-velocity track.

3.2.4 Calorimetry

The energy of charged and neutral particles exiting the tracking detectors is measured by a system of sampling scintillator calorimeters, which are alternating layers of scintillator and dense lead or iron absorbers. The scintillator light from the shower of particles created in the dense layers is guided to photomultiplier tubes connected to analog-to-digital converters (ADCs), so the recorded signal is proportional to the number of particles liberated in the shower.

The geometry of the CDF calorimetry is dictated by the goals of separating electromagnetically interacting particles from hadrons, and uniformly detecting and measuring the energy of photons, electrons, and jets produced over a wide range of η. *Projective towers* of detectors in independent readout channels point toward the collision region, mostly aligned with the particles produced there. The towers are segmented uniformly in ϕ and in η. The electromagnetic calorimeter, composed of lead and polystyrene scintillator, essentially absorbs electrons and photons, but presents a low probability of interaction to hadronic particles. Hence the EM section in each tower is followed by a hadronic section, which is made of many layers of steel and scintillator and is mostly opaque to hadrons.

The apparent density of a material to electromagnetic interactions (pair-production and *bremsstrahlung*) is quantified by the radiation length X_0. The electromagnetic shower size, and the total energy deposited by an electron or photon, scales with X_0. Hadrons in material can create π^0s which lead to electromagnetic showers, but tend to lose most of their energy in hadron showers. The scale of hadronic showering is set by the mean "free[6]" path, or interaction length λ_{int}, of the material.

CEM

The Central Electromagnetic (CEM) calorimeter [40] is a system of three subdetectors measuring electromagnetic particles' energy, position, and shower profile that typically absorbs all but a tiny fraction (e^{-19}) of an incident electron's energy.

CEM modules are wedges 230 cm long, each spanning 15° in ϕ. Each is segmented into 10 η towers. The layout of a single module is shown in Figure 3.10. Two modules cover the region $-1.1 < |\eta| < 1.1$, with a small gap between them in the center. The entire detector comprises 4 arches of 12 modules. These are designated by their geographical coordinates as the NW, SW, NE, and SE arches.

The primary CEM volume is a stack of thirty-one 5 mm sheets of polished polystyrene scintillator, alternating with thirty layers of 0.125 in lead sheets clad

---

[6] Elastic and nearly elastic scattering is ignored in this definition of the free path.

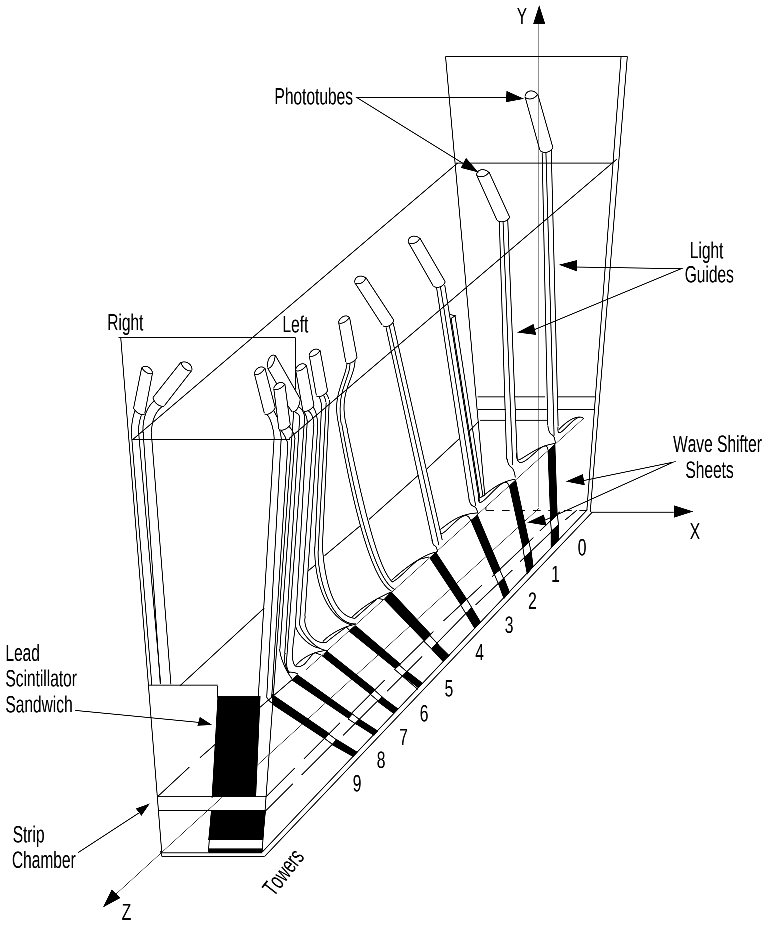

Figure 3.10: Diagram of a 15° CEM module.

in 0.015 in aluminum. There is a gap after the 8th layer of lead for the CES described below. Light in the CEM is collected by doped acrylic *waveshifters*, fitted into 0.25 in gaps on each side of the stacks. These waveshifters, which convert the blue scintillator light to green, are mated to bent acrylic rod light guides. The light guides carry signals between the hadron calorimeters into two photomultiplier tubes per CEM tower. Less than 5% of the azimuthal coverage of the CEM is sacrificed for the gaps for the waveshifters. In the CEM, the energy resolution scales as $\sigma_E/E = 13.5\%/\sqrt{E_T}$. A linear term in the resolution, $1\%E$, comes from measured variations in the response of different modules.

The CEM is augmented by two wire chambers, one just before its inner radius and another embedded within it. These chambers, described below, improve the spatial resolution for electrons and the ability to distinguish π^0 decays from other showers.

CPR The Central Pre-radiator (CPR), positioned between the solenoid and the electromagnetic calorimeter, is a system of proportional chambers with long sense wires running parallel to the beam axis, primarily intended to distinguish minimum-ionizing particles from electrons and neutral meson decays to photon pairs from single photons. The chambers follow the gross segmentation of the central calorimeter wedges: they are each 15° sections about 230 cm in length. Most of the photons escaping the COT will convert to e^+e^- pairs in the solenoid coil, and the resulting early showers will be detected with ~ 1 cm resolution in the CPR. Particle identification is accomplished by comparing the CPR signal size to a reference [41].

CES Beyond eight layers of passive material, amounting to six radiation lengths, the Central Electromagnetic Shower Maximum (CES) wire chamber is embedded in each wedge of the electromagnetic calorimeter. Electromagnetic showers are mostly composed of electrons, positrons, and photons, which create more charged particles in highly inelastic collisions. After approximately six radiation lengths, the average energy of a particle in the shower is too small to create more particles, and the shower reaches its maximum particle multiplicity. This depth is only logarithmically dependent on incident energy. The CES is an array of sense wires spaced by 1.45 cm and extending 230 cm, the length of each wedge. Perpendicular to the wires, cathode strips spaced by 1.67-2.01 cm allow showers to be located in two dimensions. This geometry measures electromagnetic shower centroids with $\sim$ 2cm resolution, far more accurately than the tower segmentation allows. The two-dimensional shower profile shape also allows some differentiation between π^0 and single electron showers [42].

PEM

The Plug Electromagnetic (PEM) calorimeter extends the calorimetry down to $|\eta| < 3.6$, which is 3° from the beam axis. Like the CEM it is a lead/scintillator sampling calorimeter, with a total depth of 21 radiation lengths and embedded with a shower maximum detector at $\sim 6X_0$. In the plug, the shower maximum detector is an array of scintillating strips. An initial layer of scintillator serves as a preshower detector [43]. Electrons reconstructed in the plug are not used in this analysis.

Hadronic calorimeters

CHA and WHA Within each central calorimeter wedge at a higher radius than the CEM, the Central Hadronic (CHA) calorimeter modules are constructed of 32 layers of steel and acrylic scintillator. Each scintillator layer is 1 cm thick and the steel layers are 2.5 cm thick. As in the CEM, the light produced in the scintillator by the shower particles produced within the steel absorber layers is transmitted to wavelength shifters at the sides of each module. These are mated to lightguides which carry the signals to photomultiplier tubes. The 32 layers of material are $4.7\lambda_{\text{int}}$ thick for hadrons at normal incidence. The sampling contribution to the CHA energy resolution is $50\%/\sqrt{E}$, with a constant term of 3%.

Because the calorimeter is barrel shaped, some of the 10 η towers of each module are cut off in the CHA. Only five towers on each side contain the full 32 layers of detector. To better contain hadronic showers at intermediate η, the Wall Hadronic (WHA) calorimeter is positioned between the barrel and the endplug.

PHA The hadronic plug calorimeter sits beyond the $\simeq 1\lambda_{\text{int}}$ depth of the electromagnetic section, and adds nearly $7\lambda_{\text{int}}$ more. It is constructed of 23 layers of steel and scintillator. As in the PEM, light is carried from the scintillator by an wavelength-shifting fiber rather than waveguides on the sides. The resolution of the hadronic energy measurement is $80\%/\sqrt{E} \oplus 5\%$ [44].

3.2.5 Muon detectors

Just beyond the hadronic calorimeters is another series of argon-ethane drift chambers, which are muon detectors by virtue of the fact that muons have a low interaction probability with the steel and lead absorbers of the calorimetry, and pass through without losing much momentum. Each detector is an array of rectangular single wire drift tubes arranged in layers. Hits from different detector layers are used to reconstruct short track segments, or *stubs*, which project back to the muon's position in the COT.

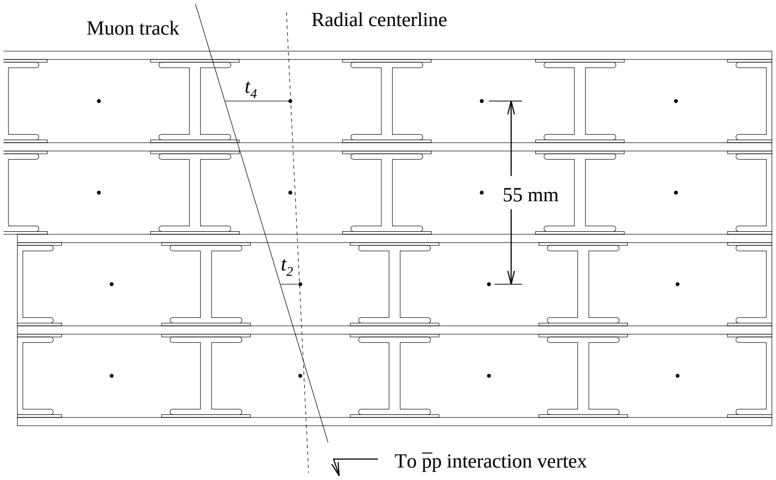

Figure 3.11: Cross section of drift tubes of the muon detector system, shown in the CMU configuration.

All of the muon chambers have similar drift tube properties: the drift field within each cell is mostly uniform in the ϕ direction, becoming radial near the wire. The entire CDF muon system is composed of many subsystems and its geometry is complex due to its installation history and to mechanical constraints in the collision hall. A map of the muon detector coverage in $\eta - \phi$ coordinates is provided in Figure 3.12.

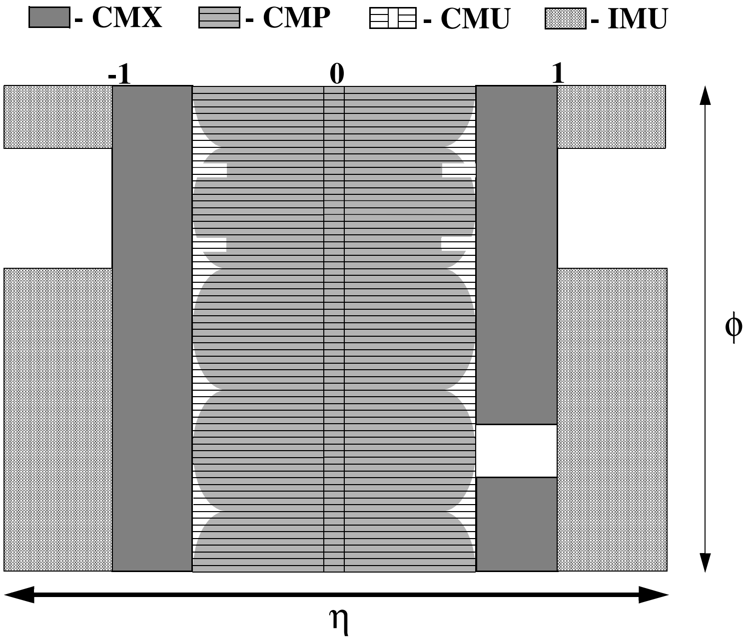

Figure 3.12: The area instrumented with muon detectors, with respect to the nominal origin of CDF. Only CMX and CMU/P detectors were used for the primary (trigger) muons in this analysis.

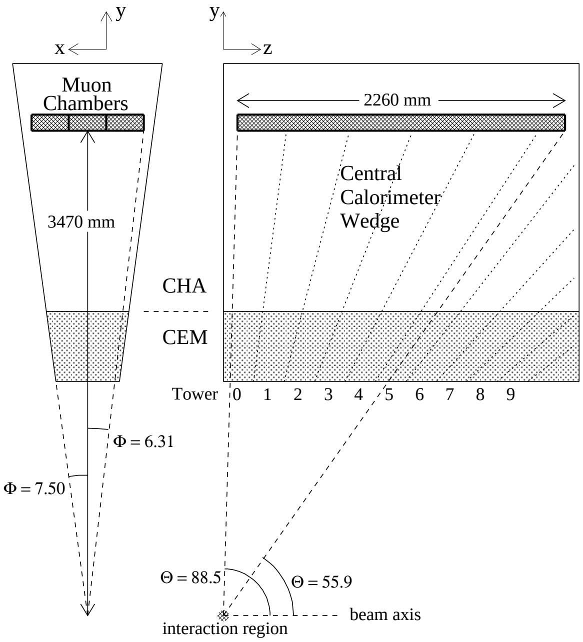

Figure 3.13: One wedge of the central muon detector, which is embedded in the central calorimeter module.

CMU

The CMU is an approximately ϕ-symmetric array of 24 modules 226.2 cm in length at a radius of 347 cm from the beam axis. These are arranged parallel to the beam at the outer radius of every central calorimeter wedge as shown in Figure 3.13. In each wedge are three 4×4 arrays of single-wire drift tubes which each record one three-dimensional track position. The resistive steel wires are connected for adjacent pairs of tubes on one end of the chamber, and the difference between the charges read out from each side of one wire is used to determine the chamber that was hit, and to find the hit z coordinate to within a few centimeters. The modules are only 76.3 cm wide spanning 12.6° in ϕ, so there is a 2.4° gap between each module and an 18 cm gap at $\eta = 0$ between the east and west detectors [45].

CMP and CSP

The CMP is a rectangular array of modules with the same $\eta - \phi$ coverage as the CMU. One module is 640 cm long, the length of the entire central region at that radius, Another 60 cm of steel separates the CMU from the CMP, providing further discrimination against penetrating hadronic particles. The $3\lambda_{\text{int}}$ depth of the CMP steel reduces hadronic backgrounds by an additional factor of 10-20, so the CMP is often used to confirm that a CMU stub is indeed a muon track. In this analysis, muons with trajectories intersecting both detectors are required to have hits in each of them.

The maximum drift time in a CMP chamber is about 1.5 μs, longer than the beam crossing period. To enable muon triggers and remove ambiguity in matching muons to collisions, 2.5 cm thick scintillating tiles are layered atop the CMP drift chambers. One CSP module is half of the CMP chamber length, so two are associated with each CMP chamber.

CMX and CSX

The Central Muon Extension (CMX) completes the η range of muon coverage to $|\eta| < 1.0$ for most values of ϕ. The original detector used in Run I consisted of two "arches" which together spanned 240° in ϕ. Three of the four gaps in ϕ were filled in Run II by the *miniskirt* and *keystone* modules – the west keystone region is uninstrumented because of solenoid cooling systems. The 15° wedges in the "arches" are arranged on a conic section with an opening angle of 41.4°, so that ϕ position measurements are not correlated with θ. The miniskirt modules lie in a plane. Like the CMP, the CMX modules are built of staggered layers of noncontiguous drift tubes, although because of the conical geometry, the gaps between chambers are larger at small η and eight layers are needed to ensure at least four potential hits on every stub.

The Central Scintillator Extension (CSX) scintillating counters cover both sides of the CMX detectors and provide better timing resolution for muons in the CMX. They are used in the trigger. On the miniskirt, only the side closer to the interaction point is covered by scintillator.

IMU

In this thesis, muons identified by the Intermediate Muon (IMU) system were not used in identifying t decays. The IMU consists of the Barrel Muon drift chambers (BMU) and nearby scintillating tiles (BSU and TSU). The BMU detects muons with $p \geq 3$ GeV/c and $1 \leq |\eta| \leq 1.5$, but only covers the range $235^\circ < \phi$ and $315^\circ > \phi$. It is constructed of drift tubes in a four-layer cell structure similar to that of the CMP. The scintillator systems BSU and TSU together cover the range $1 \leq \eta \leq 1.5$ for any value of ϕ.

3.2.6 Trigger

Each detector subsystem system has its own data acquisition (DAQ) modules: the calorimeter PMTs are read out by ADCs with integrated memory, and the signals from the muon drift chambers and the COT are digitized by electronics on the chamber and then processed by time to digital converters (TDCs). The raw digital data from a single event exceeds 0.2 MB and the readout system can log about 20 MB/s, so it is infeasible to store the data from every collision.

The decision to continue processing event data is called the *trigger*, and is made in three stages at CDF, called Level 1, Level 2, and Level 3. The data available to the first two trigger stages is schematically depicted in Figure 3.14.

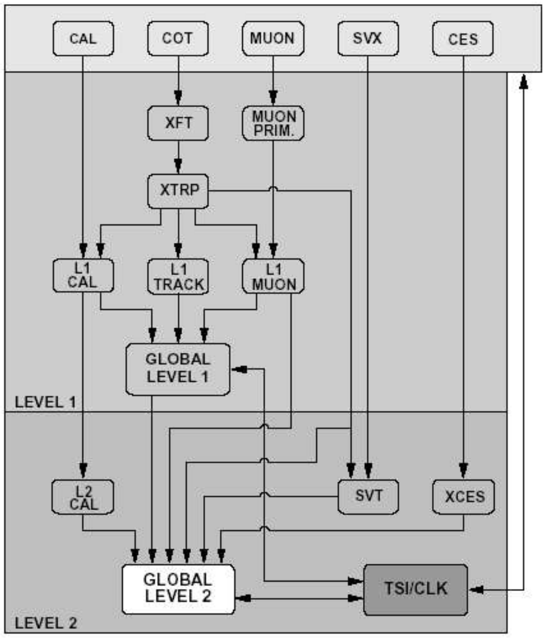

Figure 3.14: The Level 1 and Level 2 triggers at CDF. Level 3 receives the entire event record from all detector systems; this architecture is not shown.

Level 1

Beam crossings occur in bursts at a rate of 2.5 MHz. The first trigger decision is allowed 16 μs, or 42 crossings, to pass or reject an event: every detector's DAQ includes a buffer for storing 42 consecutive events. While events are queued in this L1 pipeline, the Level 1 trigger considers a subset of the event data: tower energies from the calorimeter (L1CAL), quickly reconstructed tracks from the COT (XFT/XTRP), and correlated hits from the muon detectors (L1MUON). The Level 1 trigger decision is based on the event satisfying one of 64 preselected binary combinations of the processors' output.

Level 2

If an event passes Level 1 its data is transmitted from the pipeline to a second memory buffer, the Level 2 buffer, and processed by the asynchronous Level 2 trigger. This trigger is programmable, so its configuration has evolved during Run II. It adds detail and new detector information to the Level 1 objects: adjacent calorimeter towers can be grouped into jets, electrons and photons can be identified from the CES detector data, and the Level 1 tracks can be matched to track stubs in the silicon detector, muons, or electron clusters. At each detector's DAQ controller, four buffers are present to store data passed by the first trigger. A specific subset of this data is passed to the Level 2 processors. Each buffer remains full until a Level 2 decision for that event is reached by the trigger: if all four buffers are full, events from Level 1 must be rejected.

Level 3

After a Level 2 decision to accept, each DAQ is polled for its event data, which is sent to the *event builder*. There, data from the same beam crossing is formatted into banks and sent to the Level 3 farm [46], an array of over 250 dual-processor Linux CPUs that uses all of the event data to ultimately decide whether or not the event merits permanent storage. The Level 3 farm has access to recent detector calibrations, which are compressed along with the current reconstruction executable file and uploaded to each of the processor nodes at the beginning of data-taking. Events are distributed among the nodes, which create a reasonably sophisticated interpretation of the raw detector data, including identified “physics objects” such as electrons, muons, photons, jets, hadronically decaying taus, and missing energy. The algorithms used to reconstruct these objects from the raw data are similar to the offline software algorithms, described in Chapter 4. Events passing Level 3 are sorted into files based the triggers that they passed, and written to tape.

Each event is uniquely denoted by its L1 trigger sequence number, which begins from zero every time data collection commences, and by its *run* number. Physics runs are continuous periods of data-taking with no predetermined length: they are usually ended by the termination of a store, hardware errors, or problems with the DAQ. Runs thus define a span of reasonably constant detector and accelerator status, which is useful for data quality monitoring and for realistic simulations.

Each trigger considers the trigger criteria that the event passed at a previous stage in its decision: in most cases, Level 3 will not pass an event based on objects that were not evident at Level 1 and Level 2. A physicist must choose or construct a chain of trigger requirements, called a *path*, with a large acceptance for the events she wishes to study. In this thesis, $t\bar{t}$ events with one hadronically decaying $W^\pm$ and one leptonically decaying $W^\pm$ were drawn from the trigger paths in Table 3.1. These triggers require an electron or muon with high transverse momentum, characteristic of a $W^\pm$ or Z^0 decay. The electron path results in the `ELECTRON_CENTRAL_18` dataset. The two muon paths were combined to form the `CEM/CMX_18` dataset.

Level	Trigger Name	Description
1	`L1_CEM_8_PT8`	Electromagnetic calorimeter tower with energy $\geq$ 8 GeV (the CHA energy must be less than $\frac{1}{8}$ of the CEM energy in the tower if $E_{\text{tower}} > 14$ GeV) && XFT track in the same wedge with $p_T \geq 10$ GeV/c
2	`L2_CEM_16_PT8`	and: a cluster of towers with $E \geq 16$ GeV and hadronic to electromagnetic energy ratio less than $\frac{1}{8}$, matched to an 8 GeV track 8 GeV
3	`ELECTRON_CENTRAL_18`	and: a fully reconstructed 18 GeV electron with track $p_T > 9$ GeV/c and hadronic to electromagnetic energy ratio less than $\frac{1}{8}$.
1	`L1_CMUP6_PT4`	Matched hits in the CMU and projective CMP chambers, within 2.5° of an extrapolated $\geq$4 GeV/c track
2	`L2_CMUP6_PT8`	and: match between 8 GeV/c track and stub
3	`L3_MUON_CMUP_18`	and: fully reconstructed 18 GeV/c muon track matched in $r\phi$ within 10(20) cm of reconstructed CMU (CMP) stub
1	`L1_CMX6_PT8_CSX`	Muon stub with scintillator coincidence and XFT track with $p_T \geq 8$ GeV/c
2	`L2_CMX6_PT10`	and: match between 10 GeV/c track and stub
3	`L3_MUON_CMX18`	and: reconstructed 18 GeV/c muon track matched within 10 cm of reconstructed CMX stub

Table 3.1: Trigger paths for data used in the top mean lifetime measurement.

Level	Trigger Name	Description
2	`L2_CMUP6_PT8(_&_TRK5)`	`L1_CMUP6_PT4` and match between 8 GeV/c track and stub. In later runs a second, 5 GeV/c track was also required.
3	`L3_CMUP8_TRACK5_ISO`	and: fully reconstructed 8 GeV/c muon track matched in $r\phi$ within 10(20) cm of reconstructed CMU (CMP) stub, && 5 GeV/c track with less than 1.5 GeV track isolation energy within a $0.175 < \delta R < 0.524$ cone.
3	`L3_CMX8_TRACK5_ISO`	`L1_CMX6_PT8(_CSX)` and reconstructed 8 GeV/c CMX muon track matched within 10 cm of reconstructed CMX stub, && 5 GeV/c track with less than 1.5 GeV/c track isolation energy within a $0.175 < \delta R < 0.524$ cone.

Table 3.2: Trigger paths for data used in the τ mean lifetime measurement. The Level 1 muon triggers are identical to those used in the top mean lifetime analysis. For the CMX trigger path, Level 2 was set to automatically accept events on the Level 1 6 GeV CMX trigger. Trigger efficiencies for these paths are described in Appendix C.

Trigger efficiency for t triggers

CDF has measured the efficiency of each of the trigger streams above for events containing good lepton candidates, by finding these leptons in events collected from looser triggers and measuring the fraction of events that also triggered the high-p_T central lepton trigger in question [47, 48]. For electrons, all of the inefficiency is due to the track requirement. With respect to the later offline reconstruction algorithms, the combined electron triggers are $96.2 \pm 0.6\%$ efficient.

For the muons accepted by the filters that we will describe in Chapter 5, the `MUON_CMUP18` stream is $90.8 \pm 0.5\%$ efficient and the `MUON_CMX18` stream is $96.5 \pm 0.4\%$ efficient.

Chapter 4

Event Reconstruction and Simulation

In this chapter we explain the software tools used to interpret CDF data, focusing on the reconstruction algorithms used in this dissertation. We also describe the Monte Carlo event generation scheme used in constructing simulated data samples. The Monte Carlo datasets used to measure detector acceptances and filter efficiencies are described in Section 4.2.

4.1 Algorithms

The triggers described in Chapter 3, along with detector controls and monitoring systems, form the core of the *online* operations, which are systems running in real-time as collisions take place. Online algorithms are optimized for speed. Final analysis of event data uses the typically slower *offline* systems for storing, processing, and reprocessing events which have been flagged for permanent storage.

These systems have access to the raw event data, and usually, to better calibrations than were available to Level 3. Some calibrations, such as the beamline, are calculated offline using a subset of the data for each run. Others such as global detector alignments can be updated whenever the alignment procedure is improved, using stored event data. An ORACLE database system keeps track of consistent sets of calibrations [49].

When good calibrations for a period of data-taking are produced, an enhanced version of the event reconstruction code used at L3, `ProductionExe`, processes all the physics events. Data used for this dissertation was processed with `ProductionExe` version `5.1.0`, although tracks were refit and track-dependent algorithms were rerun with later software to incorporate the best possible alignments and calibrations. Below, we describe important components of this offline software.

4.1.1 Tracking algorithms

This measurement relies on the accurate determination of the lepton track's position when it is nearest the beamline. This distance is measured in the transverse plane, in which the lepton's path is ideally circular. An arbitrary circle of diameter D is expressed in polar coordinates by the relation

$$(D + 2d_0)\sin(\phi + \phi_0) = r + d_0(D + d_0)/r \tag{4.1}$$

as pictured in Figure 4.1. The diameter is often replaced by the curvature $\kappa \equiv 1/D$, since curvature is a small quantity for high p_T tracks that lends itself to polynomial expansions. The distance we are interested in, d_0, is a signed quantity. The diagram

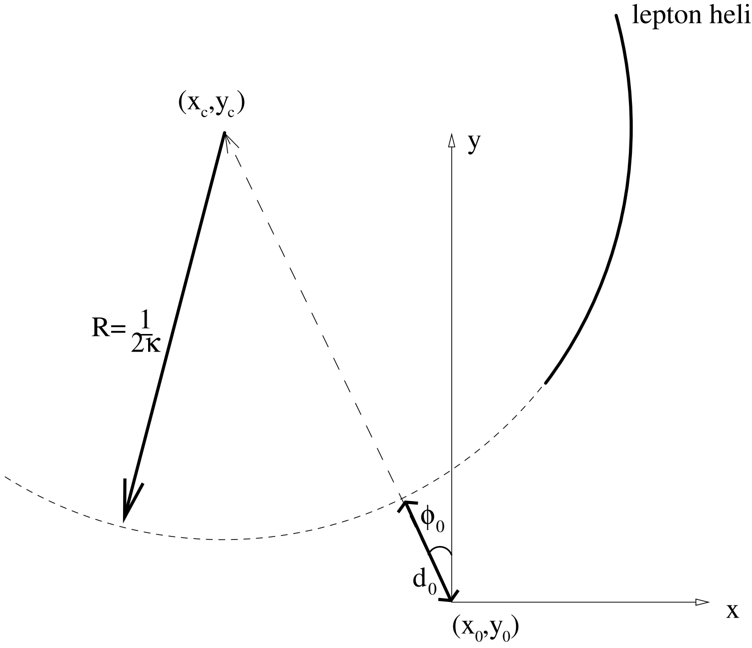

Figure 4.1: The helix parameters defining an ideal track in the $r - \phi$ plane. The diameter of the circle, $D = 2R$, is used in Equation 4.1.

makes explicit the sign convention imposed by choosing d_0 as the smallest distance between the origin and the track, and ϕ_0 as the particle's initial direction. It can be summarized by the relation $\mathrm{sign}(d_0) = \mathrm{sign}((\vec{p}_0 \times \vec{r}_0)_z)$. The track is fully specified once we add the two $r - z$ parameters: the polar angle (θ) and the z-coordinate at $r = d_0$ (z_0).

Tracking detector data is first processed into *hits*, which are generically the two, three, or four space-time coordinates for the intersection of a charged particle and a detector element. Each coordinate is associated with a measurement uncertainty. CDF tracking sensors are all much larger in one spatial dimension than the other two, and therefore only produce two spatial coordinates with useful precision. For generic tracking, the temporal data from COT hits is mostly used to resolve hit positions within a drift cell, as described in Section 3.2.2. Hence, most CDF tracking algorithms associate collections of two-coordinate hits and derive the five spatial helix parameters.

The step of assigning hits to a candidate track is called pattern recognition; in principle it is a different task than *track fitting*, the determination of track parameters from the assigned hits. In practice the two steps often overlap: pattern recognition begins at large radii where the hit density is lowest, then new hits are considered after improved track parameters have been calculated, and the track is refit.

COT pattern recognition Hits in the COT are first used to form track *segments* within superlayers. This procedure uses seeds of three consecutive hits to search for collections of correlated hits within a superlayer, and with a simple drift model calculates the best two-dimensional track passing through the nominal origin of CDF and near the hits. The seed segment direction must be less than about 50° from radial, which essentially disallows tracks with $p_T \leq 355$ MeV/c. These reconstructed segments must have more than five hits to be accepted [50].

Segments are combined into track candidates by two procedures to maximize the pattern recognition efficiency. In *segment linking* [50], the segments of the outermost axial layers are combined if they are consistent with a single track with $d_0 = 0$. These combined segments are fit together to determine d_0, and then other segments near the improved candidate track are added to the fit. *Histogram linking* [51] is a faster algorithm, based on the principle that for a given sign of κ, a single hit determines a unique candidate circle with $d_0 \simeq 0$. A histogram of the distance between the candidate circles from every hit (at some fixed reference radius) will have peaks corresponding to different tracks, and the distance to a segment-based track candidate will peak near zero for hits belonging to that track. Histogram linking is biased toward high p_T tracks. It is the only linking algorithm used for the Level 3 trigger.

All linked tracks are kept for fitting, although the two algorithms create overlapping sets. The candidates are fit in two dimensions using the original $r - \phi$ hit set, using a linear approximation in κ. The linearized track fit is used to look for compatible stereo layer segments in an iterative procedure. Finally, hit positions are corrected with a better drift model, the tracks are refit, and duplicates are pruned.

Outside-in SI hit attachment Adding silicon detector hits to the fits improves the impact parameter resolution $\sigma(d_0)$ by more than a factor of 10. Silicon hits are added beginning from the outermost $r - \phi$ silicon layers, with a branching algorithm [52]: every additional hit creates a new track candidate with adjusted parameters and a new error matrix. The track candidates in this extremely redundant final list are ranked, first by number of successfully added silicon hits, and then by the fit χ^2. Only the best candidates are retained.

Material interactions Charged particles participate in elastic and inelastic interactions with atoms as they traverse the detector. CDF tracking algorithms take the elastic process, which is essentially independent of the incident particle's mass, into account. In COT track finding, the correction is applied by increasing the error associated with hits at larger radius at each stage in the final progressive track fit [50].

The dispersion from multiple elastic scattering varies inversely with particle momentum. In a sample of generic tracks from a high-$\sum E_T^{\rm cal}$ trigger stream, we find that $\sigma_{d_0}^2 = \sigma_0^2 + (56.8)^2/p_T$. The impact parameter resolution for these tracks is plotted *vs.* p_T in Figure 4.2.

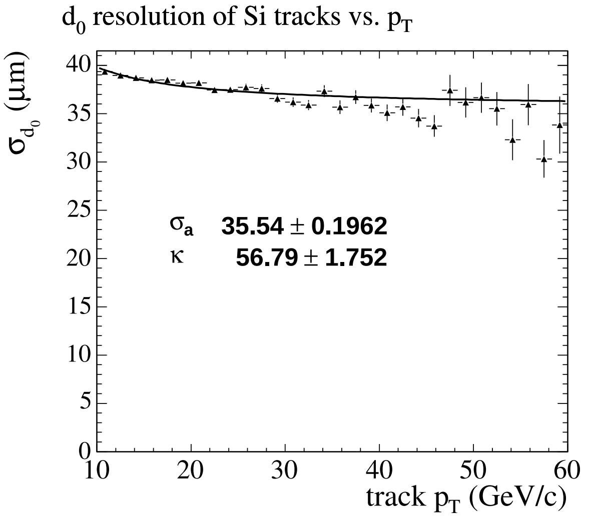

Figure 4.2: Impact parameter resolution vs. transverse momentum for generic high-p_T tracks.

Inelastic interactions affect particles of different masses differently. Using the sign convention explained above, these interactions cause an asymmetric d_0 bias for particles of a given charge: the measured d_0 is positively correlated with the measured curvature κ, and inelastic scattering causes $\Delta\kappa > 0 (< 0)$ for positive (negative) curvature tracks. As Figure 4.3 confirms, such interactions are significant for electron tracks. We must account for different resolutions in the lifetime measurement; resolution functions and background d_0 distributions are measured separately for electrons and muons, as described in Section 7.1.

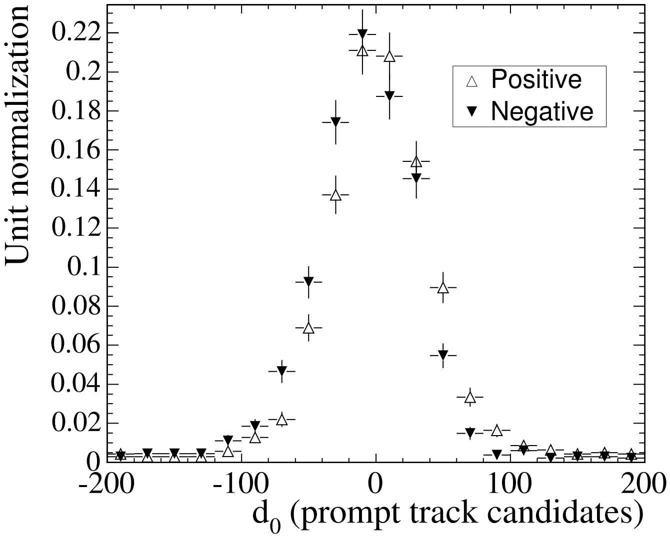

Figure 4.3: The signed d_0^{obs} of good electron track candidates with $d_0^{\text{true}} = 0$. The effect of inelastic scattering on the electrons is evident in the charge bias of d_0^{obs}.

4.1.2 Jet reconstruction

Jet reconstruction begins by calculating the tower energies in the electromagnetic and hadronic sections of each calorimeter. The ADC counts from each photomultiplier tube are converted to an energy measurement using loaded calibrations. Given a primary vertex z position, the tower position can be converted to a relative η, and the energy measurements can be converted to a tower E_T which is used in jet clustering.

Clustering Clustering is performed by the `JetClu` algorithm [53], which finds groups of towers near a sufficiently energetic seed tower in $\eta - \phi$ space and therefore has two important parameters: a seed energy threshold and a definition of nearness. We use $E_{\text{seed}} = 1$ GeV and define nearness by the *cone size*, which is the maximum allowable value of $\sqrt{(\Delta\eta)^2 + (\Delta\phi)^2}$. We use a cone size of $\Delta R_{\text{cone}} = 0.4$ rad.

The algorithm begins by selecting towers with energy greater than E_{seed}, which define an initial jet center (η_0, ϕ_0). The towers within a circle of radius ΔR_{cone} about this center are included in the jet candidate. The centroid position of this tower set, (η_c, ϕ_c) is then calculated as

$$\begin{aligned} \eta_c &= \frac{1}{E_{\text{cluster}}} \sum_{\text{tower}=1}^{N_{\text{towers}}} \eta_{\text{tower}} E_{\text{tower}} \\ \phi_c &= \frac{1}{E_{\text{cluster}}} \sum_{\text{tower}=1}^{N_{\text{towers}}} \phi_{\text{tower}} E_{\text{tower}} \end{aligned} \tag{4.2}$$

This procedure is iterated with the substitution $(\eta_0, \phi_0) \rightarrow (\eta_c, \phi_c)$ until the centroid is stable.

The method has drawbacks which complicate the calculation of jet multiplicities for various processes. The use of a single seed tower means that the number of observed jets is not robust with respect to small changes in geometry such as dividing one tower's energy over two adjacent towers. Jets can also be connected by soft radiation between them, which moves the centroid and leads to a merged jet. Because of this, the correspondence between N_{jet} and N_{parton} for a given process is best reflected by detailed event generation and detector simulation.

Energy corrections The measured jet energies vary with experimental conditions in an undesirable way. Some of the effects are instrumental: while the variation of calorimeter tower response is corrected online by the DAQ to within 3%, residual tower corrections must be applied offline. Moreover, particles need not be produced by a jet to end up within the jet cone. Extra particles from the *underlying event* and from overlapping $p\bar{p}$ collisions[1] during the same beam crossing will increase measured jet

---

[1] These are termed "multiple interactions" at CDF but the usage is not universal.

energies. On the other hand, jet energies will decrease if the cone does not fully contain the parton shower, if particles traverse the entire calorimeter without depositing all of their energy, or if some particles fall in uninstrumented regions of the calorimeters such as the gaps for waveguides and the space between arches.

These effects can be corrected for using a series of calibration measurements [54]: comparing Z masses reconstructed with electrons to the world average, relating the energy deposition of isolated muons to their momenta, measuring tower energy in null-trigger events, and balancing the E_T of opposing jets in dijet events. Corrected jets should approximate the energy of the final state of a parton shower well, but we do not attempt to compensate for the effects of jet fragmentation itself. Especially, the same corrections are applied to b jets and light quark jets, although on average less of a b parton's energy is visible in the calorimeter because it can decay to neutrinos and muons.

4.1.3 Secondary vertex tagging

Bottom and charm quarks form hadrons which are often long-lived, decaying in the detector after traveling several millimeters. The tracks produced in these decays should intersect at their production point rather than the interaction region, so the reconstruction of such a *secondary vertex* allows b and c jets to be identified. For this measurement, top events were identified using the secondary vertex tagging algorithm SecVtx [55].

SecVtx looks for displaced vertices by first finding displaced tracks, and then tests if the transverse distance between the vertex and the interaction point (L_{2D}) is significant with respect to the measurement errors. Tracks within a jet[2] are used if their impact parameter significance ($\frac{d_0}{\sigma_{d_0}}$) is greater than 2.0, and they have $p_T > 500$ MeV/c. They must also begin inside the beampipe and not form part of a K^0 or Λ candidate, which is an opposite-sign pair of tracks with invariant mass near 0.498 or 1.11 GeV/c^2.

The algorithm makes two attempts ("Pass 1" and "Pass 2") to form vertices from the selected tracks. The first Pass attempts to build a three-track vertex starting from the best pair of tracks. Other tracks consistent with the intersection of the first two tracks are all added to the vertex. Then the tracks contributing $\Delta\chi^2_{\text{fit}} > 50$ to the three-dimensional vertex fit are removed, one by one. If an acceptable three-track vertex remains, it is retained; otherwise the next pair of tracks is used as a seed.

If Pass 1 exhausts the possible seeds without creating a vertex, tracks with ($\frac{d_0}{\sigma_{d_0}}$) less than 3.5 or $p_T < 1.5$ GeV are removed from the list. The second Pass then tests two-track vertices from the remaining list against a more stringent set of cuts. If a pair is found with $\chi^2 < 50$ it is retained.

The vertex returned by either Pass 1 or Pass 2 must satisfy $L_{\text{2D}}/\sigma_{L_{2D}} > 7.5$ to be considered a *tag*. Tags can be positive or negative, depending on the sign of the two-dimensional dot product $\vec{r}_{\text{vtx}} \cdot \vec{p}_{\text{jet}}$. A long-lived particle moving in the jet direction will produce a positive tag. The algorithm is intrinsically unbiased to this sign, so false vertices should be uniformly distributed, and the probability of negative tags should equal the probability of false positive tags, or *mistags*. In fact, this symmetry is broken. The hadron mass cuts and the vertex radius cuts are designed to alleviate

---

[2] Tracks are part of a jet if $\sqrt{(\eta_{\text{track}} - \eta_{\text{centroid}})^2 + (\phi_{\text{track}} - \phi_{\text{centroid}})^2} < 0.4$, and if their z_0 is within 2 cm of the z_{PV} used for clustering the jets.

the bias toward forward-going mistags.

Mistags We define mistags as positive tags in light flavor jets. The probability of such a tag is important in calculating the non-$t\bar{t}$ background in our final dataset. The negative tag probability is useful for measuring the mistag rate, but we have already noted a source of error in this identification: material interactions, $\gamma \rightarrow e^+e^-$ and light hadron decays increase the number of positive tags in light flavor jets. Moreover, negative tags are more than twice as probable in heavy flavor jets as light flavor jets [56]. The negative tag probability is increased because there are more tracks candidates with large d_0 in the heavy flavor jet, and because tracks from two distinct vertices in the jet can be combined to produce a negative tag.

Because of these concerns, the average mistag probability for a jet should be measured using the positive tagging rate in a pure sample of light flavor jets. Such a sample is impossible to construct. In impure samples the *negative* tagging rate is a better approximation, since the increase in the positive tag rate for a given heavy flavor contamination fraction is much larger than the negative tag rate increase. We use generic jet samples with little heavy-flavor contamination and correct the negative tag rate for the two sources of error mentioned above. We also parameterize the mistag probability as a function of jet $\eta, \phi, E_T, N_{\text{tracks}}$ and the event $\sum E_T$, since the mistag probability depends strongly on these variables [57, 56].

4.1.4 Lepton reconstruction

Our measurement uses the properties of the track matched to the lepton candidate in $t\bar{t}$ events. In this section we summarize the identification of leptons and the matching of candidates to tracks.

Electron

Electrons are first clustered in the electromagnetic calorimeter by searching for a seed tower and allowing nearby towers to be added to form a cluster if their energy exceeds some threshold. In electron reconstruction the cluster is not allowed to be wider than three towers in η, or one in ϕ.

To find electrons, the tracks are extrapolated through the solenoid to the CES detector. The track position at the CES is used to seed a strip and wire clustering algorithm, which compares signal shapes in the chamber to a template from electron test beam data and adjusts the center accordingly. If the CES profile matches the template well, it passes electron candidate cuts, and the highest p_T track in the region is used as the electron track. The electron energy and the position of the electron track at the electromagnetic calorimeter is also used to calculate L_{shr}, a tower lateral energy sharing test variable. L_{shr} is defined as

$$\frac{\sum_{towers}(E_{\text{meas.}} - E_{\text{pred.}})}{\sqrt{0.196 E_{\text{EM}} + \sum \sigma(E_{\text{pred.}})^2}} \tag{4.3}$$

and tests the hypothesis that the tower energies are created by a single electron [58].

Conversion electrons Conversion electrons originate in the electromagnetic interaction of a photon and atomic field, as pictured in Figure 4.4. All electrons are checked to see if they might be conversions, by looking for an oppositely-charged track which is less than 0.2 cm away at the point where the tracks are parallel [59]. The two tracks must also be nearly parallel in the $r - z$ plane, satisfying $|\cot\theta_1 - \cot\theta_2| < 0.04$.

If exactly one track matches, the electron is labeled a conversion; more than one matching track is taken to be the conversion of a *bremsstrahlung* photon, which often produces tracks that match the track that radiated it. Such an event, shown in the second panel of Figure 4.4, is termed a *trident*. The efficiency of this procedure for identifying high-p_T conversion electrons is discussed in Appendix B.

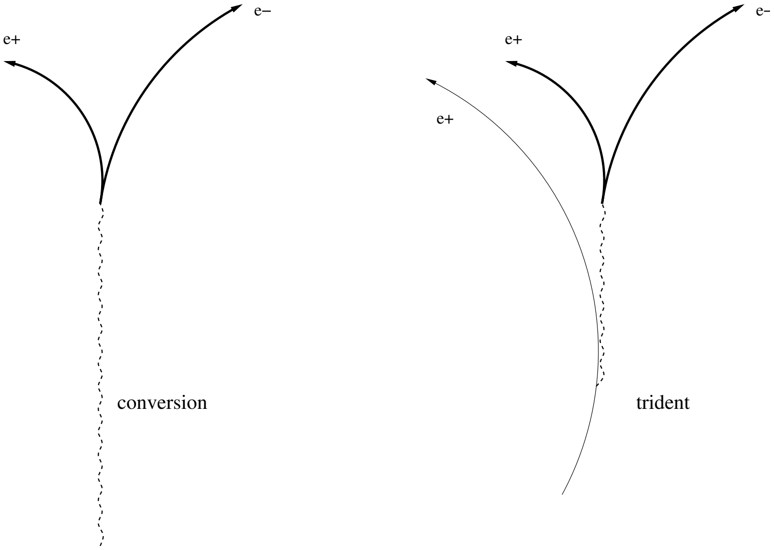

Figure 4.4: Illustration of conversion and trident electrons. Left: conversion pair production by a photon. Right: A conversion pair radiated from a positron. The three tracks can be recognized as a trident.

Muon

Muon TDC times are first converted to hit positions with twofold ambiguity, using a drift model that represents the chamber geometry. CMU hits are each recorded in two chambers; the chamber with the larger charge measurement is the correct match, and a z position can be extracted from the ratio of recorded charges [60]. In general, muon stub finding is much like COT tracking, except that the segment has no curvature. A trivial drift model is first used to collect hits, and then stubs are fit in either two or three dimensions, depending on the detector. Tracks are matched to muon stubs if the track extrapolated to the muon detectors is within about 10 cm in $x \equiv r \cdot \phi$, although these cuts are usually tightened for specific analyses. In the CMU, a z match is also required.

Hadronically decaying tau

Hadronically decaying τ leptons are characterized by a few stable hadrons confined to a narrow cone, the size of which is inversely related to the tau E_T. Taus, like jets and electrons, are reconstructed by first clustering calorimeter towers. Since τ cones are narrow, the seed tower energy threshold is typically larger than the jet seed threshold. The highest p_T track in a cone of $\Delta R = 0.4$ around the cluster becomes the seed track, which is used to define the z vertex for τ reconstruction. Tracks and CES clusters consistent with neutral pions within a cone of size $\Delta R \propto 1/E_T^{\mathrm{cluster}}$ about the seed direction are associated with the τ candidate. These can be used to refine the cluster-based E_T measurement, which is simply $E_T^{\tau} = E_{\mathrm{cluster}} \cos\theta_{\mathrm{seed}}$ [61].

Since the τ has unit electric charge, jet backgrounds can be reduced by $\sim 50\%$ by requiring an odd number of tracks in the τ cone: our τ lifetime analysis (described in Appendix C) requires exactly one or three.

Isolation Most energetic particles created at CDF are formed within jets, so the total energy in a surrounding $\eta - \phi$ cone usually exceeds the particle's energy. This surrounding energy is basically absent in the decay of real $W^{\pm}$ and Z^0 bosons to leptons, because leptons and electroweak gauge bosons are color-neutral. This fact forms the basis of a powerful discrimination tool between high-p_T leptons from these electroweak processes and the tracks that mimic them, the isolation cut.

There are three definitions of the isolation cut used in this analysis. For electrons and muons, the standard *calorimeter isolation* I is defined as the ratio $(\sum_{\Delta R=0}^{0.4} E^{\mathrm{cal}} - E_\ell^{cal})/E_\ell$. For tracks, the *track isolation* I_{track} is the ratio $(\sum_{\Delta R(\mathrm{i})=0}^{0.4} p_T^i)/p_T^{\mathrm{track}}$. We use I_{track} only to identify leptonically decaying taus in the τ lifetime analysis of Appendix C. In the same analysis, we define the *hadronic tau isolation* as $(\sum_{\Delta R=R_{\mathrm{min}}}^{0.4} E^{\mathrm{cal}} - E_\ell^{\mathrm{cal}})/E_\ell$, where R_{min} is the energy-dependent tau cone size. This definition excludes the tau decay products from the isolation energy.

4.2 Event simulation

Event generation

We can model elementary particle collisions by determining the probability distributions for the observables in various final states (from the calculated matrix elements, for example), and selecting outcomes from these distributions using a random number generator. We use this *Monte Carlo* event generation method to model both signal and background processes. In Chapter 2 we pointed out the difficulty of calculating matrix elements for collisions involving hadrons. The Monte Carlo therefore uses several distinct approximation schemes. The first approximation is the use of finite order expansions of differential cross sections for the *hard scattering* between partons. These differential cross sections are stored in a library of the event generator, and are often averaged over observables such as polarization.

The second set of approximations is used to model the more complex QCD elements of the collision. First, the incoming hadrons are described by measured parton distribution functions, as discussed in Section 2.1.1. The incoming partons in the hard scattering are evolved backward from the interaction momentum scale Q^2 down to the scale of the stored PDFs by *parton showering,* a process modeled by enabling 1→2 branchings[3] such as $g \to q\bar{q}/g\bar{g}$ and $q \to qg$. This process creates the additional partons which would only be included by higher order matrix elements in perturbative QCD. The final state is also evolved down to the non-perturbative QCD scale by final-state parton showering. Finally the outgoing partons are *hadronized* to form the color-neutral particles of the final state.

We use two general-purpose programs for Monte Carlo event generation, PYTHIA [62] and HERWIG [63]. These differ slightly in the kinematics of parton showering, and also in the description of hadronization. Occasionally, we use higher-order matrix element calculations from the ALPGEN [64] program as input to HERWIG, which performs the parton showering and the hadronization of ALPGEN events. Full event generation results in a set of stable and metastable particles, their initial positions, and initial momenta. The *event record* also includes all of the intermediate particles, and describes the lineage and descendants of each.

Detector simulation

The list of metastable particles is passed to a description of detector elements based on GEANT [65], which simulates the propagation of particles through detector materials. For each detector element, there is a simulation based on microscopic

---

[3] In our Monte Carlo generators, electromagnetic interactions are also included by showering.

interactions or parameterizations of test-beam data, which ultimately produces an output bank functionally identical to the bank produced by the online DAQ. Our simulation events are based on a run number corresponding to a collider data run, so that calibrations, alignments and channel maps can be applied. The purpose of this method is to accurately replicate datasets, including the variable conditions under which data is collected [66]. The simulated events are reconstructed the same way as collision data, with one exception: the trigger is not applied to simulations in our t lifetime analysis. For this reason there are cuts on the final dataset to either confirm trigger decisions or exclude events that would not be fiducial to the trigger.

4.2.1 Monte Carlo datasets

The Monte Carlo datasets used in this analysis are listed in Table 4.1. We apply two corrections to the Monte Carlo modeling of electroweak interactions: because these $W^{\pm}$ and Z^0 samples combine ALPGEN and HERWIG, the inclusive cross sections represented for these processes are difficult to normalize. We scale the predictions for $W^{\pm}$ and Z^0+jets events to match the number of those events found in the data. We also correct the probability of finding heavy flavor quarks from higher-order QCD interactions in $W^{\pm}$ events, which has been shown to be underestimated by the ALPGEN+HERWIG simulation [67].

Monte Carlo for τ mean lifetime measurement

Because the tau and muon track isolation variables are especially luminosity dependent, we use special Monte Carlo datasets that simulate the luminosity conditions

Process	Monte Carlo sample		description
	electrons	muons	
$W \to \ell\nu$	`atop[a,5..7]a`	`atop[c..f]b`	Alpgen hard scattering followed by Herwig fragmentation
$Z \to \ell\ell$	`atop[3..6]z`	`ztop2i`	e: Alpgen hard scattering followed by Herwig fragmentation; μ: Pythia leading-order matrix element and fragmentation
$W \to \tau\nu$	`atop[7..9]t`		Alpgen+Herwig
$t\bar{t}$	`ttopel`		Pythia leading-order
WW	`wtop1w`		Pythia leading-order
WZ	`wtop1z`		Pythia leading-order
ZZ	`ztopcz`		Pythia leading-order
s-channel t	`mtopya`		Pythia leading-order
t-channel t	`mtopta`		Pythia leading-order
$Z \to \tau\tau$	`ztop4i`		Pythia leading-order

Table 4.1: CDF database names and descriptions of the Monte Carlo samples used in the top mean lifetime analysis. The samples use the generators indicated, and the CTEQ6M parton distribution functions [9].

of the 2002-2005 CDF data. The signal Monte Carlo $Z^0/\gamma^* \rightarrow \tau\bar{\tau}$ events were generated using Pythia, with a dilepton mass threshold of 20 GeV. Tau decays are generated using Tauola, a routine that produces the correct angular correlations [68]. The run-dependent Monte Carlo for the τ analysis not only replicates the silicon detector status but also the luminosity-dependent multiple interaction multiplicity. The $W^\pm \rightarrow \mu\bar{\nu}$ and $Z^0/\gamma^* \rightarrow \mu\bar{\mu}$ background datasets for the τ analysis are generated with similar prescriptions.

Monte Carlo for QCD studies

No Monte Carlo sample is used to simulate the QCD background in the top or tau mean lifetime measurements. However, Herwig inclusive $2 \rightarrow 2$ QCD scattering simulations filtered for an 8 or 9 GeV lepton after event generation are used to check and parameterize impact parameter distributions of leptons from semi-leptonic b and c decays.

Chapter 5

Data selection

In this chapter we describe the offline selection of events that we will use to measure the top quark lifetime. We use a sample of leptonically decaying $W^{\pm}$ bosons in events with multiple high p_T jets. In Section 5.1 we explain this specific combination of leptons, missing energy, and jets. In Section 5.2 and 5.3 we describe the cuts which select acceptable events and define these objects. We conclude with a summary of the accepted data.

5.1 The W+jets sample

As discussed in Chapter 2, the largest number of t quarks produced in hadronic collisions are created through the interactions $q + \bar{q} \rightarrow t\bar{t}$ and $g + g \rightarrow t\bar{t}$. In this analysis we wish to study t decays to $W^{\pm}b$ in which $W^{\pm} \rightarrow \ell\bar{\nu}$, where ℓ represents an electron or muon[1]. However, $W^{\pm} \rightarrow q\bar{q}'$ is more common, so we have selected a

---

[1] Because τ leptons are unstable and long-lived ($c\tau_{\tau} \simeq 87\mu$m), they are poor indicators of the $W^{\pm}$ decay position. We do not attempt to include them in the event selection.

sample of events with one hadronic $W^\pm$ decay and one leptonic $W^\pm$ decay.

The preferred final state thus consists of two b jets, two other jets from the $W^\pm \to q\bar{q}'$ decay, a high-p_T lepton, and large missing transverse energy ($\not\!\!E_T$) indicating an undetected neutrino. Jets may escape detection and gluon radiation can create additional jets, so it not efficient to demand exactly four. To qualify as a $t\bar{t}$ candidate, we require the following *event-level cuts*:

- exactly one good central ($|\eta| < 1$) electron or muon candidate, which is energetic (with $E_T > 20$ GeV/c^2) and isolated (as explained in Section 4.1.4),
- Missing transverse energy ($\not\!\!E_T$) exceeding 20 GeV, and
- at least three reconstructed jets with $|\eta| < 2.0$. These jets' transverse energy must be greater than 15 GeV and at least one must be tagged with the secondary vertex tagger (SecVtx).

There is an important superset of these events obtained by removing the requirement of a secondary vertex tag. Because (as discussed in Chapter 6) most events in this larger sample are direct $W^\pm$ production with QCD radiation, it is called the W+jets sample. We will also refer to it as the *pre-tag* sample.

Figures 5.1 and 5.2 show the expected distribution of $t\bar{t}$ signal events in several event-level variables.

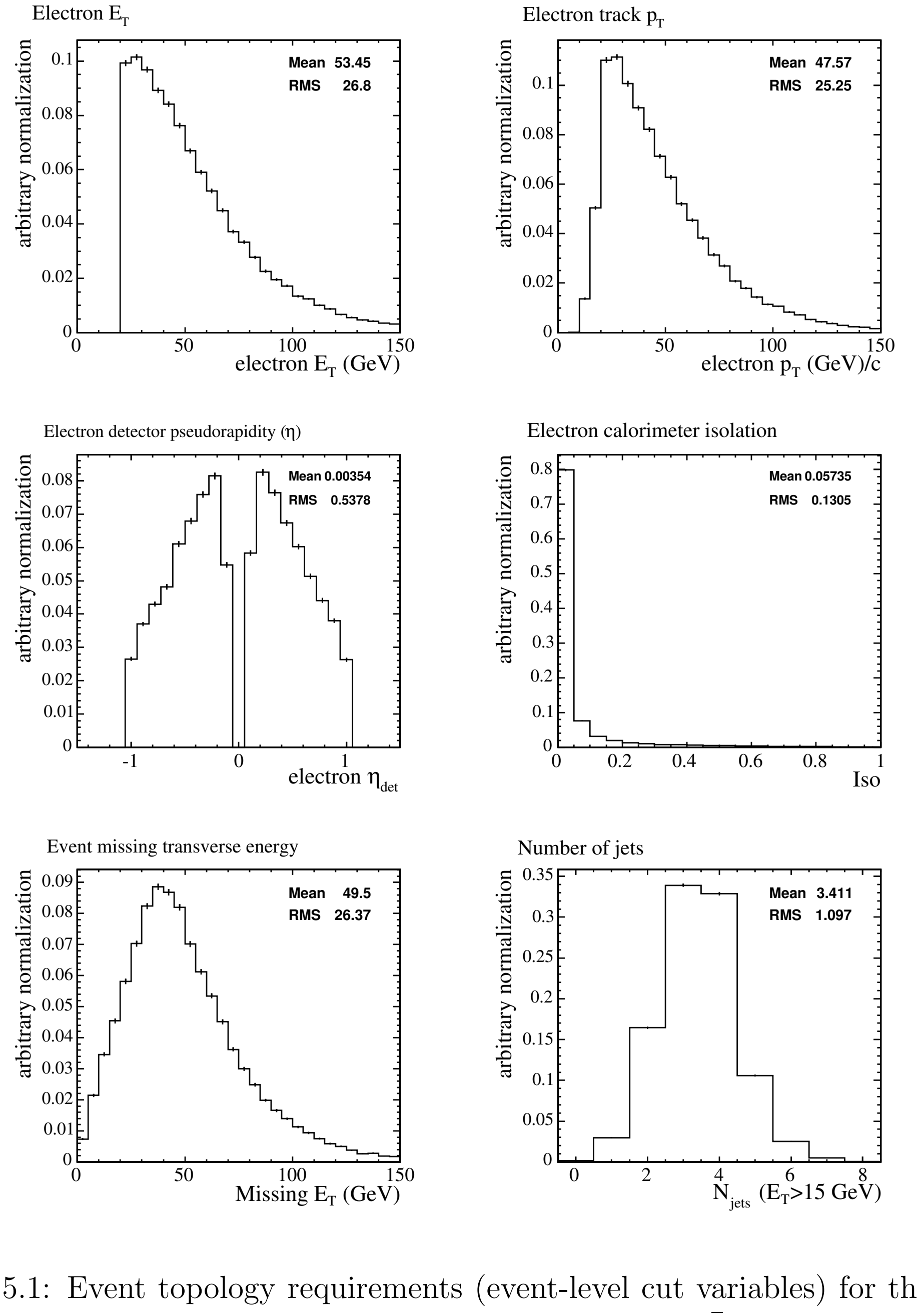

Figure 5.1: Event topology requirements (event-level cut variables) for the $t\bar{t}$ signal simulation. These distributions from simulated $p + \bar{p} \rightarrow t\bar{t}$ events with an electron candidate were created with the Pythia Monte Carlo generator and the full detector simulation.

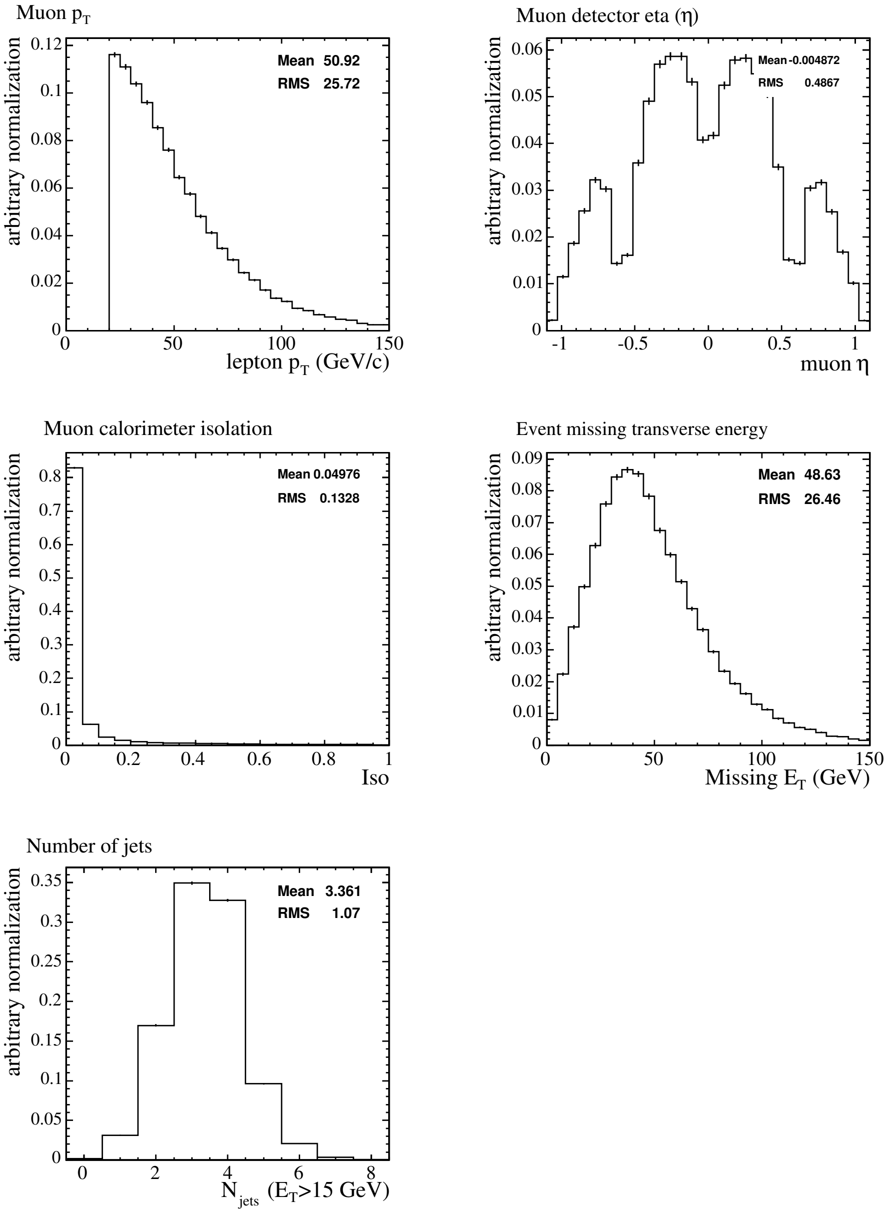

Figure 5.2: Event topology requirements (event-level cut variables) for the $t\bar{t}$ signal simulation. These distributions from simulated $p + \bar{p} \rightarrow t\bar{t}$ events with a muon candidate were created with the PYTHIA Monte Carlo generator and the full detector simulation.

5.2 Event reconstruction requirements

5.2.1 Detector status

The trigger and reconstruction software can compensate for a finite number of *known* overactive or unresponsive sensors for each detector system, but unflagged hot or dead channels can lead to spurious triggers and event misreconstruction. We use the `GoodRun v.7.0` list [69] to reject all events from a run if the COT or silicon tracking, the CES detector, or the muon chambers were not properly operating during the run. Because the CMX muon detectors were fully commissioned five months after the silicon detectors, we only accept events from those early months if the primary lepton is not reconstructed from CMX hits. These `GoodRun` requirements not only reduce the effective luminosity of the CMX lepton dataset from 318 pb^{-1} to 305 pb^{-1}, but also exclude a three-month period of data-taking during which wire aging in the COT reduced the gas gain in some regions. While a solution was being developed, some superlayers were operated at a lower electrostatic potential [70].

5.2.2 Interaction point requirements

The collision point is found by fitting three-dimensional tracks to a common z-vertex position. To accept an event, a good[2] z vertex must be found. Such a vertex can be formed by one track, but only if it is the highest p_T COT track in the event. Otherwise, the sum of track weights in the vertex must be 12 or greater. Tracks with a good fit χ^2 and small $|d_0|$ (<1 cm) that are consistent with the vertex z are weighted

---

[2] “Class 12,” in CDF terminology.

with the following prescription:

- COT tracks with ≥ 3 axial and ≥ 3 stereo segments: weight = 6
- silicon-based tracks with ≥ 5 axial and ≥ 3 stereo hits: weight = 4
- tracks with ≥ 2 axial and ≥ 2 stereo COT segments, and ≥ 2 axial and ≥ 2 stereo silicon hits (failing the cuts above): weight = 2

Due to multiple collisions in the same beam crossing there is often is more than one good z-vertex: we rank these candidates by the scalar $\sum |p_T|$ over all associated tracks, and choose the z_0^{event} to be vertex with the highest p_T sum within 5 cm of the lepton's track. To ensure that the event is well-contained in the fiducial region of the detector and consistent with the luminous region at CDF, z_0^{event} must fall between -60 and 60 cm. The efficiency of this cut is 95.5 ±0.3% [71].

5.2.3 Background rejection

The backgrounds to $t\bar{t}$ production in our sample are described in Chapter 6. Here we summarize some event-level cuts designed to remove distinct backgrounds.

Dilepton veto

We remove events in which a second lepton passes all lepton identification requirements, or all lepton identification requirements excluding the isolation cut. Such events pertain to top events of the $\ell\nu b\ell\bar{\nu}\bar{b}$ topology, or to other backgrounds. For $t\bar{t} \rightarrow \ell\nu bq\bar{q}'\bar{b}$ events with three identified jets, this cut is over 99% efficient.

Z^0 decay veto

Energetic isolated leptons are produced copiously in pairs by the Drell-Yan process, especially at the Z^0 resonance. Some such events pass the N_{jet} and missing energy requirements listed above. To reduce this background, we do not allow any lepton candidate to belong to a pair of same-flavor leptons with invariant mass between 76 and 106 GeV/c^2. The second lepton can can have have p_T as low as 10 GeV/c and fail many lepton identification cuts: leptons associated with tracks must have opposite charge and isolation ≤ 0.15, but trackless electrons with $E_T < 10$ GeV and hadronic to electromagnetic energy ratio ≤ 0.12 are also considered in the veto. The efficiency of this cut for generic $t\bar{t}$ events which have not already been removed by the dilepton veto is 97.0 ±0.1% for muons and 95.4 ±0.1% for electrons. The underefficiency of this background removal filter is studied with Monte Carlo simulation, as discussed in Chapter 6.

Conversion veto

Electrons in the signal sample are required not to form conversion candidates with any reconstructed track, unless the conversion can be classified as a trident. The conversion and trident identification algorithm is described in Section 4.1.4. 5% of the electrons in the data sample are identified as tridents. No conversion veto is applied to simulated $t\bar{t}$ events.

Cosmic ray veto

Muons produced in the atmosphere by cosmic rays frequently cross the CDF detector, and occasionally coincide with a beam crossing. These muons are typically isolated, and hence likely to enter the $W^{\pm}$+jets sample. Tracking information and the timing of hits in the TOF and hadronic calorimeter TDCs are used to reject muons from cosmic rays [35]. Cosmic muons are not correlated with the event z_0, so muons are rejected when they are more than 4 cm in z from the event primary vertex. If they happen to pass near the interaction point, they can be interpreted as a pair of oppositely charged muons, because the curvature of the track moving toward the beam will be misinterpreted. Often the inward-moving leg will be missed, because the flight time correction applied to the COT hits will have the wrong sign. Cosmic ray events are an important background to understand because there is no correlation between the muon track and the beam axis for muons produced by cosmic rays. The lepton's impact parameter distribution is intrinsically flat, like the distribution of t decay leptons as $c\tau_t \to \infty$. This poses an obvious danger to the lifetime measurement sensitivity, so we study the veto efficiency in Section 6.1.6.

5.3 Lepton selection

5.3.1 Electron identification

Electron candidates are first constructed by the algorithm described in Section 4.1.4. They are then filtered to reduce backgrounds and ensure good energy reconstruction. The track is required to be near the CES cluster in z and in "local x," the $r\delta\phi$ coordinate[3]. Candidates near detector boundaries are rejected. To reduce jet backgrounds, candidates with large hadronic energy depositions in the towers of the electron cluster are also removed. The candidate is required to have L_{shr} (the tower profile variable explained in Section 4.1.4) less than 0.2.

Because of the high probability of *bremsstrahlung*, the electron energy cut is applied to the total cluster energy, and the track p_T can be as low as 10 GeV/c. The ratio E/p is required to be greater than 2. All of the electron kinematic and quality requirements are expressed in Table 5.1.

Figure 5.3 compares distributions of the identification quantities listed in Table 5.1 for electrons from the `ELECTRON_CENTRAL_18` dataset to distributions for simulated electrons from top events. For the real electrons in this comparison, we use a very pure Z^0 sample: in the event there must be another electron that passes the cuts in Table 5.1 and has opposite charge, such that $76 < |m_{e^+e^-}| < 106$ GeV/c^2. Some obvious differences between the simulation and the CDF data distribution are evident in Figure 5.3, especially the plot of CES Δ_Z. Such discrepancies lead to a difference in true and simulated electron identification efficiency, which is resolved by a *scale factor* discussed below.

Electron identification scale factor

To correct the discrepancy between simulated electrons and the candidates in the signal sample, the ratio $(SF)_{\text{ele ID}} = \frac{\epsilon_{\text{data}}}{\epsilon_{MC}}$ was measured using a Monte Carlo sample of electrons from Z^0 decays and a 99.85 % pure sample of Z^0 electrons in data. The

---

[3] The position matching in local x is asymmetric, because a radiating electron will bend away from its cluster in the magnetic field.

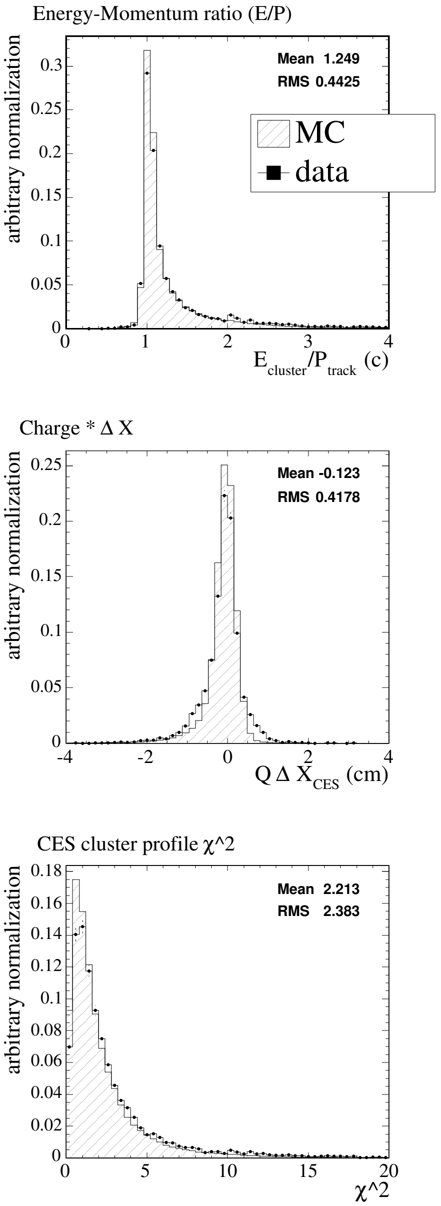

Figure 5.3: Comparison of electron identification variables for real and simulated electrons. The Monte Carlo (shaded) distributions are derived from electrons in our Pythia $Z \to e^+e^-$ simulation, while the overlaid data distributions are plotted using the unbiased electron in the Z^0 sample described in the text. For each data distribution, every identification cut except for the variable being plotted is applied.

ratio for triggerable electron candidates, corrected for backgrounds in data, was found to be 0.996 ±.005 [72].

5.3.2 Muon identification

The muon candidates constructed as described in Section 4.1.4 are subject to quality cuts as well. Muons typically interact very little in the calorimeters, so candidates traversing towers that recorded a large energy deposition are rejected. The extrapolated track position must be consistent with the reconstructed stub position. Since muons in the CMX trigger stream are required to have 4 axial segments of XFT hits, we require that the track pass through at least 4 axial superlayers before exiting the COT. This ensures that CMX muons in the Monte Carlo would be fiducial to the trigger. The complete set of kinematic and quality requirements for muons is shown in Table 5.2.

In Figure 5.4, we compare the distributions of muon identification quantities for muons in data to distributions for simulated muons from top events. Again, we use muons from the Z^0 sample and require them to pass every cut unrelated to the variable being plotted. Discrepancies between the simulation and the dataset necessitate a muon identification efficiency scale factor.

Muon identification scale factor

The correction factor for the efficiency of μ identification calculated in Monte Carlo is derived, as for electrons, by comparing Z^0 candidates to simulation. The efficiency for an exceptionally pure data sample, relative to a Monte Carlo sample of

Electron E_T	$\geq$ 20 GeV
Track p_T	$\geq$ 10 GeV/c
Isolation fraction	$\leq$ 0.1
$E_{\text{cluster}}/P_{\text{track}}$ ($p_T < 50$ GeV/c)	$\leq$ 2.0 c
$E_{\text{cluster}}/P_{\text{track}}$ ($p_T \geq 50$ GeV/c)	no requirement
$E_{\text{hadronic cal.}}/E_{\text{CEM}}$	$\leq 0.055 + \frac{0.00045\text{GeV}}{E}$
$q * \delta X$	$<$ 1.5 cm and $>$ -3.0 cm
$\lvert \delta Z \rvert$	$<$ 3.0 cm
χ^2_{strip}	$<$ 10
$Lshr_{\text{track}}$	$<$ 0.2
"fiducial"	($\lvert X_{\text{CES}} \rvert < 21$ cm, $9 < \lvert Z_{\text{CES}} \rvert < 230$ cm, tower $\neq$ 9)

Table 5.1: Electron identification criteria. The variables used for cuts are described in the text.

Muon track p_T^{corr}	$\geq$ 20 GeV/c
Isolation fraction	$\leq$ 0.1
$E_{\text{had}}(P < 100$ GeV/$c)$	$\leq$ 6.0 GeV
$E_{\text{had}}(P \geq 100$ GeV/$c)$	$\leq 3.20\text{GeV} + .0280 \times P$
$E_{\text{EM}}(P < 100$ GeV/$c)$	$\leq$ 2.0 GeV
$E_{\text{EM}}(P \geq 100$ GeV/$c)$	$\leq 0.95\text{GeV} + .0115 \times P$
CMUP: $\lvert \delta X_{\text{CMU}} \rvert$	$<$ 3.0 cm
CMUP: $\lvert \delta X_{\text{CMP}} \rvert$	$<$ 5.0 cm
CMX: $\lvert \delta X_{\text{CMX}} \rvert$	$<$ 6.0 cm
CMX: $r_{\text{COT exit}}$	$>$ 140 cm

Table 5.2: Muon identification criteria. The energies E_{had} and E_{EM} are the sum of the energies in towers crossed by the extrapolated muon track.

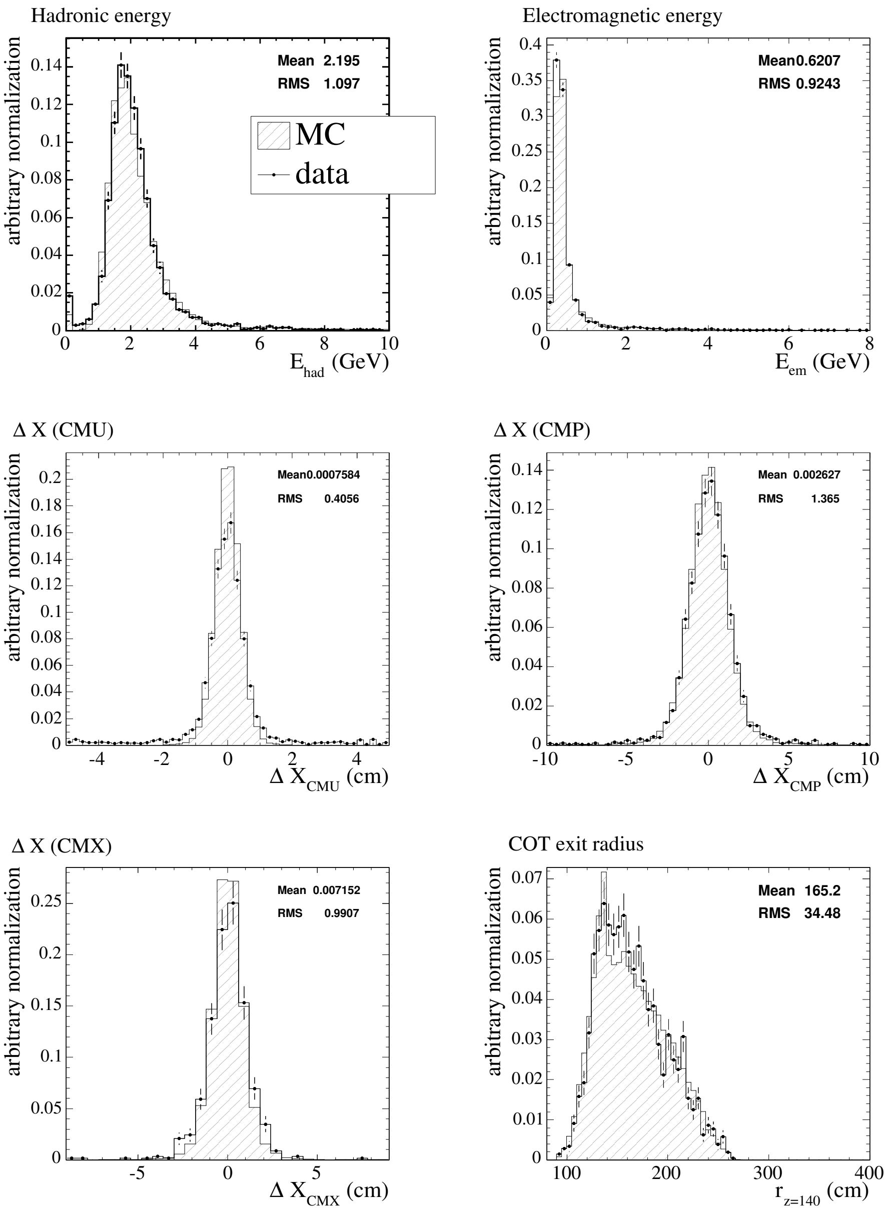

Figure 5.4: Comparison of muon identification variables for real and simulated muons. The CMU and CMP position cuts are both shown for CMUP muons. The Monte Carlo (shaded) distributions are derived from muons in our Pythia $Z^0 \rightarrow \mu^+\mu^-$ simulation, while the overlaid data distributions are plotted using the unbiased muon in the Z^0 sample described in the text. For each data distribution, every identification cut except for the variable being plotted is applied.

similar events, was found to be 0.874±0.009 for CMUP muons and .989±.006% for CMX muons [48].

5.4 Heavy flavor jet identification

We use positively tagged b-jets as defined in Section 4.1.3 to identify $t\bar{t}$ decays. Since tagging depends heavily on track resolution and reconstruction efficiency, we must check that the simulation models the b-tag efficiency well. Monte Carlo simulations used for this analysis are slightly optimistic, a problem we remedy with a scale factor.

To measure the b-tagging scale factor we use a fairly pure sample of heavy flavor jets, selected by requiring that the jet contains a low p_T electron and recoils against a SecVtx tagged jet. This sample is over 70% pure. A complementary sample with low heavy flavor purity is constructed by requiring that the low p_T electron is a conversion candidate: this procedure allows *in situ* background subtraction. The SecVtx correction determined with this procedure is $(SF)_{\text{tag}} = 0.890 \pm 0.038 \pm 0.072$ [73]. A similar measurement using jets containing muons, which determined the background via fits to $p_T^{\text{rel}} \equiv \vec{p}_T(\mu) \cdot \hat{p}_T(\text{jet})$, measured a correction factor of $0.915 \pm 0.017 \pm 0.060$ [74]. These measurements were combined to form $(SF)_{\text{tag}} = 0.909 \pm 0.060$ [75].

5.5 Neutrino identification

Neutrinos rarely interact within CDF and escape detection. Their presence can only be deduced from the nonzero vector sum of the p_T of every observed particle in the event. In the transverse plane, the sum $\sum \vec{p}_{\text{visible}}$ should equal $-\sum \vec{p}_{\text{invisible}}$. We assume there is only one neutrino in the event, and take $p_T^{\nu} = -|\sum(\vec{p_T})_{\text{visible}}|$.

The missing energy sum is best measured in the calorimeter, approximated by $-\sum(\vec{E_T})_{\text{tower}}$ for all calorimeter towers. To compensate for calorimeter non-uniformity, the energy correction applied to all jets with $E_T^{\text{raw}} \geq 8$ and $|\eta| < 2.4$ is also subtracted from the missing energy tower sum. Unclustered energy in towers below the jet energy threshold is not corrected.

The energy of identified muons in the event is visible to the track reconstruction, but little is absorbed by the calorimeter, so another correction can be incorporated in the neutrino reconstruction. We subtract the p_T of good muon candidates from the sum above. The muon energy deposited in the calorimeter is added back to avoid overcorrection.

5.6 Lepton track requirements

A precise measurement of the lepton's production position requires a well-measured track, so we begin with the `defTrack` collection produced by the tracking algorithms described in Section 3.2.2. The `defTracks` are required to have at least five COT hits in two axial layers and one stereo layer. We require an additional stereo layer, as well as three or more hits in the silicon (SVX, ISL, or L00) $r-\phi$ layers. Figures 5.5 and

5.6 show the impact of our filter on `defTrack` tracks. Figure 5.7 indicates the impact parameter resolution improvement attained by requiring more silicon $r - \phi$ hits.

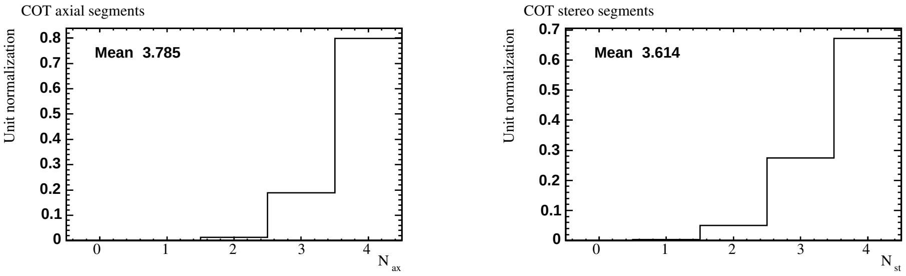

Figure 5.5: Distribution of $N_{\text{superlayers}}$ for COT tracks. These plots are created using lepton tracks in the signal sample, before track quality cuts are applied.

5.6.1 Silicon hit cut scale factor

The Monte Carlo is tuned to reflect the status of silicon detectors on a run-by-run basis, and models the efficiency of the N_{Si} cut well [66]. We use the ratio of this efficiency for leptons in data to that in Monte Carlo to normalize the Monte Carlo predictions of the probability that the leptons pass track quality cuts. We use identified leptons in the Z^0 datasets described earlier to measure the efficiency of this cut. For comparison, we use inclusive Z^0 samples of electrons and muons created by Pythia. The scale factors measured with electrons and muons are consistent, so we use the weighted average: $\frac{\epsilon}{\epsilon_{\text{MC}}} = 1.002 \pm .004$.

Figure 5.8 compares the track η dependence of the efficiency in data and Monte Carlo. The simulation is accurate over the fiducial region.

5.7 Accepted events

The filtering described above yields 157 events from the CDF data stream; 97 are collected from the electron trigger and 60 from the combined muon triggers. Some kinematic distributions of the selected data are displayed in Figures 5.9 and 5.10.

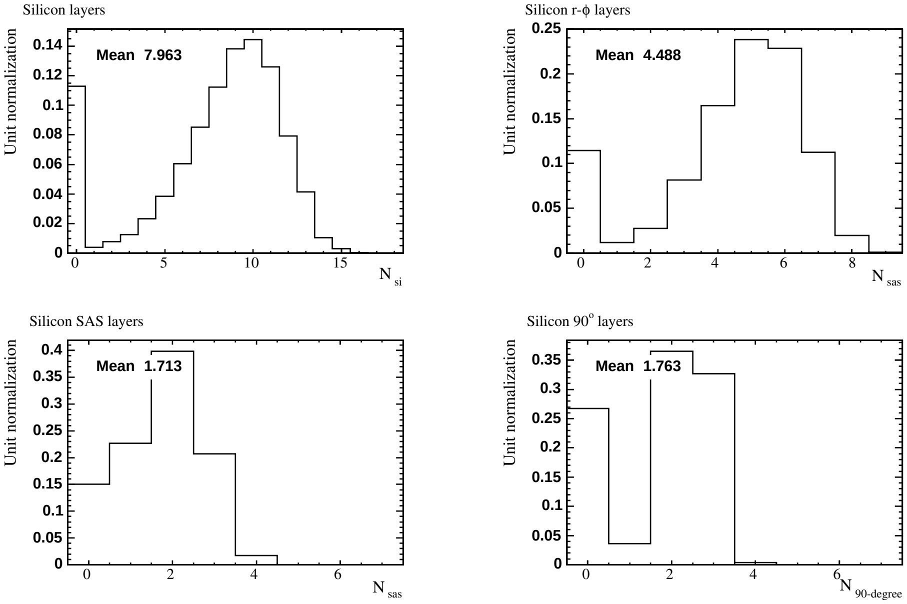

Figure 5.6: Distribution of N_{hits} for SI tracks. These plots are created using lepton tracks in the pre-tag sample, before track quality cuts are applied.

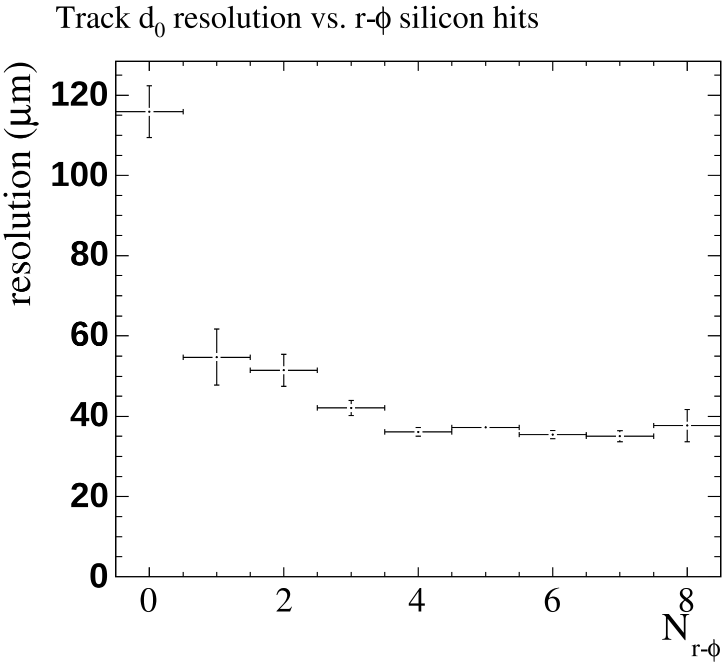

Figure 5.7: The average impact parameter resolution for tracks as a function of the number of axial SI hits. This plot is created using leptons in the pre-tag sample, before the number of axial SI hits cut is applied.

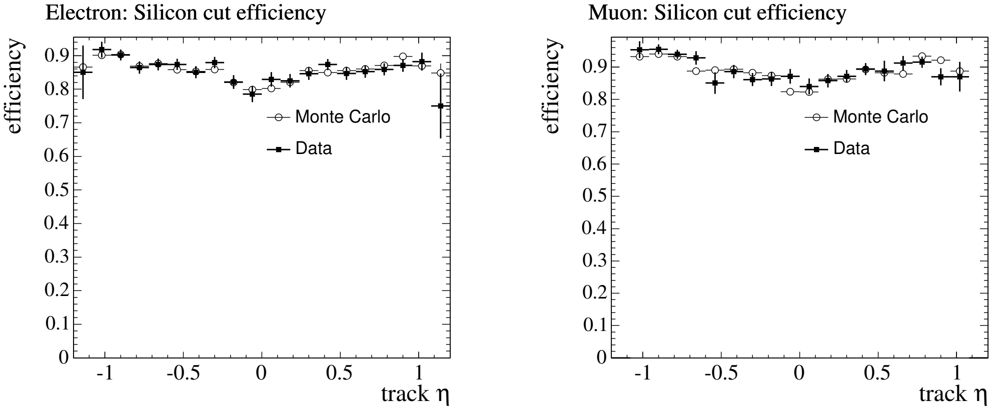

Figure 5.8: Track (event) η dependence of the silicon hit cut efficiency, in $Z \rightarrow \ell\ell$ data and Monte Carlo.

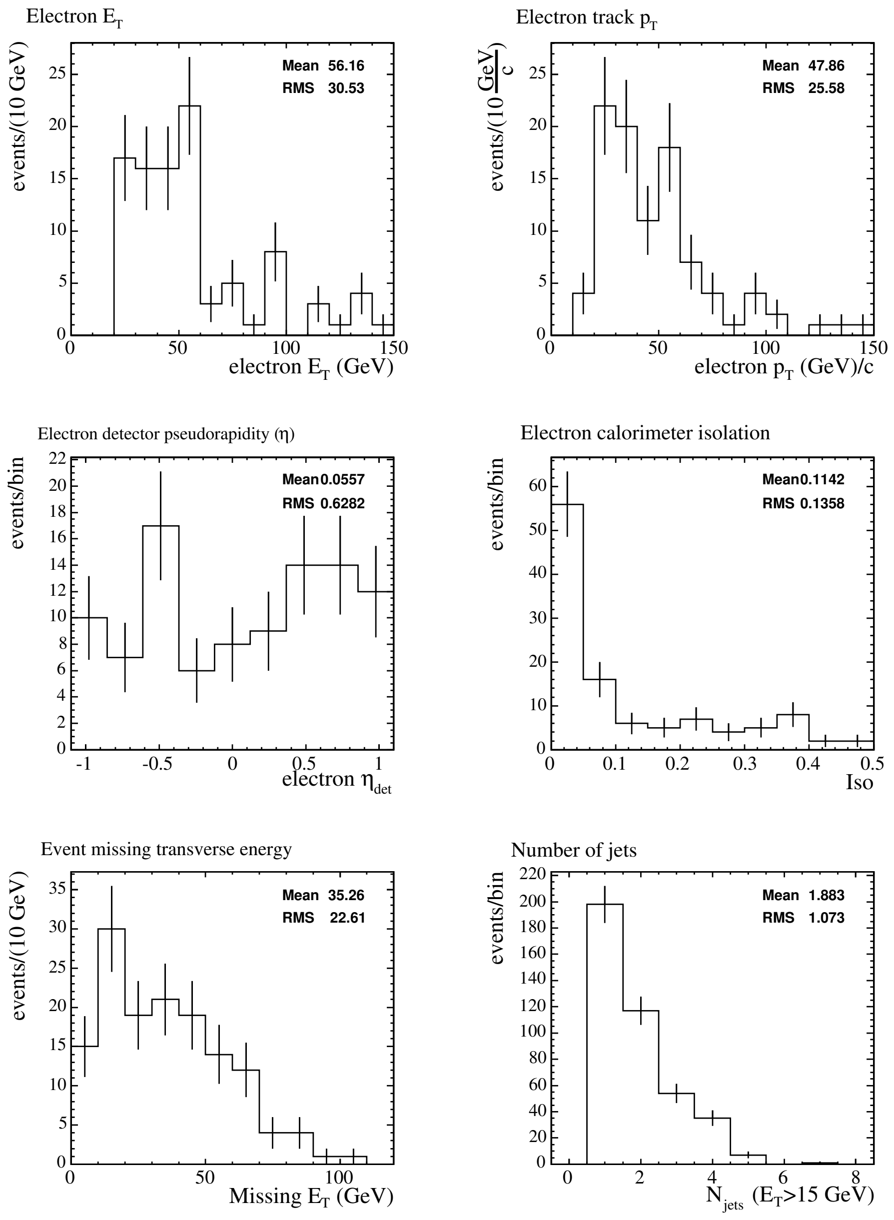

Figure 5.9: Kinematic distributions for electron events in the signal data sample. The first three plots are for selected events; for the last three distributions we relax the cut on the variable being plotted.

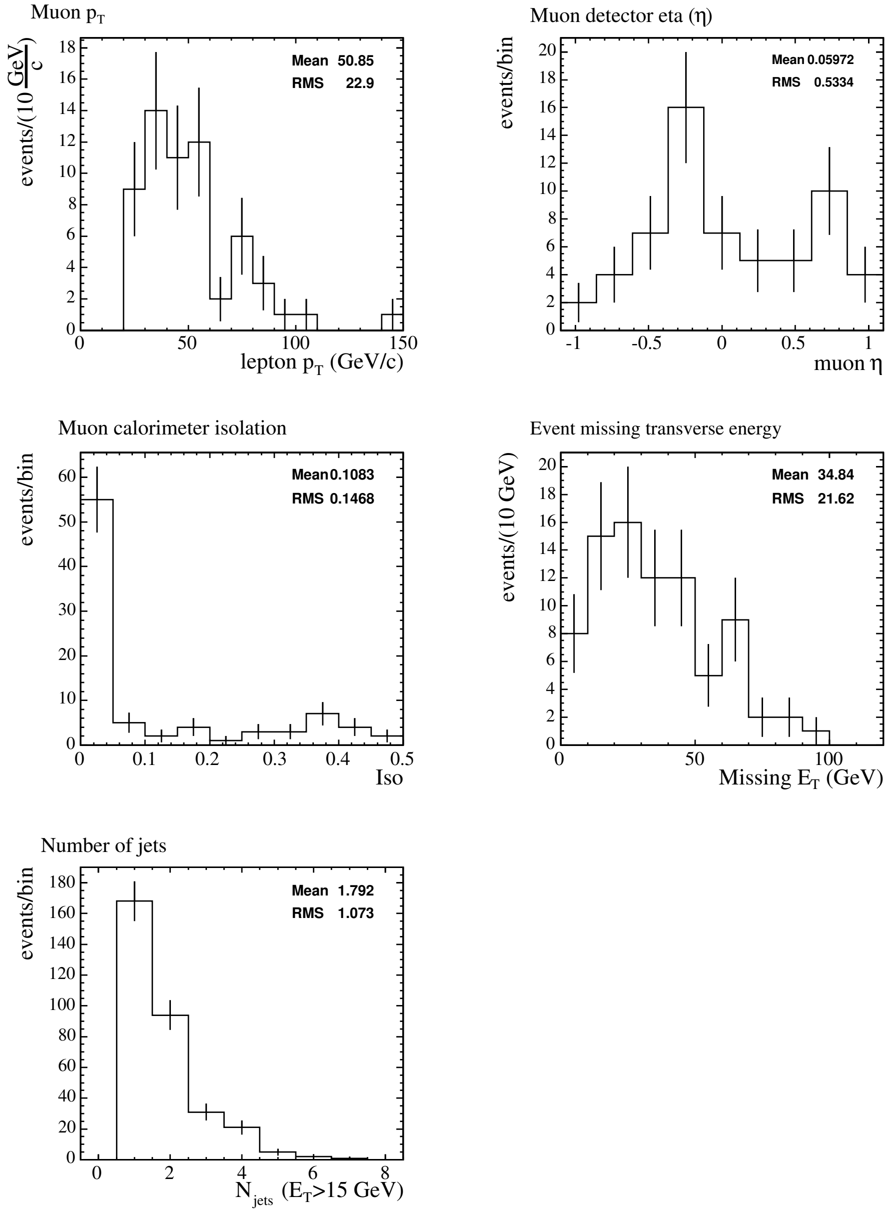

Figure 5.10: Kinematic distributions for muon events in the signal data sample. The first two plots are for selected events; for the last three distributions we relax the cut on the variable being plotted.

Chapter 6

Backgrounds

We derive a sample mostly composed of $t\bar{t}$ events using the selection described in Chapter 5. However, other processes mimic the $t\bar{t}$ signature and contaminate this sample. The largest of these background processes is the direct production of $W^{\pm}$ bosons in association with either heavy flavor jets or mistagged light flavor jets. Other significant backgrounds include electroweak production of heavy boson pairs (WW, WZ, and ZZ) or single top quarks. All of these processes can produce an isolated lepton, large missing energy due to unreconstructed neutrinos or unidentified muons, and several jets through higher order QCD interactions or via gauge boson decays. For these backgrounds, we use Monte Carlo event generators.

Another significant background, in which the isolated lepton is fake, is more difficult to model with our event generation/simulation software. In W+jets nomenclature, a *fake* isolated lepton can

- have fake isolation, if it comes from either the semi-leptonic decay of a heavy quark, the leptonic decay of a light meson, or from a photon conversion, or

- be a fake lepton, such as a hadron that penetrates to the muon chambers or a jet with few tracks and high electromagnetic energy fraction.

When the fake is not produced in a semi-leptonic b or c decay, the missing energy is mostly due to jet mismeasurement. These fake backgrounds, which are mostly from QCD interactions, are determined entirely from data.

To account for the sample contamination in the lifetime measurement, we must determine the anticipated d_0 distribution of the total background. Most of the background d_0 distribution width is simply due to the detector resolution. Leptons truly displaced from the interaction point will only be produced by a few sources:

- $W^{\pm}$ and Z^0/γ^* events in which the boson decays to a τ lepton,
- photon conversions in the detector material,
- cosmic ray muons, and
- QCD backgrounds from semi-leptonic decays.

This chapter describes the determination of background event multiplicity. The prediction of the d_0 distribution from each background is explained in Chapter 7.

6.1 Background event multiplicity

For most backgrounds we predict the multiplicity of events by the product of the theoretical cross section (and branching ratio, in the case of exclusive $W^{\pm} \to \ell\nu$ and $Z^0 \to \ell\ell$ production), our sample luminosity, the acceptance of our trigger and topological event selection, and the efficiency to identify the lepton and b jet in such events. For the acceptance and efficiencies we use the Monte Carlo samples described in Table 4.1. We correct the efficiencies for the known shortcomings of the simulation, as described in Chapter 5. The corrections are summarized again in Table 6.1.

Selection	Scale factor: $\epsilon_{\text{data}}/\epsilon_{\text{MC}}$			reference
	Electrons (CEM)	Muons (CMP)	Muons (CMX)	
Lepton ID	0.996±0.005	0.874±0.009	0.989±0.006	[72, 48]
Lepton Isolation		1.00±0.05		[76]
Jet b-tagging		0.909±0.06		[73]

Table 6.1: Scale factors used with Monte Carlo to determine event acceptance.

As noted, the cross section and the acceptance for QCD events are difficult to accurately predict using simulation techniques. Better predictions of these backgrounds are formed by examining the data. The QCD background from photon conversions (N_{conv}) is straightforward to derive from data if the efficiency of the conversion veto is known. The remainder is found after the backgrounds from the simulated samples in Table 4.1 and conversions have been subtracted. The problem then reduces to estimating three *a priori* unknowns: the numbers N_{top}, $N_{\text{electroweak}}$, and $N_{\text{QCD}} - N_{\text{conv}}$. This separation is thoroughly discussed in Section 6.1.5 and Appendix A.

6.1.1 Diboson background

The $p + \bar{p} \to WW$, $p + \bar{p} \to WZ$, and $p + \bar{p} \to ZZ$ background estimates are all derived from their theoretical cross sections. Feynman diagrams for these backgrounds are shown in Figure 6.1. The acceptances modeled by Pythia-generated Monte Carlo samples and the full detector simulation are summarized in Table 6.3. From

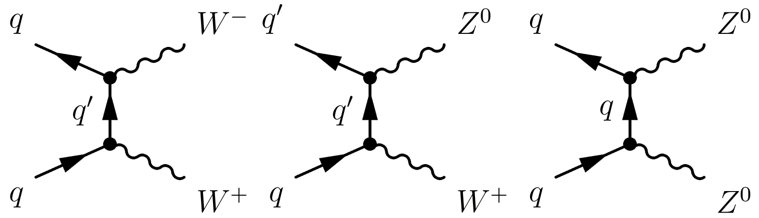

Figure 6.1: Feynman diagrams for the diboson production processes (WW, WZ, ZZ) contributing to the W+jets sample.

these acceptances, the scale factors in Table 6.1, and the trigger efficiencies from Section 3.2.6, there should be 18.2±0.4 electron events and 14.3±0.4 muon (CMU and CMX) events from these three backgrounds in the pre-tag sample. Using the b-tagging acceptance and scale factor we predict a total of 1.31±0.03 electron events and 0.93±0.02 muon events in the signal region. This prediction is compared to other background levels in Table 6.4.

6.1.2 $Z^0 \rightarrow \tau\tau$ background

The theoretical prediction for the inclusive production rate of $Z^0 \rightarrow \tau\tau$ events at the Tevatron is 255 pb^{-1}. The acceptance for this background is also found from Pythia Monte Carlo and the full simulation.

Although τ decays produce leptons less than 26% of the time, and these leptons are typically softer than directly produced e or μ, the reduction in lepton identification efficiency is somewhat compensated by the second τ in the event. A hadronically decaying τ resembles a jet, which increases the acceptance for this background. The event also has a larger tagging tagging probability because of the long-lived hadronic tau decay (the pre-tag $Z^0 \rightarrow \tau\tau$ Monte Carlo events are tagged about four times as frequently as $Z \rightarrow \mu\mu$ events). The corrected pre-tag background estimates for

$Z \to \tau\tau$ are 4.4±0.2 electron and 3.3±0.2 muon events. The expected numbers of tagged events in the $\geq$ 3 jet signal region are 0.29±0.01 electrons and 0.20±0.01 muons, as shown in Table 6.4.

6.1.3 Single top background

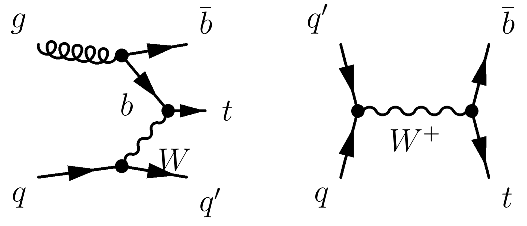

Figure 6.2: Feynman diagrams for single top quark production.

Single top quarks are expected to be produced at the Tevatron by the processes shown in Figure 6.2. The standard model cross sections are small – 1.98 pb for the t-channel exchange and 0.88 pb for the s-channel process. If we use these standard model cross sections, we anticipate 6.6±0.1 electron and 4.4±0.1 muon events due to single top in the pre-tag sample; 3.1±0.1 electrons and 2.3±0.1 muons are tagged.

This small background imposes a measure of model-dependence on this search. As discussed in Chapter 2, most natural mechanisms that generate a long top lifetime would also decrease the single-top cross section.

Since the ratio of the single top cross section in the Standard Model to that cross section in a “natural” scenario with $c\tau_t \simeq 1\mu$m would be $\sim 10^{12}$, a top lifetime of 1μm corresponds to an immeasurably small single top cross section. For any anomalous top lifetime we consider in this measurement, the single top background vanishes. Table 6.2 summarizes the changes to the background calculation caused by assuming

$V_{tq} \simeq 0$.

	electrons		muons	
Process	$N^D_{(+,bg)}$	$N^D_{(+,bg)}, V_{tq} \simeq 0$	$N^D_{(+,bg)}$	$N^D_{(+,bg)}, V_{tq} \simeq 0$
$t\bar{t}$	75.3	78.3	44.9	47.2
W	12.9	13.0	9.1	9.2
Z	0.2	0.2	0.4	0.4
$W \rightarrow \tau\nu$	0.29	0.29	0.20	0.20
QCD	2.0	2.0	1.6	1.6

Table 6.2: The effect of neglecting single top on the background estimates for tagged events in region D, $N^D_{(+,bg)}$.

6.1.4 Conversion electron background

Conversion events are mostly removed by the conversion finding algorithm described in Section 4.1.4. The requirement of three silicon hits also removes a large fraction of conversions, since conversions typically occur outside of the SVX detector outer radius, or in the passive bulkheads. Although conversions form a smaller background in this measurement than in other studies that do not use the $N_{\mathrm{SI\ hit}} \geq 3$ cut, the conversion contamination in $t\bar{t}$ candidate events is explicitly estimated here for the first time. In previous $t\bar{t}$ and $W^{\pm}$ studies at CDF, conversions were treated as a component of the QCD or "non-W" background, since the missing energy in conversion-triggered events is unrelated to the lepton. In the lifetime measurement, however, conversions and other QCD sources are distinct because the d_0 distribution of conversion events reflects the arrangement of dense material in the detector rather than an intrinsic lifetime[1]. Hence we must divide the QCD background for electrons

---

[1] If the photon that converts is from the primary event vertex, the conversion electron's impact parameter can be calculated from the conversion position and the electron's p_T alone.

into a conversion and non-conversion component.

We use $e_{\rm conv}$, the efficiency to find the conversion partner of a tight electron conversion track, to determine the number of conversions *not* removed from the top sample by the conversion veto: $N_{\rm missed} = N_{\rm found}(1-e_{\rm conv})/e_{\rm conv}$. This efficiency $e_{\rm conv}$ is measured in Appendix B, as is the conversion event tag probability. From the 18.4±5 pre-tag conversion candidates, we expect 1.2±0.6 tagged events from the conversion background.

6.1.5 W/Z+jets background

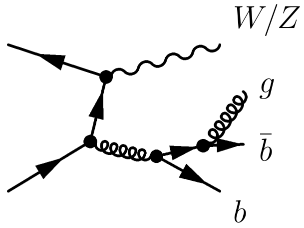

Figure 6.3: Feynman diagrams for the dominant W+jets background.

We use the Monte Carlo simulation to model the kinematics of the W/Z+jets background and measure acceptances, but we constrain the cross section using CDF data with the procedure described in Appendix A. This measurement also produces the number of (non-conversion) QCD events $N_{\rm QCD}$ and thus allows us to estimate the number of top events ($N_{t\bar{t}}$).

Using the event missing energy and lepton isolation variables, we create four disjoint sets of data from the study sample:

- A: $\not\!\!E_T \leq 15$ and Isol > 0.2,

- B: $\not\!\!E_T \leq 15$ and Isol ≤ 0.1,
- C: $\not\!\!E_T > 20$ and Isol > 0.2,
- D: $\not\!\!E_T > 20$ and Isol ≤ 0.1.

These sets are illustrated in Figure 6.4. Note that set "D" corresponds to the signal sample. From each set we subtract the anticipated number N_{bg} of *a priori* backgrounds ($WW, WZ, ZZ, Z \to \tau\tau$, conversions, and single top events) which were calculated in the previous sections. We then solve for the number of electroweak[2] (W, Z and

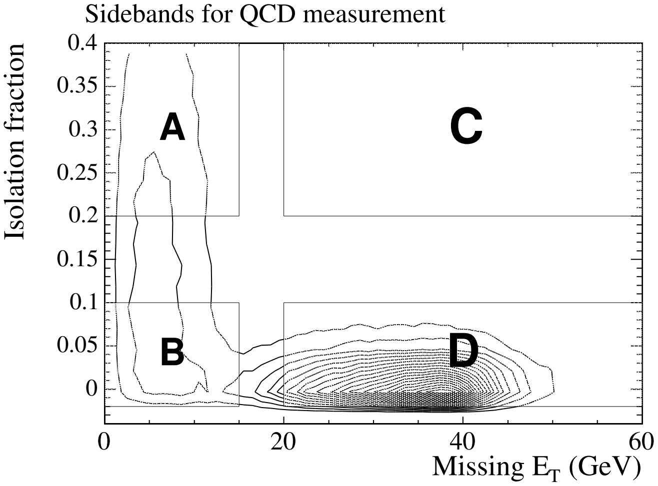

Figure 6.4: Definition of sidebands A,B, and C, used to measure the QCD and $W^{\pm}$+jets backgrounds in the signal region.

---

[2] We cannot treat $Z \to \tau\tau$ like the other electroweak backgrounds here since the Monte Carlo process is modeled at leading order, and the constraints of Equation 6.1 do not hold for the simulated events.

$W \to \tau\nu$), top ($t\bar{t}$) and QCD events in each set by imposing the following constraints:

$$\begin{aligned}
\sigma_W \cdot \mathrm{Br}(W^\pm \to \ell\nu)/\sigma_Z \cdot \mathrm{Br}(Z^0 \to \ell\ell) &= 10.69 \qquad (6.1)\\
\sigma_W \cdot \mathrm{Br}(W^\pm \to \ell\nu)/\sigma_W \cdot \mathrm{Br}(W^\pm \to \tau\nu) &= 1.\\
N_D - \sum_{bg}^{\textit{a priori}\ \mathrm{bkg.}} a_{bg} N_{bg} - \sum_{ewk}^{\ell\nu,\ell\ell,\tau\nu} a_{ewk}\mathcal{L}\sigma_{ewk} - N_{\mathrm{D;qcd}} &= a_{t\bar{t}}\mathcal{L}\sigma_{t\bar{t}} \equiv N_{\mathrm{top}}\\
N^+ - \sum_{bg}^{\textit{a priori bkg.}} a^+_{bg} N_{bg} - \sum_{ewk}^{\ell\nu,\ell\ell,\tau\nu} a^+_{D,ewk}\mathcal{L}\sigma_{ewk} - N^+_{\mathrm{D;qcd}} &= a^+_{t\bar{t}}\mathcal{L}\sigma_{t\bar{t}} \equiv N^+_{\mathrm{top}} \qquad (6.2)\\
\frac{N_{D,\mathrm{qcd}}}{N_{B,\mathrm{qcd}}} &= \frac{N_{C,\mathrm{qcd}}}{N_{A,\mathrm{qcd}}} \qquad (6.3)
\end{aligned}$$

Here a_i is the pre-tag acceptance × efficiency for process i and a_i^+ is the signal sample acceptance × efficiency. $\mathcal{L}$ is the sample luminosity, and σ_{ewk} stands for the cross section × branching ratio for electroweak processes. This decomposition procedure resembles a method used to study the cross sections for continuum $W^\pm$+jets processes, described in [77]. However, we do not fix the $t\bar{t}$ cross section to the theoretical prediction since we are more interested in top events than the W+jets spectrum, and instead add Equation 6.2 as a constraint. The QCD event tagging probability $\frac{N^+_{\mathrm{D;qcd}}}{N_{\mathrm{D;qcd}}}$ and the W+jets tagging probabilities used to calculate $a^+_{W\to\ell\nu}$ are taken from [76]; the latter includes the correction to $\frac{\sigma_{W+b,c}}{\sigma_{W+q}}$ mentioned in Section 4.2.

Solving the system of equations in Equation 6.1, we derive $N_{t\bar{t}}$, N_W, and N_{QCD} for electrons and muons. Details of the method are described in Appendix A. Results are listed in Table 6.4.

Background	$A \times \epsilon$ (e)	$A \times \epsilon$ (μ)	Event tag probability (μ)
$W \to \ell\nu$	1.4%	0.99%	0.054
$Z \to \ell\ell$	0.48%	0.033%	0.015
$W \to \tau\nu$	0.077%	0.054%	0.054
$t\bar{t}$	3.68%	2.77%	0.60
WW	0.37%	0.29%	0.052
WZ	0.21%	0.16%	0.13
ZZ	0.038%	0.036%	0.15
s-channel t	1.2%	0.8%	0.60
t-channel t	0.53%	0.35%	0.44
$Z \to \tau\tau$	0.040%	0.029%	0.06

Table 6.3: Acceptance-efficiency product and tagging probabilities for Monte Carlo background samples. The efficiency includes the trigger efficiencies, and lepton identification, SVX tracking, and z_0 vertex scale factors.

6.1.6 Cosmic ray muon background

We confirm that the cosmic ray veto reduces this background to negligible levels. Since cosmic rays are uncorrelated with the beam position, the d_0 distribution of these tracks should be flat[3], and we can estimate an upper limit on the cosmic ray contamination by looking at the tails of d_0 for muons in the signal sample. We compare the number of selected muon pre-tag events for events passing the cosmic veto to those failing it, when the muon passes the silicon hit selection but has $|d_0| >0.1$ cm. This sample should be composed of cosmic ray muons, with some contribution from QCD heavy flavor muons. We neglect the effect of QCD here since we are interested in a rough upper limit on the cosmic ray contamination.

Interpreting all of the muons with large d_0 as cosmic rays, the veto is more than 0.983 ±.001 efficient. As demonstrated in Figure 6.5, only one flagged cosmic candidate is found with $N_{\text{jet}} > 2$. Hence, assuming the cosmic ray veto efficiency is

---

[3] In fact the silicon hit requirement sculpts the d_0 distribution for $d > 1.1$cm.

Process	Tagged	Pre-tag
	electrons	
$W \to \ell\nu$	240.8±18.6	12.9±1.0
$Z \to \ell\ell$	7.8±0.6	0.2±0.01
$W/Z \to \tau$	17.8±1.6	1.01±0.1
$t\bar{t}$	120.5±15.4	75.3±9.6
$WW + WZ + ZZ$	18.2±0.4	1.31±0.03
single t	6.6±0.1	3.1±0.1
QCD	19.8±3.4	2.0±0.4
Conversions	18.4±5.0	1.2±0.6
	muons	
$W \to \ell\nu$	170.8±13.3	9.1±0.8
$Z \to \ell\ell$	27.2±2.5	0.4±0.04
$W/Z \to \tau$	12.5±1.2	0.69±0.07
$t\bar{t}$	75.4±13.0	44.9±7.8
$WW + WZ + ZZ$	14.3±0.4	0.93±0.02
single t	4.4±0.1	2.3±0.1
QCD	15.4±2.6	1.6±0.3

Table 6.4: Signal and background event multiplicities for the signal cuts used in this analysis (when standard model estimates of the single top cross sections are used). Data/MC statistical errors are included.

uncorrelated with N_{jet}, no more than .0173 ±.0173 cosmic events are expected in the pre-tag signal region. Even without resort to the additional suppression of the d_0 cut, which should remove nearly 90% of the remaining cosmic muons, this background can be safely ignored.

6.1.7 Summary

We have calculated the purity of the tagged event samples for electrons and muons by producing the background estimates in Table 6.4, and thereby established that

$$Prob(d_0; c\tau) = (0.78)Prob^{t}(d_0; c\tau, \sigma_{d_0}) + (0.22)Prob^{!t}(d_0; \sigma_{d_0}) \tag{6.4}$$

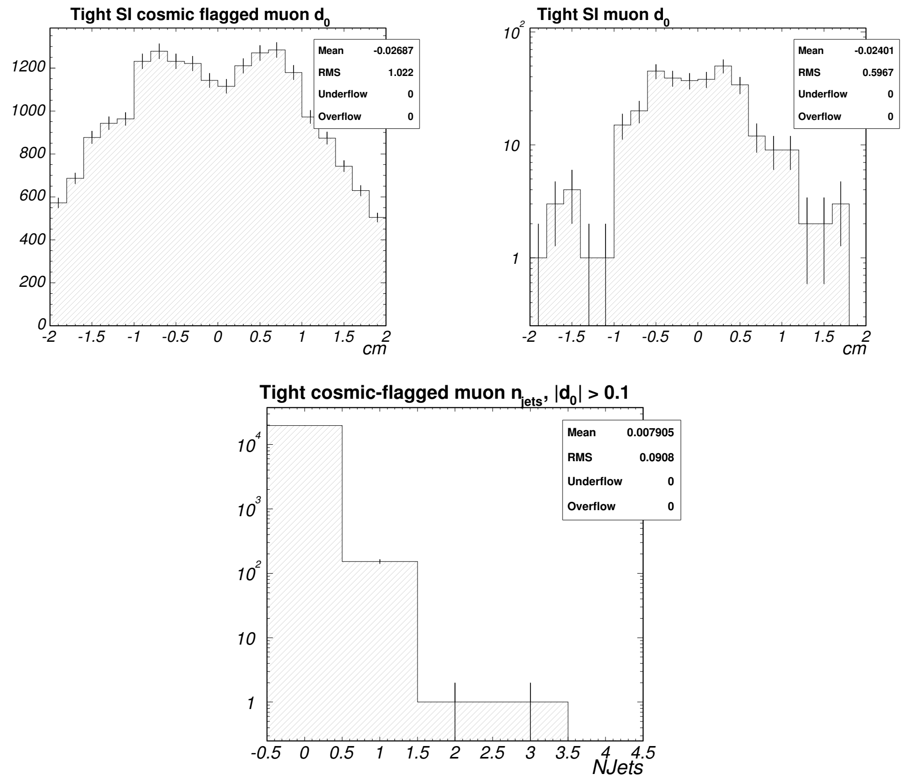

Figure 6.5: Top: Comparison of the impact parameters of tight muon tracks with more than 2 silicon r-ϕ hits in the pre-tag sample, for events failing (left) or passing (right) the cosmic veto. For the events passing the veto, the region $|d_0| < 0.1$ has been removed from this plot for illustrative purposes. Bottom: the N_{jets} spectrum of failed cosmic events.

if d_0 is measured with an electron track, and

$$Prob(d; c\tau) = (0.75)Prob^{t}(d; c\tau, \sigma_{d_0}) + (0.25)Prob^{!t}(d; \sigma_{d_0}) \tag{6.5}$$

if d_0 is measured with a muon track. Moreover, our background composition indicates that 0.773 of the total background electrons and 0.822 of the total muon background should have impact parameters consistent with zero, given the detector resolution. The probability distributions for other background leptons' impact parameters are discussed in the next chapter.

6.2 Systematic uncertainties in background composition

Uncertainties in the background measurements directly affect the calculated signal fraction $\mathsf{p}_{t\bar{t}}$, and uncorrelated uncertainties among the background calculations also affect the background template $Prob^{!t}(d_0; \sigma_{d_0})$. In this section we describe the sources of systematic errors. Monte Carlo and data sample statistical errors, calculated at each stage of the acceptance and efficiency measurements, have already been noted in the preceding tables and text.

The total error on the background estimate is given in Table 6.5. The effect of these background errors on our lifetime limit is discussed in Chapter 8.

6.2.1 QCD background estimates

The QCD background for electrons is measured in two components: the conversion background, and the remainder. From the systematic error on the conversion inefficiency determined in Appendix B, the conversion background uncertainty is 16%.

For e and μ events the separation of the remaining QCD processes from t and $W^{\pm}$ production depends on the missing energy and isolation modeling by the simulation. We vary the boundaries of the sideband regions A,B, and C and repeat the procedure, to probe possible shortcomings in the Monte Carlo. We move the isolation cut by ± 0.1 and the missing energy threshold by ± 5 GeV, and calculate the change in N_{top}, N_{ewk} and N_{QCD}.

We let the largest deviation represent our uncertainty, and find a 25% systematic uncertainty on the QCD background based on this procedure.

6.2.2 Heavy flavor tagging

The 6.6% systematic error on the b-tagging scale factor affects the *a priori* backgrounds coherently. Hence we calculate the error on the tagged backgrounds and apply it as a correlated systematic in Chapter 8. The effect on the total background is listed in Table 6.5. This scale factor error also affects the predicted number of tagged top and W events in the QCD background separation procedure; to determine the effect of the uncertainty on this part of the background measurement, we vary $(SF)_{\mathrm{tag}}$ within its errors and note the fluctuations in the sample decomposition. Finally, an additional 26% error on N_W is contributed by the measurement of the heavy flavor content of the W sample [67].

6.2.3 Luminosity, trigger efficiency and scale factor uncertainties

Monte Carlo samples for which we use a cross section and the simulated acceptance are sensitive to errors in event trigger efficiencies, lepton identification and silicon hit attachment scale factors. These were determined previously [78, 47, 72, 48, 71], and are tabulated in Table 6.6. Combined errors for these sources are taken as correlated when incorporated into the limit calculation.

Systematic	Electron	Muon
EWK/QCD estimate (stat)	1.1	0.85
MC statistics	0.07	0.05
Cross sections	0.13	0.07
$\mathcal{L}$/Trig/Lep ID/N_{Si}	0.39	0.25
b-tagging	0.33	0.21
W tag rate	3.59	2.66
QCD method	0.56	0.43

Table 6.5: Error (in N_{events}) on the total background estimate.

Error source	relative uncertainty (%)		
	CES	CEM	CMUP
Luminosity		5.9	
Trigger efficiency	0.62	0.55	0.41
Lepton ID scale factor	0.50	1.03	0.61
z_0 vertex		0.32	
Lepton ID		5	

Table 6.6: Correlated errors for backgrounds estimated from Monte Carlo [47, 72, 48, 71, 78]

Chapter 7

Templates

In this chapter we describe the creation of $Prob^{t}(d; c\tau, \sigma_d)$ and $Prob^{!t}(d; \sigma_d)$, the signal and background *templates*. We first discuss the impact parameter resolution for high p_T electron and muon tracks with silicon hits, and determine a *resolution function* describing the probability distribution of the difference between the true and observed impact parameters ($d_0^{\mathrm{obs}} - d_0^{\mathrm{true}}$). We call this function $g(d_0^{\mathrm{obs}} - d_0^{\mathrm{true}})$. In Section 7.2 we use Standard Model t production and decay kinematics from simulated $t\bar{t}$ events to construct the distribution of d_0^{true} in events where the t quark has an arbitrary lifetime. In this toy model, top production kinematics are not affected by the new physics responsible for the long lifetime. We then use the resolution function g to derive the observable d_0 distribution from these templates. Finally, in Section 7.3 we describe the creation of background templates, using the background measurements in Chapter 6.

7.1 Track impact parameter resolution

If for a given lepton the detector resolution causes track d_0 mismeasurement by Δd_0, and the beam position is displaced from the average beamline by $\vec{b}$ in the transverse plane, the measured track impact parameter will be related to the true impact parameter by[1]

$$d_0^{\text{obs}} \simeq d_0^{\text{true}} + \Delta d_0 - (\vec{b} \times \hat{p}_T)_z = d_0^{\text{true}} + \Delta d_0 + \Delta b_0, \tag{7.1}$$

The beam displacement Δb_0 is related to the Tevatron transverse emittances, and makes a the largest contribution to the resolution of d_0^{obs}, as discussed in Section 3.1.3. The probability distribution for $\Delta d_0 + \Delta b_0$, which we call the resolution function $g(d_0^{\text{obs}} - d_0^{\text{true}})$, can be directly measured in a sample where $d_0^{\text{true}} = 0$. Since Δd_0 is independent of d_0^{true} for small displacements of high p_T tracks, this resolution function will apply even to tracks with a different d_0^{true} distribution, such as tracks from hypothetical long-lived t decays.

To use this measurement in our lifetime limit we must additionally ensure that the tracks in the $d_0^{\text{true}} = 0$ sample are very similar to the tracks in our signal sample. Below we describe how these samples are constructed, and report the measured probability distribution $g(d_0^{\text{obs}} - d_0^{\text{true}})$.

7.1.1 Prompt lepton track samples

We use the Z^0 sample first introduced in Chapter 5: Z^0 bosons decaying to central leptons (electrons or muons) are selected from the `ELECTRON_CENTRAL_18` and

---

[1] We have written a linear approximation in curvature κ for the beam displacement error.

`CEM/CMX_18` datasets. We choose events from the same runs as the signal sample, and again require that the event z vertex be fiducial and that any muons are inconsistent with a cosmic ray. Lepton identification cuts are listed in Tables 5.1 and 5.2.

From these data we create a very pure sample of Z^0 events by requiring that two oppositely charged leptons of the same type pass the cuts in Table 5.1 or 5.2. The candidate pairs are required to have an invariant mass very near the Z^0 resonance ($83 < m_{\ell^+\ell^-} < 106$ GeV/c^2) to increase the purity of the sample: the lower mass limit was raised to reduce background contamination. 2725 muon events and 4288 electron events pass the complete Z^0 selection and are used in the resolution functions.

7.1.2 Z^0 sample purity

Electrons

The purity of a lepton sample like the one specified above is of common interest to CDF experimenters, and it has been measured for an electron sample (using a Z^0 mass window of $76 < m_Z < 106$ GeV/c^2 and removing the $N_{\text{SI hit}} \geq 3$ cut) to be 99.85 ± 0.05 % [72]. The method relies on the number of same-sign events as a background estimate. However, Z^0 events in which one leg forms a trident are also a source of same-sign events which we term the "trident background." In the study cited above, the trident background is considered signal and so the background estimate is corrected by the number of wrong-sign events in Z^0 Monte Carlo samples. For our purposes, the trident background is contamination, since the d_0 of the conversion legs does not represent the resolution of the d_0 of the prompt lepton. After applying the $N_{\text{SI hit}} \geq 3$ cut to both legs, which efficiently reduces the trident contamination, our

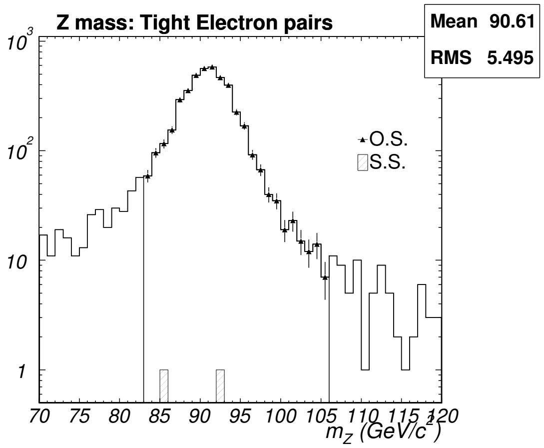

Figure 7.1: The Z^0 invariant mass distribution for same-sign (shaded) and opposite-sign electron pairs. The same-sign events demonstrate the background contamination. The vertical lines indicate the region used for the resolution function.

measured background fraction becomes .10 ±.06%. In the tighter Z^0 mass window that we require for the resolution function measurement ($83 < m_Z < 106$ GeV/c^2) the background estimate is consistent: 0.07 ±0.05 %.

Muons

The muon sample, again with $76 < m_Z < 106$ GeV/c^2 and no silicon hit cuts, is evidently 100% pure[48]. We confirm this high purity in our more restrictive sample: no same-sign (s.s.) events populate the signal region so our background estimate is 0. To set an upper limit on the background, we use the 90% C.L. upper limit on $N^{s.s.}$ from sampling a Poisson distribution when $N^{s.s.}_{\rm obs} = 0$. This limit, $N^{s.s.} < 2.44$, implies a background fraction less than 0.13%.

The background in this sample should be dominated by $W^{\pm} \rightarrow \mu\nu$ events combined with a random track. Since $W^{\pm}$ leptons are also prompt, we can safely neglect any non-prompt component in the resulting sample.

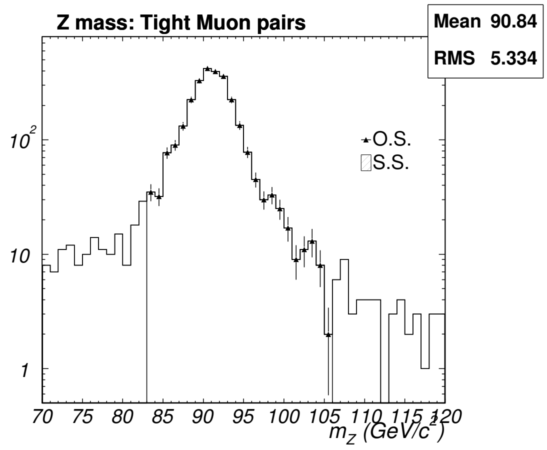

Figure 7.2: The Z^0 invariant mass distribution for muon events demonstrates the mass range used in constructing the resolution function. There are no same-sign events in the mass window.

7.1.3 Resolution functions

Using this $100.0^{+0}_{-0.13}\%$ pure sample of $Z^0 \to \mu^+\mu^-$ events and the 99.93 $\pm 0.05\%$ pure sample of $Z^0 \to e^+e^-$ events, we can plot $Prob(d_0)$ for leptons of each type, which is equivalent to $g(d_0^{\rm obs} - d_0^{\rm true})$ since $d_0^{\rm true} = 0$. We thus determine the impact parameter resolution functions for high p_T leptons, including the beam width uncertainty. The r.m.s. of $g(d_0^{\rm obs} - d_0^{\rm true})$ is 37.9$\pm$0.3 (stat) μm for electrons and 32.6$\pm$0.3 (stat) μm for muons. The resolution functions for muons and electrons are depicted in Figure 7.3.

7.2 Signal sample d_0 probability distributions

To simulate long lived t decay kinematics, we simply use standard model top kinematics and move the t decay vertex appropriately along the top $\vec{p}$ direction. The standard model t kinematics come from our PYTHIA simulation of 178 GeV/c^2 $t\bar{t}$ pair production and decay, the `ttopel` sample. The sample is reconstructed and filtered with the cuts in Chapter 5 so that the probability density for the requisite kinematic variables reflects the probability density functions in our sample, which are in principle biased by our cuts. When the $W^{\pm}$ decays to e or μ, the true impact parameter of a track from a long-lived t decay depends on the lifetime and velocity of the t in the laboratory frame, the projection of the t path onto the $(r-\phi)$ plane, and the angle between the t flight direction and the lepton's direction. The relationship is shown in Figure 7.4. At higher order, the impact parameter also depends on the lepton track curvature (or transverse momentum). Thus, three numbers are needed to specify the lepton d_0 for a such a t decay event:

- $ct\beta\gamma \sin\theta$, the t quark flight distance in the $(r-\phi)$ plane,
- $\alpha_{\ell t}^{\mathsf{lab}}$, the decay angle of the lepton with respect to the t direction, and
- the lepton track p_T.

These values are correlated in t decays, so their three-dimensional joint distribution is used to generate signal templates. Two-dimensional projections of the joint distribution $Prob(ct\beta\gamma\sin\theta, \alpha_{\ell t}^{\mathsf{lab}}, p_T^{\ell})$ are shown in Figure 7.5. From Figure 7.4 we can determine the true track d_0, using the helix diameter D and center (x_c, y_c). The d_0

of a track of charge q satisfies

$$qd_0 = \sqrt{(x_c - x_0)^2 + (y_c - y_0)^2} - D/2. \tag{7.2}$$

Applying the top lifetime displacement is equivalent to setting

$$\begin{aligned} D_\ell &= 2\frac{p_T}{c \times (1.4\text{ T})} && (7.3) \\ x_c &= c\tau\beta\gamma\sin\theta + \frac{D_\ell}{2}\cos(\alpha_{\ell t}^{\mathsf{lab}} + q_\ell\frac{\pi}{2}) && (7.4) \\ y_c &= \frac{D_\ell}{2}\sin(\alpha_{\ell t}^{\mathsf{lab}} + q_\ell\frac{\pi}{2}) \end{aligned}$$

(where for simplicity we have chosen a reference frame aligned with the t flight direction.)

Tau decays in signal events While we constructed analysis cuts in Chapter 5 in order to accept $W^\pm \to e\nu_e$ and $W^\pm \to \mu\nu_\mu$ decays in $t\bar{t}$ events, the tight lepton originates from a $W^\pm \to \tau\nu$ decay in 8.8% of selected $t\bar{t} \to W^\pm$+jets events. Since the τ is also long-lived, additional information is needed to construct the track d_0 from $\tau \to \ell\bar{\nu}_\ell\nu_\tau$ in this case: for these events we also record the laboratory-frame $\delta\phi$ between the e or μ and the τ direction, and the τ lepton's flight distance in the transverse plane. We then simply add the tau's displacement to (x_c, y_c).

Using the calculations above, we convert the kinematic information in Figure 7.5 into a probability distribution function for d_0^{true}. These are our unsmeared signal templates. Examples of the resulting templates are shown in Figure 7.6.

7.2.1 Signal templates

We can now derive and parameterize a set of signal templates. The probability density functions for d_0^{obs} of leptons from $t \to W^{\pm}b$ decays are obtained by convolving the distributions obtained in Section 7.2 with the resolution function. Examples of the final templates $Prob^t(d; c\tau, \sigma_d)$ are shown in Figure 7.7.

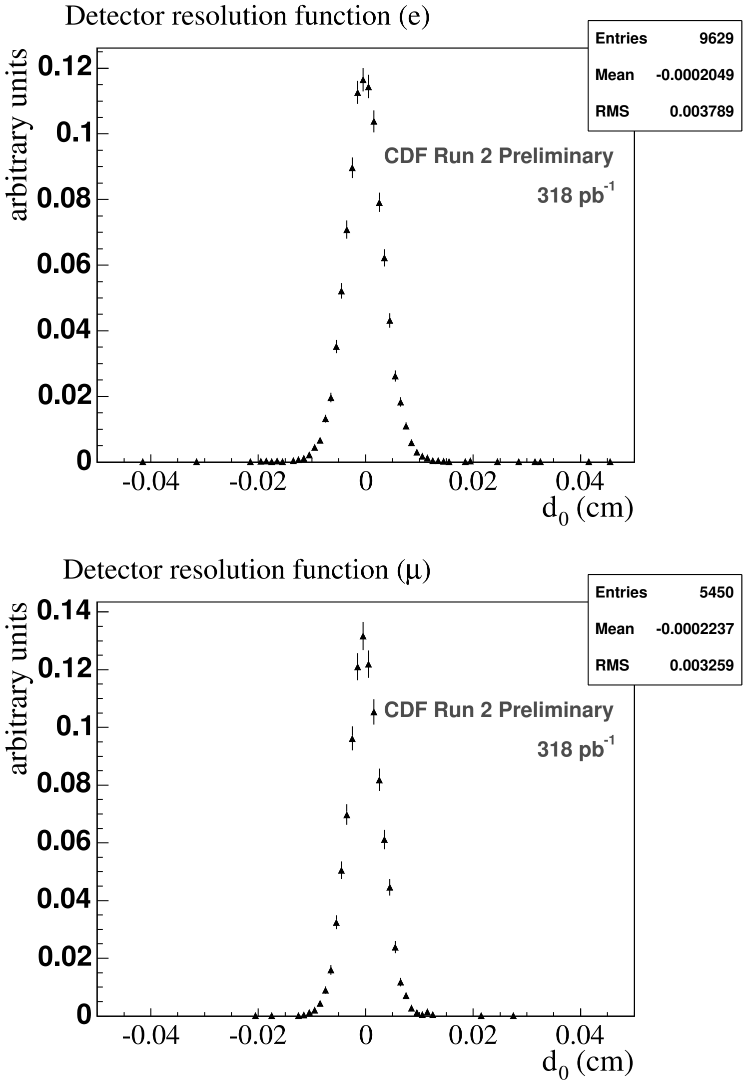

Figure 7.3: Track impact parameter distributions for $Z^0 \to e^+e^-$ and $Z^0 \to \mu^+\mu^-$ events. These are the resolution functions $g_e(d_0^{\rm obs} - d_0^{\rm true})$ and $g_\mu(d_0^{\rm obs} - d_0^{\rm true})$.

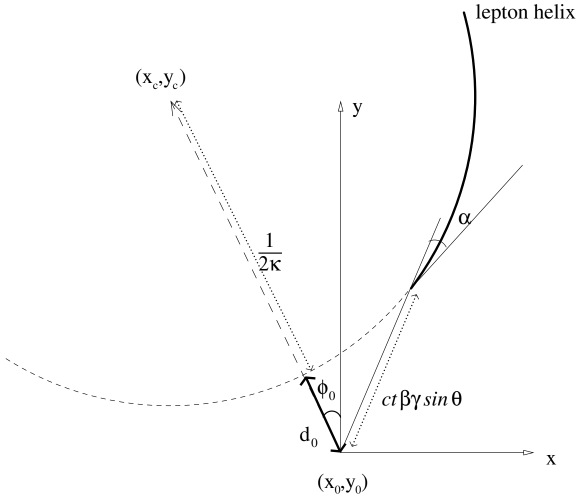

Figure 7.4: Illustration of the impact parameter calculation based on the *t* flight distance, the lepton direction, and the lepton track curvature.

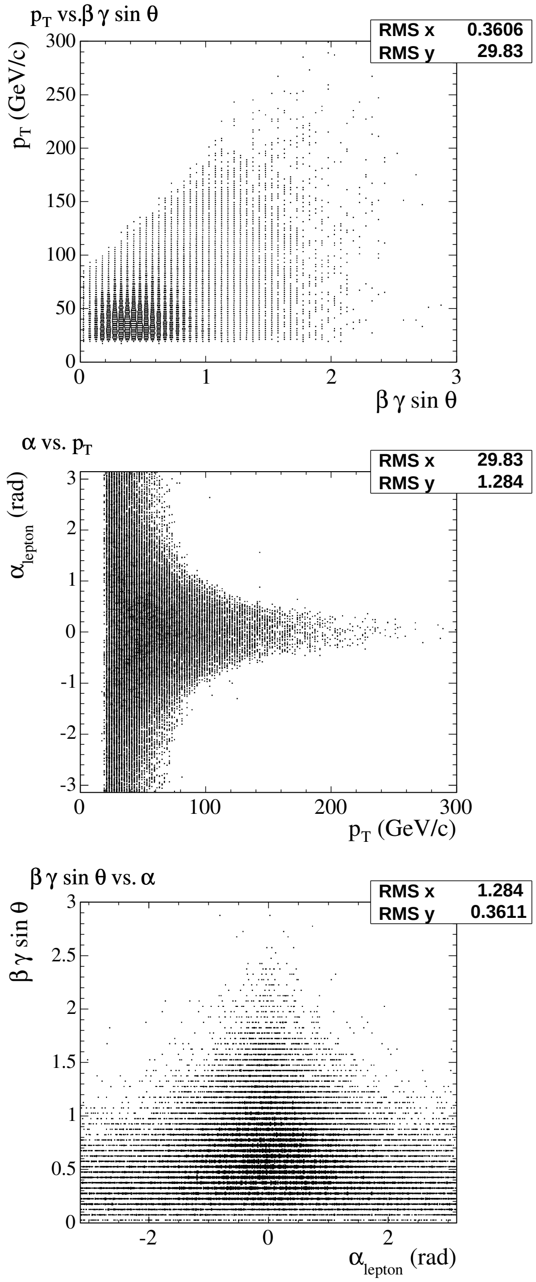

Figure 7.5: Correlations between the kinematic variables in t decay which are used to construct the signal templates. Top: lepton p_T *vs.* top flight distance ($ct\beta\gamma\sin\theta$). Middle: lepton p_T *vs.* lepton angle $\alpha_{\ell t}^{\mathsf{lab}}$. Bottom: Top flight distance *vs.* lepton angle.

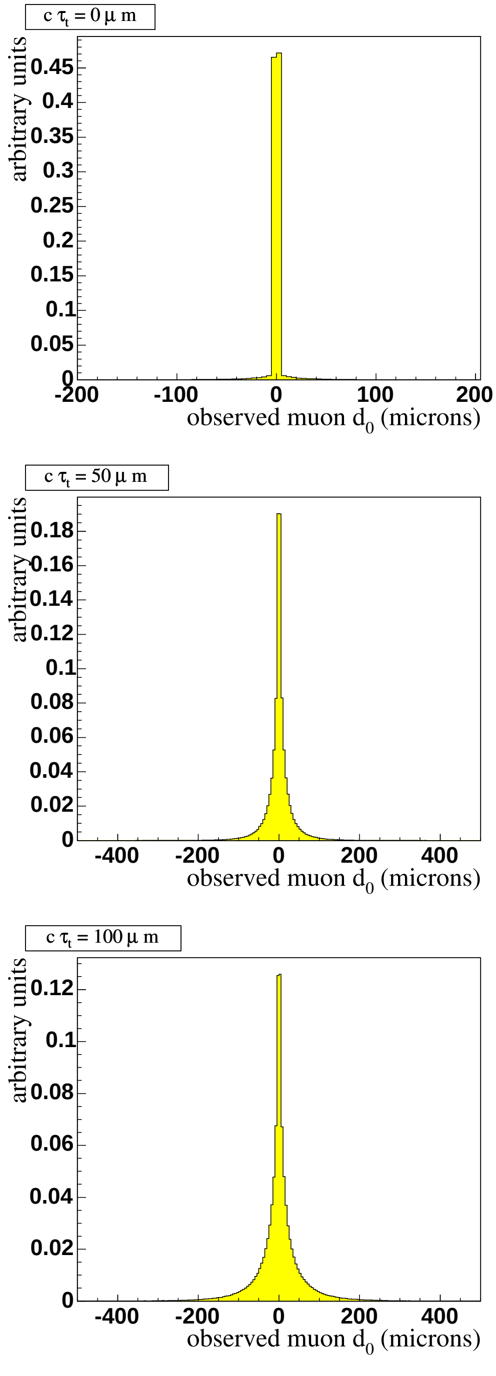

Figure 7.6: Example probability densities for d_0^{true} (signal templates), including $t\bar{t}$ events with τ leptons. These templates will be smeared by the resolution function $g(d_0^{\text{true}} - d_0^{\text{obs}})$ and compared with the data.

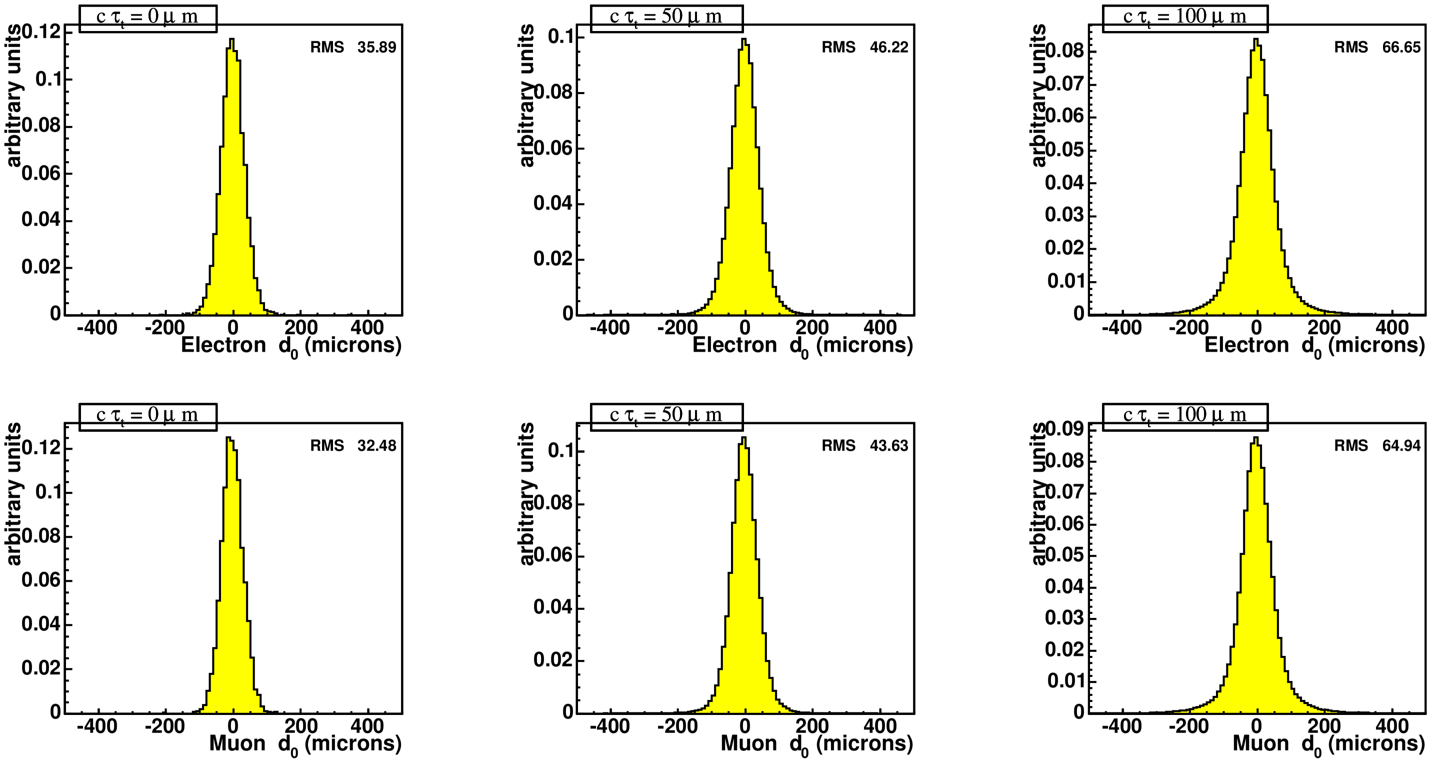

Figure 7.7: Example probability densities for $d_0^{\text{obs.}}$ for electrons (top) and muons (bottom), after smearing with the resolution functions.

7.3 Background d_0 distribution functions

7.3.1 Prompt backgrounds

Most backgrounds are "prompt:" they produce leptons at the interaction point. These backgrounds come from the dominant $W^\pm \to \ell\nu$ process, as well as $Z^0 \to \ell\ell$, WW, WZ, ZZ, and, whenever relevant, single top. For these processes, the probability distribution of the observed impact parameter is represented by the resolution function g, derived in Section 7.1 and depicted in Figure 7.3.

7.3.2 $Z^0 \to \tau\tau$ and $W^\pm \to \tau\nu$ backgrounds

Because the τ is long-lived, we must model the d_0 distributions for τ-producing backgrounds[2]. Again, we smear the distribution of d_0^{true} obtained from taus in our Monte Carlo by $g(d_0^{\text{true}} - d_0^{\text{obs}})$. We can safely increase the statistical power of our simulated samples by releasing cuts that have no effect on the d_0 shape, but it turns out that different cuts affect the d_0 of leptons in $Z^0 \to \tau\tau$ and $W^\pm \to \tau\nu$.

The $W^\pm \to \tau\nu$ background is represented by all tight, isolated leptons in events from the $W^\pm \to \tau\nu$ sample passing the pre-tag event selection. However, the pre-tag sample is a poor model for the Z^0 background, because the probability to mistag a hadronic tau jet in a $Z^0 \to \tau\tau$ event is related to its momentum. Correlations in the p_T of the two Z^0 legs are reflected in the flight distance of the leptonically decaying τ. For $Z^0 \to \tau\tau$ events we cannot release the tag cut, but we can loosen the N_{jet} cut to ≥ 1.

---

[2] The backgrounds in this section do not include the potential $W^\pm \to \tau\nu$ decays in $t\bar{t}$ events, which are treated as part of the *signal* template.

The smeared $W^{\pm}$ and Z^0 contributions are normalized to the ratio of signal predictions, and the combination is fit as shown in Figure 7.8.

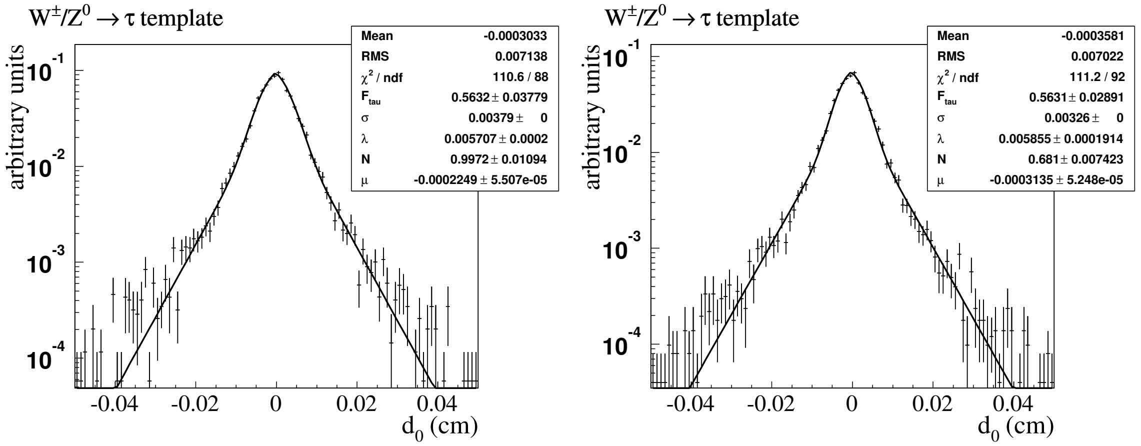

Figure 7.8: Template shapes for the $W^{\pm}/Z^0 \to \tau$ background in the signal region. Electrons are on the right, and muons are on the left. We fit the data to the sum of a Gaussian distribution and a symmetric exponential with decay constant λ; the non-Gaussian fraction is F_{tau}.

7.3.3 Conversion electron background

For photons that point back at the primary vertex and convert at a radius r_{conv} in the detector, the created electrons' d_0 is simply expressed by κr_{conv}^2 at leading order in the track curvature κ. This only depends on r_{conv} and the electron p_T, so we can use a large conversion sample to study the template distribution. We relax the following cuts with respect to the signal sample:

- N(jets) ≥ 0 (was ≥ 3)
- N(tags) ≥ 0 (was ≥ 1)
- Isol < 1.0 (was < 0.1)

- $\not\!\!E_T \geq 0$ (was ≥ 20)

This conversion sample will obviously have the correct probability distribution in r_{conv}, but κ is biased by our change of cuts. Figure 7.9 compares the $1/p_T(\propto \kappa)$ distributions of these conversion candidate electrons to conversion electrons in events in the signal sample. Since they are different, we use the ratio of these distributions to re-weight the conversion events based on their p_T. In Figure 7.10 we show the resulting template shape.

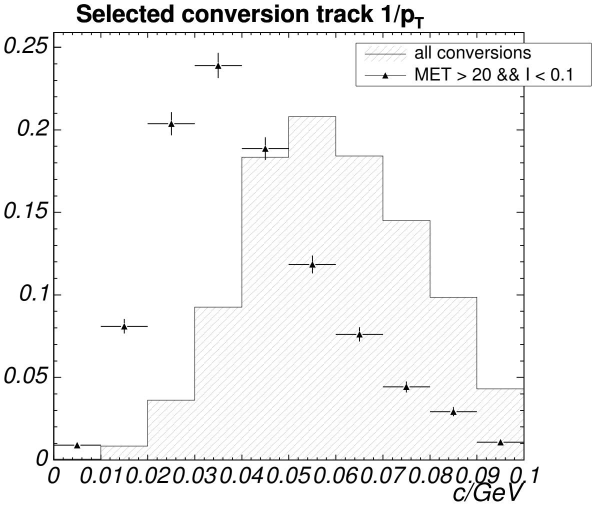

Figure 7.9: Comparison of $1/p_T$ for conversions used to generate the template and conversions in events passing signal cuts ($\not\!\!E_T > 20, I < 0.1$). To generate a corrected template, the conversion events are re-weighted by the ratio of these distributions.

7.3.4 QCD jet background

QCD backgrounds include prompt fakes, modeled by the prompt template, and heavy flavor leptons. For the heavy flavor template, we fit events with $\not\!\!E_T < 15$ in the

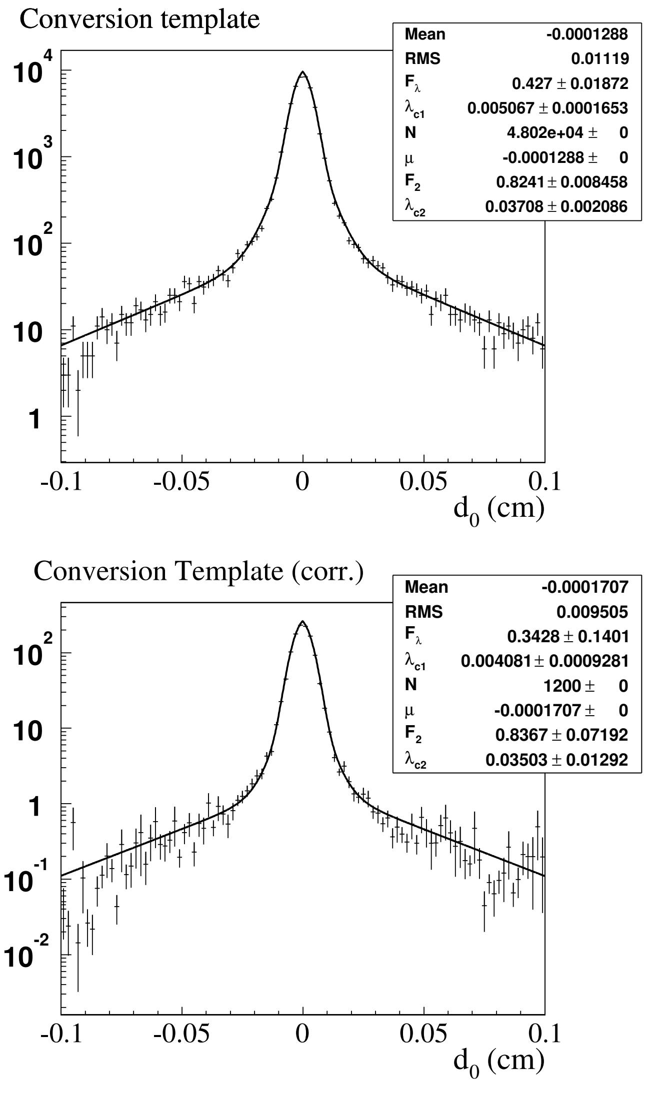

Figure 7.10: Template shape for conversions before and after correcting the p_T bias. We must use two symmetric exponential distributions with fractions F_λ and $F_\lambda F_2$, and decay parameters λ_1 and λ_2. These are added to a Gaussian distribution to describe the conversion data. The conversions are found in the looser sample described in Section 7.3.3. Top: before re-weighting. Bottom: after re-weighting.

1- and 2-jet bins. We use Monte Carlo to determine a parameterization and study correlations.

We begin with a sample of generic QCD 2 → 2 scattering events produced by HERWIG and filtered for a 9 GeV lepton. Because the lepton filter precedes the detector simulation which produces conversion electrons and muons from meson decay in flight, it essentially selects leptons from b and c jets. Pre-tag events in this sample are 77±6% heavy flavor; most of the light flavor leptons are electrons from neutral meson decays. We will assume that the b and c lifetimes are well represented by the Monte Carlo, but use events in data to determine the normalization parameters of the fit function. The impact parameter distributions for leptons from b and c decays are well-described by two exponential decay components, one with $\lambda_{\text{long}} = 121 \pm 20$ μm, and the other with $\lambda_{\text{short}} = 45 \pm 5$ μm.

We process these samples with the detector simulation and the standard event selection from Chapter 5, and show the resulting d_0 distribution in Figure 7.11.

Simulating enough generic QCD events to model the heavy flavor lepton backgrounds with high statistical accuracy has been a continuing challenge at CDF. We must explore our signal cuts to improve the statistics of the Monte Carlo template shape without imposing systematic biases. The $\not\!\!E_T$, SECVTX and jet multiplicity cuts only affect the b/c ratio and not the shapes of lepton d_0 distributions from b or c decays, so we relax these cuts and check that the parameterization is still valid.

Next we determine the free parameters the data, first using isolated events in the 1 and 2 jet bins with $\not\!\!E_T < 15$. In the pre-tag sample, this region is about 95% QCD; τ events contribute less than 1% to either jet bin, but conversions are a significant

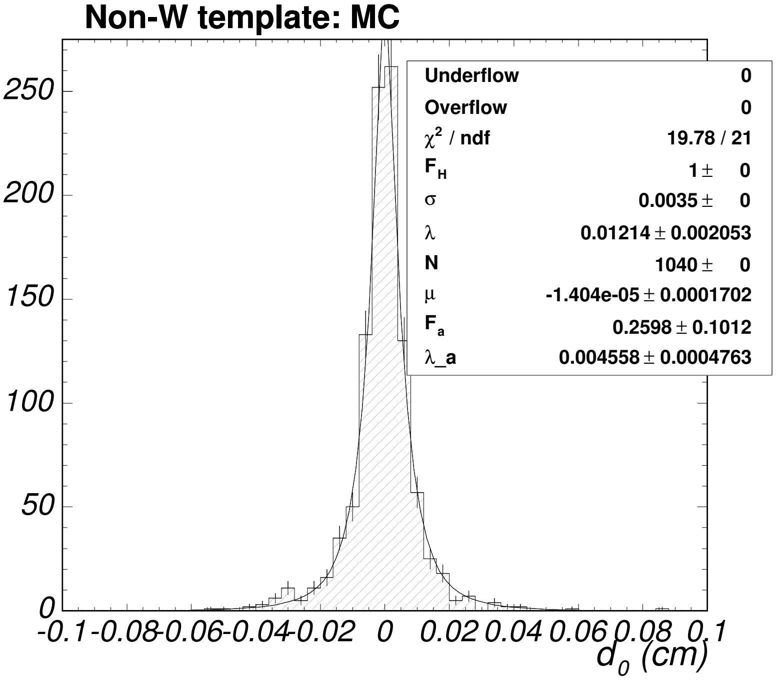

Figure 7.11: Heavy flavor template parameterization from QCD 2 → 2 Monte Carlo. The parameterization is the same as for conversion electrons, but the Gaussian contribution is zero in this pure Monte Carlo sample. All leptons passing p_T cuts are used to determine the form of the QCD impact parameter template parameterization.

contribution to the electron sample. We allow the normalizations of both lifetime components and a prompt Gaussian to float in the fit.

The 1.1K selected muon events are predicted by the template shape with a χ^2 probability of 86%, while the fit to 3.4K electron events has a $\sim 10^{-5}$ χ^2 probability. However, we have not corrected for conversion electrons. We account for these by including the conversion template shape described in Section 7.3.3, normalized to the number of conversions expected in the 1 and 2 jet bins at low $\not\!\!E_T$. The resulting fit is acceptable: Prob(χ^2) = 11%.

To finally fix the free parameters, we require a tagged jet and repeat the fit. The result is shown in Figure 7.12. The events used to model the heavy flavor template, which have low $\not\!\!E_T$, might have a different heavy flavor composition than the QCD background in the signal region. In the QCD Monte Carlo, the fraction of leptons from b jets increases slightly (0.24 ± 0.21% per GeV) with missing energy, after a tagged jet is found in the event (Figure 7.13). We use this slope to correct the parameterization derived in the low $\not\!\!E_T$ sideband. The difference in mean $\not\!\!E_T$ between the signal region and our low $\not\!\!E_T$ sideband is 27.5 GeV, so we estimate that the fraction of leptons from b decays should be 6±5% higher in the signal region.

7.3.5 Background templates

By decomposing the backgrounds in the tagged $W^{\pm}$+jets dataset into components with similar lepton d_0 distributions, we have constructed a template shape which should describe the d_0 distribution of the non-$t\bar{t}$ events in our $t\bar{t}$ candidate sample, events that make up approximately 25% of the data. Most of these backgrounds

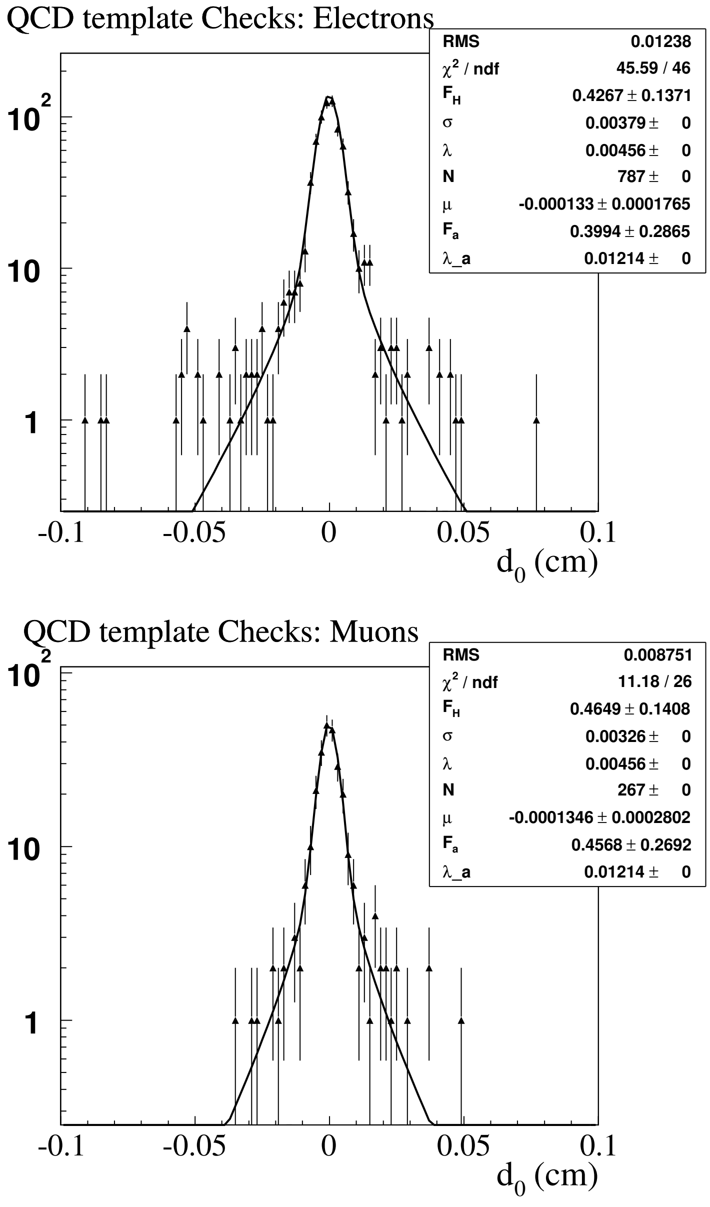

Figure 7.12: Validation of the heavy flavor templates in ≤ 2 jet, low missing energy tagged events.

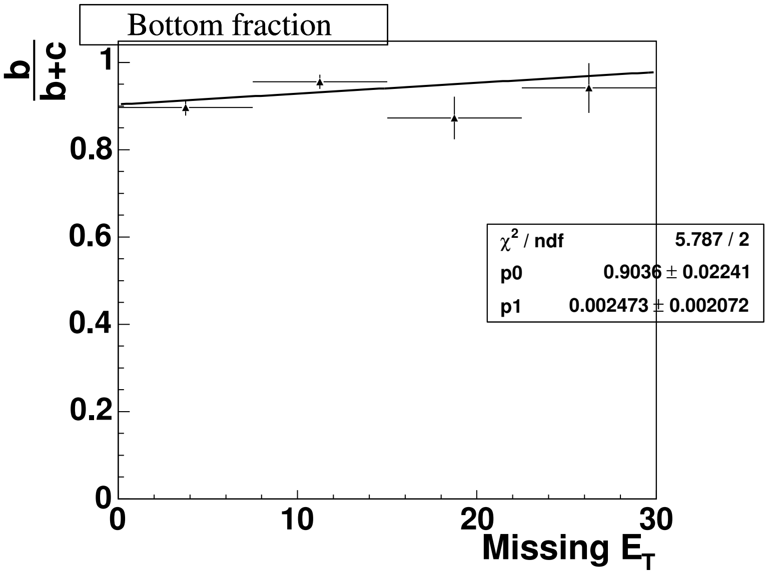

Figure 7.13: There is some correlation between $\not\!\!E_T$ and the lepton parent in QCD Monte Carlo. The plot shows the fraction of leptons produced in b decays with respect to the total number of leptons produced in heavy flavor decays, as a function of event $\not\!\!E_T$. We assume this effect is present in the data and correct our parameterization accordingly.

produce prompt leptons, which have d_0 distributions with r.m.s. 32.6μm for muons (37.9μm for electrons). The remaining contribution is summarized in Table 7.1.

Background (e)	pre-tag sample	tagged sample	d_0 template r.m.s.
$t\bar{t}$	120.5±15.4	75.3±9.6	—
Prompt	266.7±19.3	14.4±1.0	37.9±0.4
Single Top	6.6±0.1	3.1±0.1	37.9±0.4
Tau	17.8±1.6	1.01±0.1	71 ±0.6
QCD	19.8±3.4	2.0±0.4	108 ±3
Conversions	18.4±5.0	1.2±0.6	95 ±1

Background (μ)	pre-tag sample	tagged sample	d_0 template r.m.s.
$t\bar{t}$	75.4±13.0	44.9±7.8	—
Prompt	212.3±13.6	10.5±0.8	32.6±0.3
Single Top	4.4±0.1	2.3±0.1	32.6±0.3
Tau	12.5±1.2	0.69±0.07	70 ±0.6
QCD	15.4±2.6	1.6±0.3	95 ±4

Table 7.1: Summary of electron (top) and muon (bottom) background templates. Statistical errors from data and Monte Carlo are included.

Background	Normalization error		Shape error	
	electron	muon	electron	muon
Prompt	27%	27%	0.6μm	0.6μm
Tau	10%	10%		
Conversions	6%	6%	2%(λ)	–
QCD	30%	30%	8.6%(F_H)	8.6%(F_H)

Table 7.2: Summary of systematic errors applicable to the template normalizations and shapes. The error on the conversion shape is to account for potential biases in conversion finding, based on the conversion r_{conv} or lepton p_T. The error on the QCD shape is to account for the extrapolation to high $\not{E}_T$. Both are described in the text.

7.4 Systematic distortions of templates

7.4.1 Signal templates

Our signal kinematic model determines the resulting template shapes. An exotic, long-lived top-like quark would probably not have the same production and decay distributions as the standard model top, but even our simulations of these standard model distributions suffer systematic uncertainties.

Signal template errors can be understood by creating new signal templates to reflect systematic uncertainties. We make a set of signal templates for the following effects. In Chapter 8 we incorporate these *systematic templates* into the limit calculation.

- **Parton showering** The modeling of initial and final state showers described in Section 4.2 is controlled by several free parameters. These determine a cut-off scale for parton showers, the Q^2 dependence of α_s, and the kinematic limits in 1→2 shower splitting. These parameters are varied based on studies of the soft jet distributions in $Z^0 \to \ell\ell$ production events [79]. Four separate samples with more or less initial state radiation, and more or less final state radiation were each used to generate a template.

- **Parton distribution functions** The parton distribution functions for the $p+\bar{p}$ initial state are developed from constrained fits with an array of free parameters [9]. The principal axes of the error ellipsoid determine 20 potential $\pm 1\sigma$ parameterizations which span the uncertainty in parameter space [10]. The relative variations in the distribution functions can then be applied as weights to previously simulated events, to generate the systematic templates. We use Monte Carlo re-weighted in this way to generate an array of signal kinematic templates.

- **Calorimeter energy scale** The uncertainty in the calorimeter jet energy corrections propagates back to the true signal kinematics, since the jet threshold in our event selection will bias the event kinematics. We shift the corrections up and down within their $\pm 1\sigma$ systematic uncertainties to generate a pair of kinematic templates reflecting this potential sample bias.

Changes in signal kinematics should mostly affect the top quark's transverse boost in the laboratory frame[3]. The magnitude of the systematic effect from each of these three sources is suggested by the variation of $\langle \beta\gamma \sin\theta \rangle$ given in Table 7.3.

Systematic source	$\Delta_{\beta\gamma \sin\theta}$
ISR	.001 ±.004
FSR	.004 ±.004
Jet energy scale $\pm 1\sigma$	.004 ±.003
PDF	.001 ±.004

Table 7.3: Effect of radiation, parton distribution function uncertainty, and the jet energy scale on the transverse t boost in accepted events. For the parton distribution function we show the quadrature sum of the difference between the CTEQ eigenvector samples.

7.4.2 Z^0 selection effects on resolution function

If the tracks in our Z^0 sample differ significantly from the signal sample, the resolution function $g(d_0^{\text{obs}} - d_0^{\text{true}})$ might be poorly represented by $Prob(d_0^{\text{obs}})$ in the

---

[3] While the lepton p_T actually varies more, it has negligible effect on the templates.

Z^0 events. In fact Z^0 tracks have a different p_T distribution than the signal, and the track impact parameter resolution is dependent on momentum. Our choice of Z^0 mass window might also introduce a bias, by preferentially selecting track pairs that have not radiated.

Momentum dependence

The p_T distribution of leptons tracks, shown in Figure 7.14, is different in $t\bar{t}$ and Z^0 events. We use the generic track p_T dependence fitted in Figure 4.2 to average the variance in d_0 according to the p_T distribution of electrons in $t\bar{t}$ or Drell-Yan events. This check predicts 36.8 μm resolution for both t and Z^0 electrons: the effect of multiple scattering should therefore be quite small.

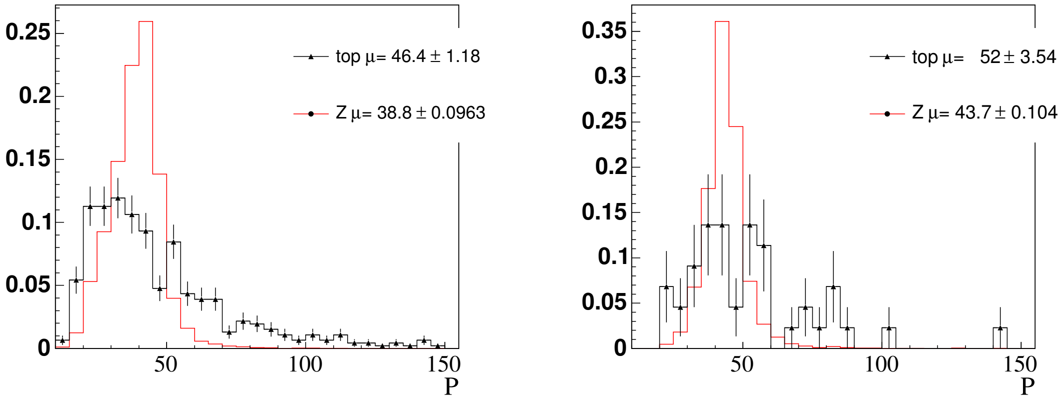

Figure 7.14: Comparison of lepton track momenta in the signal and Z^0 samples. Electron data are shown on the left, and muon data on the right. The ratio of the two distributions in each plot are used to derive a systematic error on the resolution.

Inelastic interactions

By cutting on the invariant mass of electron track pairs to select prompt electrons, we have eliminated backgrounds but perhaps also biased the E/p of the electrons in our sample, and hence the d_0 resolution. In Table 7.4 we compare the observed widths of the resolution functions extracted from the higher E_T Z^0 leg, in varying Z^0 mass windows. All statistically independent samples yield a consistent resolution, except for the lowest mass window, where the difference is 2.1σ. We use the change in $\sigma(d_0)$ when the lower E_T leg of the Z^0 is excluded from the resolution function as a generous estimate of the bias from *bremsstrahlung*. For electrons the change is -2.7 μm, and for muons, it is -0.4 μm.

(m_Z^{min},m_Z^{max})	$\langle d_0 \rangle$	RMS	Mean track p_T
(76,83)	-1.8 ±2.5	40.1 ±1.8	37.6 ±0.6 GeV/c
(83,91)	-2.4 ±0.7	35.8 ±0.5	41.3 ±0.2 GeV/c
(91,99)	-2.3 ±0.8	35.8 ±0.5	43.0 ±0.2 GeV/c
(99,106)	-3.4 ±3.0	35.2 ±2	46.9 ±0.9 GeV/c
(76,106)	-2.3 ±0.5	35.8 ±0.4	42.0 ±0.1 GeV/c

Table 7.4: Resolution for electron tracks calculated from subsamples with varying cuts on the reconstructed m_Z. The average d_0 is also given. The mass windows also select different lepton p_T ranges, so the p_T dependence systematic error found in Section 7.4.2 overlaps with this cross-check.

We also explore the systematic error for this effect by selecting leptons from Z^0 decays that fall into different p_T bins. (This p_T dependence is not entirely independent of either the multiple scattering bias or the E_T effect above.) We scale these resolution functions by the ratio of histograms in Figure 7.14. This procedure generates a sample with weighted p_T identical to the signal sample. We then add the scaled resolution templates together. After rescaling, the resolution shifts +3.99 μm for electrons and

-0.46 μm for muons. We combine the errors in Table 7.5.

High p_T lepton d_0 bias

As is evident in the figures and Table 7.4, $g(d_0^{\rm obs} - d_0^{\rm true})$ is not symmetric for electron or muon impact parameters. This bias would only generate a systematic error if it were specific to Z^0 events – if the bias is common to all high p_T lepton tracks, the smearing procedure used to correct the ideal d_0 templates will appropriately bias the observed variable's templates.

We have investigated this bias using both electrons and muons from W and Z decays. It seems to be a generic feature of high p_T lepton tracks. In Figure 7.15 we show the mean d_0 *vs.* run number for positively and negatively charged tracks in $W + 0$jet candidate events. In Figures 7.16 and 7.17 we show various geometric dependences of the mean d_0. Since the bias is the same for W and Z tracks we assume it is accounted for in our resolution function and do not correct it, or apply any systematic error.

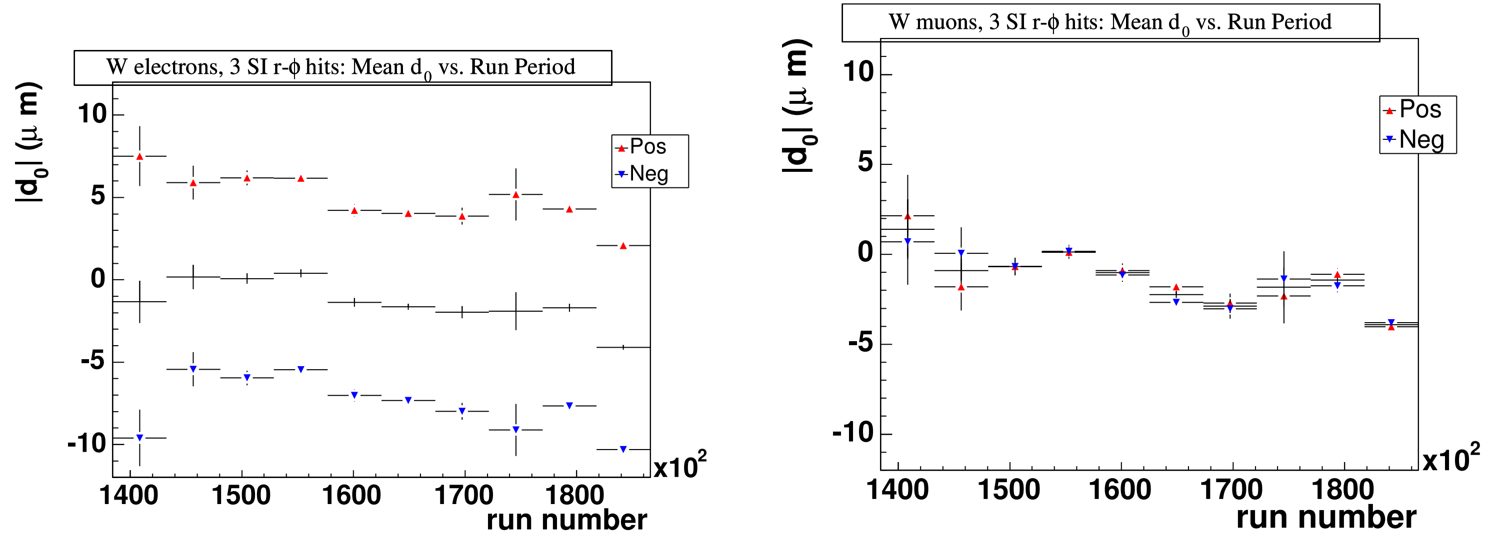

Figure 7.15: Mean d_0 vs. run number for positive vs. negative curvature W electron (left) and muon (right) tracks. The dependence for the positive (▲), negative (▼) and all (no marker) tracks is shown.

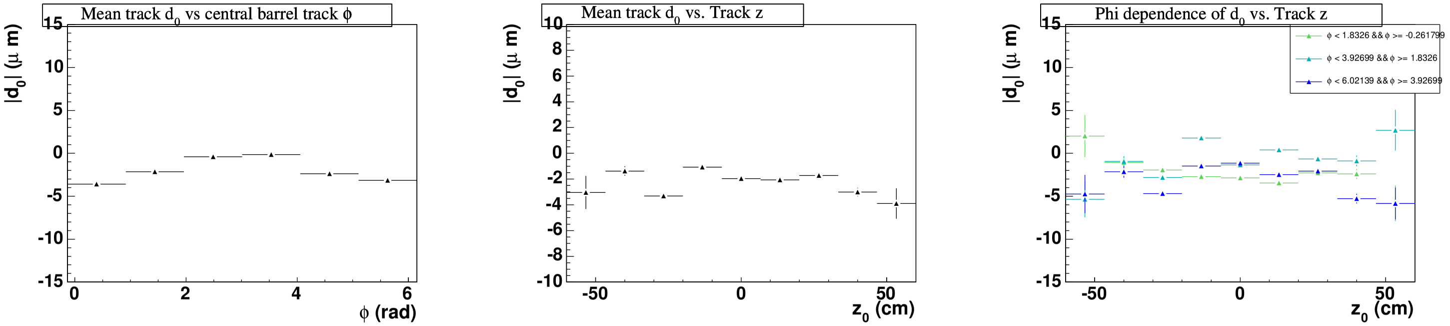

Figure 7.16: Mean d_0 vs. electron track z_0 and ϕ.

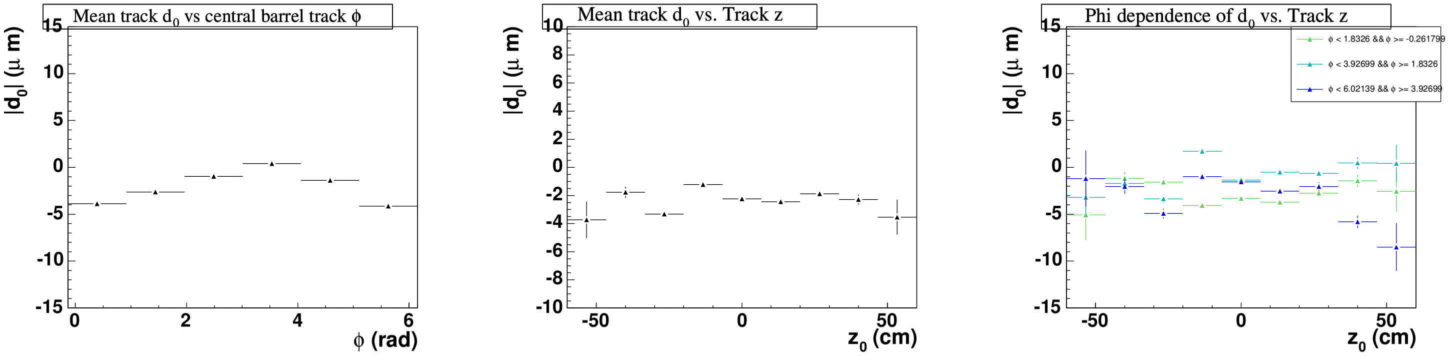

Figure 7.17: Mean d_0 vs. muon track z_0 and ϕ.

Source of error	Electron $\Delta(\sigma_{d_0})$	Muon$\Delta(\sigma_{d_0})$
statistics	± 0.3 μm	± 0.3 μm
Lepton track p_T dependence	$^{+4.0}_{-0}$ μm	± 0.5 μm
Lepton sample bias	$^{+0}_{-2.7}$ μm	± 0.4 μm
Total	$^{+4}_{-2.7}$ μm	± 0.6 μm

Table 7.5: Errors associated with the resolution function.

7.4.3 Background template shape systematics

Bias from "found" conversions

The conversion template necessarily uses identified conversions, and so may be biased by a p_T or r dependence of the conversion identification efficiency. This would create a distortion of the d_0 shape. We assume that this effect is modeled by the simulation, and show the efficiency *vs.* d_0 from true conversions in Figure 7.18. This

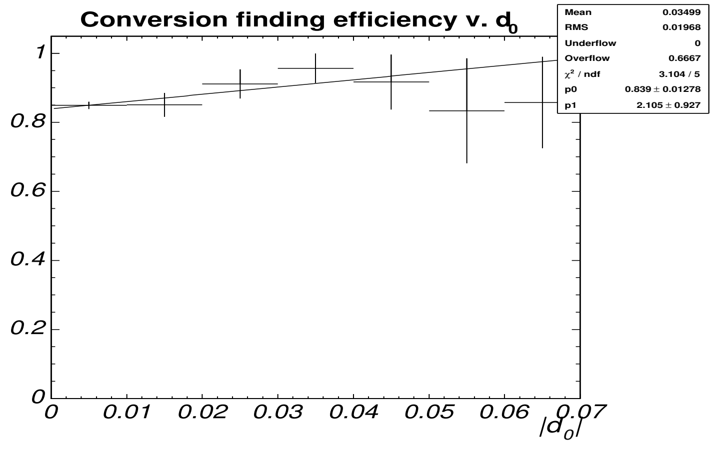

Figure 7.18: Monte Carlo conversion finding efficiency *vs.* electron track d_0.

efficiency increases by 0.1 ±.055 over the impact parameter range $0 < |d_0| < 0.05$. We can test how much an efficiency bias might affect the template. If we compare a Gaussian + exponential fit to the generic conversion d_0 shape in data to a function corrected by a multiplicative efficiency scale factor $SF = (.83 + 2.01|d_0|)$, the prompt fraction is unchanged but the decay constant changes by approximately 2% (Table 7.6). This change is within statistical errors on the fit, but we will increase the error on the conversion decay constants by 2% accordingly.

	Decay constant (μm)	Prompt fraction (%)
Uncorrected fit	106 ±3	76.1 ±.8
Corrected fit	103 ±3	76.7 ±.8

Table 7.6: Change in conversion fit parameters when an efficiency bias is taken into account. The fits were performed for all good conversion tracks, without correcting for a p_T bias.

Heavy flavor model

As demonstrated in Figure 7.19,the Monte Carlo shows no significant change in the shapes of heavy flavor impact parameters at low *vs.* high missing energy. However, in Section 7.3.4 we also note that the heavy flavor *fractions* in the Monte Carlo slightly increase with $\not\!\!E_T$. The slopes of the mean d_0 *vs.* $\not\!\!E_T$ in non-isolated events in the data are also mostly insignificant (Figure 7.20), although there is a $\sim 1\sigma$ increase in $|d_0|$ for non-isolated muons in data. To determine whether the $\not\!\!E_T$ sideband used has a systematic effect on the template shape in data, we consider the effect of this cut on non-isolated events. We compare the fits to tagged, non-isolated events in the 1 and 2 jet bins after imposing different $\not\!\!E_T$ cuts; these comparisons can be found in Figure

7.21. For muons, the overall heavy flavor fraction increases somewhat (14±9%) as we increase the $\not\!\!E_T$ while for electrons the increase is not significant (1±7%). We conclude that the 6±5% correction derived from the slope of the b-fraction in Monte Carlo is reasonable, and apply an additional systematic error of 7%.

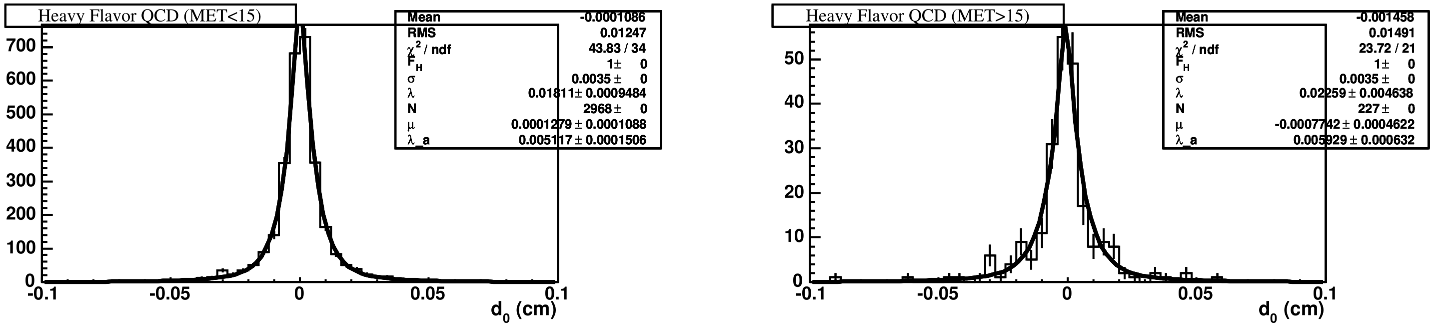

Figure 7.19: The impact parameter distributions of leptons from b and c decays are unrelated to the missing energy in the event in QCD Monte Carlo. The isolation cut was relaxed to Isol < 2.5 to obtain better statistics here.

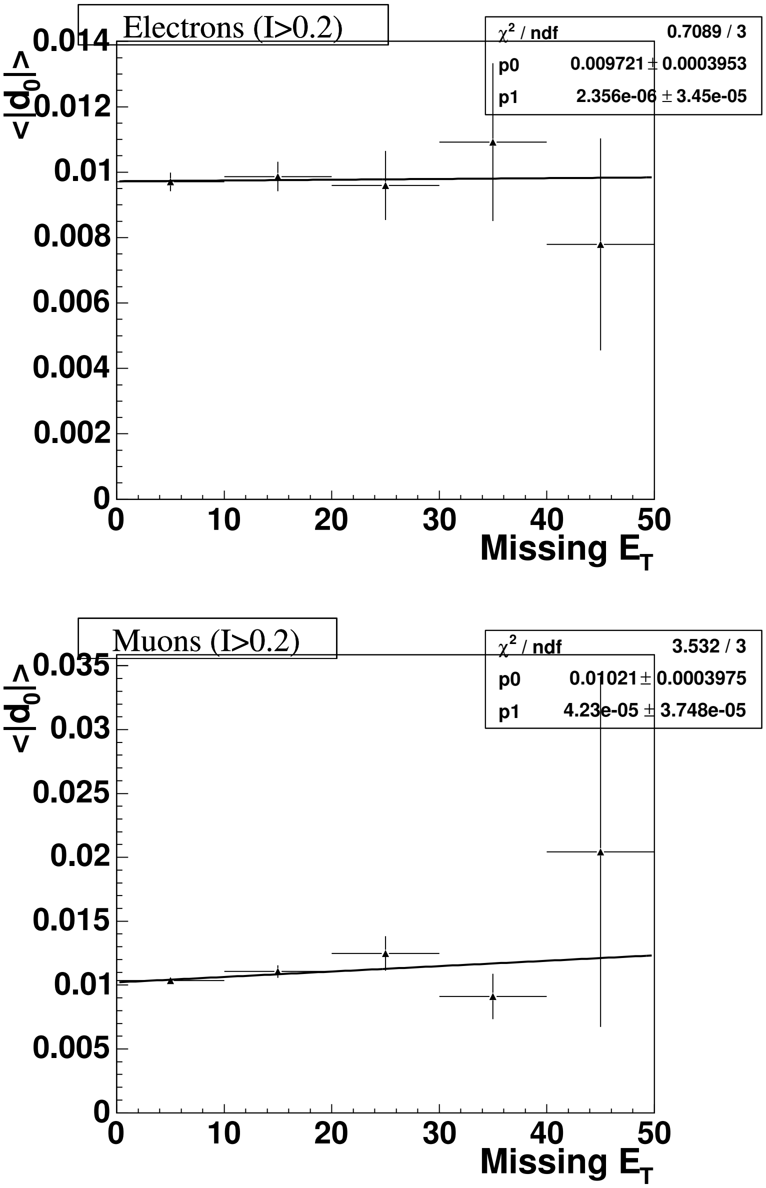

Figure 7.20: The mean (unsigned) impact parameter of leptons in non-isolated tagged events in data is not strongly correlated to the event missing energy.

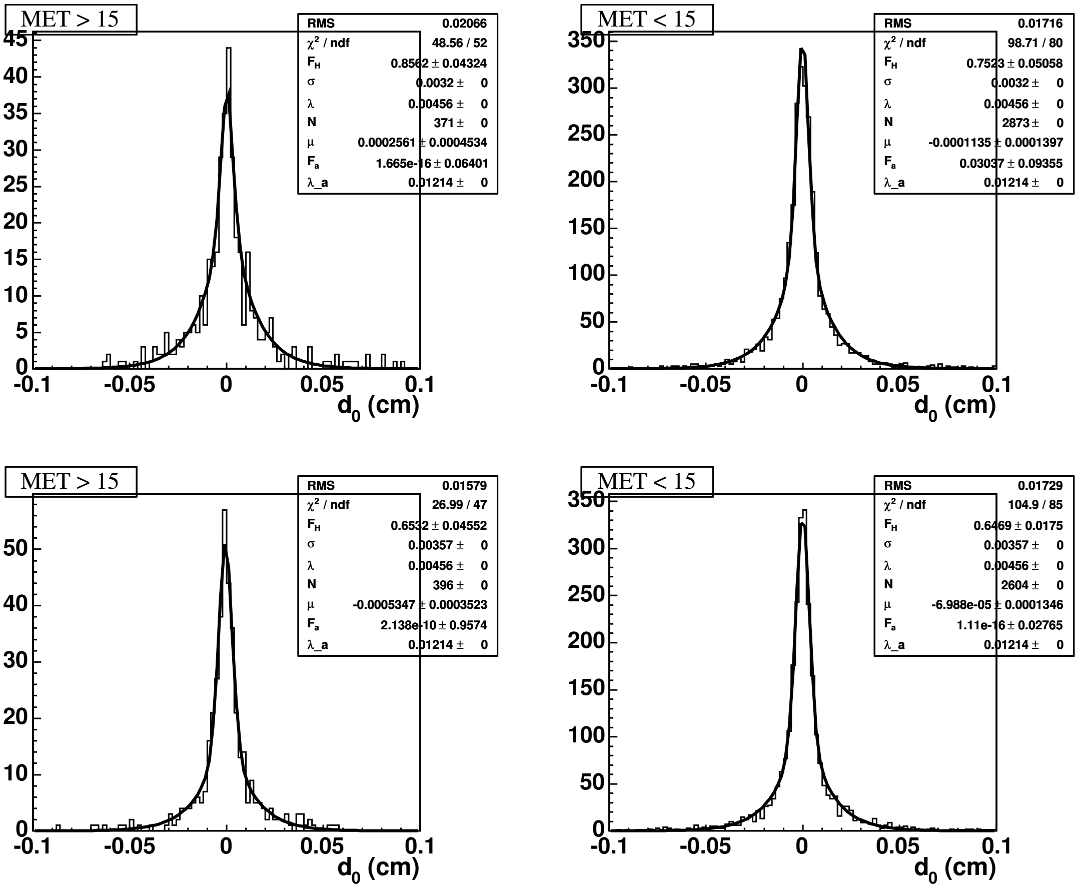

Figure 7.21: Fits to the impact parameter distribution of non-isolated leptons in the 1 and 2 jet bins show slight correlation to missing energy. The upper pair of plots displays muon events; the lower plots are electrons.

Chapter 8

Limits

In previous chapters we have described the event selection that results in 157 $t\bar{t}$ candidate events, filtered from the 318 pb^{-1} of Tevatron data. We have also calculated the number of background events we expect among these candidates. From the discussion of Chapter 6, we learned that there should be approximately 126 t signal events among this data. In Chapter 7 we determined resolution functions ($g_e(d_0^{\text{obs}} - d_0^{\text{true}})$ and $g_\mu(d_0^{\text{obs}} - d_0^{\text{true}})$) for lepton impact parameter measurements using CDF tracking, and determined the track impact parameter distributions for the leptons from background events. Finally, in Section 7.2 we parameterized the d_0^{obs} distribution for leptons from t decays as a function of the top lifetime $c\tau_t$.

Denoting the sample purity $\mathsf{p}_{t\bar{t}} = \frac{N_{t\bar{t}}}{N}$, the distribution of lepton track d_0 in our sample should be well-described by

$$Prob(d_0; c\tau_t, g) = \mathsf{p}_{t\bar{t}} Prob^{t}(d_0; c\tau_t, g) + (1 - \mathsf{p}_{t\bar{t}}) Prob^{!t}(d_0; g)$$

if $c\tau_t$ is the true top mean lifetime. Thus to estimate the top mean lifetime from the W+jets sample, we choose the value of $c\tau_t$ for which the combined likelihood $\mathcal{L}$ of the observed lepton impact parameters, $\prod_{i=1}^{157} Prob(d_0(i); c\tau_t, g)$, is maximal.

In this chapter we calculate this value (which we denote $c\tau_t^{\max\mathcal{L}}$), and explore the probability distributions that describe it. The calculation of $c\tau_t^{\max\mathcal{L}}$ is discussed in Section 8.1. The probability distributions for $c\tau_t^{\max\mathcal{L}}$ are produced by dedicated Monte Carlo simulations (*pseudoexperiments*), which reproduce the maximum likelihood fitting procedure in a large number of generated datasets. We process a set of pseudoexperiments initialized with different true (input) top lifetimes $c\tau_t^{\text{true}}$ in the range $0 \leq c\tau_t^{\text{true}} \leq 500\mu\text{m}$, so that we can generate an approximation to the two-parameter probability distribution[1] $Prob(c\tau_t^{\max\mathcal{L}}|c\tau_t^{\text{true}})$. This method is discussed in Section 8.2.

Based on the set of distributions $Prob(c\tau_t^{\max\mathcal{L}}|c\tau_t^{\text{true}})$ and our observed value of $c\tau_t^{\max\mathcal{L}}$, we finally calculate limits on $c\tau_t^{\text{true}}$, using the Feldman-Cousins construction [80]. Our upper and lower limits thus represent a *confidence interval* for $c\tau_t^{\text{true}}$: they are random variates with a 90% or 95% probability of satisfying $c\tau_t(min) < c\tau_t^{\text{true}} < c\tau_t(max)$, according to the pseudoexperiment-derived probability distributions.

In Section 8.3, we show how this interval is constructed, and how it is affected by the systematic errors described in Chapters 6 and 7.

8.1 Maximum likelihood fit

Rather than a continuous function of $c\tau_t^{\text{true}}$, the template method of Chapter 7 creates a discrete array for the signal probability distribution. After adding backgrounds,

---

[1] By this notation we mean a probability distribution for $c\tau_t^{\max\mathcal{L}}$, *i.e.* a function such that $\int cd(\tau)Prob(c\tau|c\tau_t^{\text{true}}) = 1$.

the array of templates is still discrete. To find the maximum-likelihood value of $c\tau_t$ we calculate the negative logarithm of the likelihood $\mathcal{L}$ for the probability distribution corresponding to every integer value $c\tau_t^{\mathrm{true}}$ in the range $0 \leq c\tau_t^{\mathrm{true}} \leq 500$ μm. While technically, both the signal and background templates used to make the probability distribution function depend on $c\tau_t^{\mathrm{true}}$, the differences between background templates is undetectable for all $c\tau_t^{\mathrm{true}}$(strictly) greater than 0. This is because the background only depends on $c\tau_t^{\mathrm{true}}$ through the magnitude of the single top production cross section[2], which we take to scale as $\sigma_0^{p\bar{p}\to t\bar{b}} \times \left(\frac{1.2\times 10^{-12}\mu\mathrm{m}}{c\tau_t^{\mathrm{true}}}\right)$.

We therefore calculate $-\ln\mathcal{L}$ as a function of the assumed $c\tau_t^{\mathrm{true}}$, and choose the value for which $-\ln\mathcal{L}$ is smallest. This scan is performed with `Minuit` [81].

Using the 157 lepton impact parameters from our signal sample, we find that $-\ln\mathcal{L}$ is minimal at $c\tau_t^{\max\mathcal{L}} = 0$. A quadratic fit to $-\ln(L/L_{\max})$ is plotted against $c\tau_t$ in Figure 8.1. In Figure 8.2, we show the data, compared to the maximum likelihood template.

8.2 Pseudoexperiments

To understand the observed result of an experiment, it is useful to know the outcome's probability distribution as a function of the physical parameter being measured. We have approximated this function ($Prob(c\tau_t^{\max\mathcal{L}}|c\tau_t^{\mathrm{true}})$) for our measurement by repeatedly running a small simulation that produces $c\tau_t^{\max\mathcal{L}}$ according to our likelihood fitting method and simulated lepton impact parameters.

The simulation proceeds in several steps. We describe the process of a single

---

[2] This choice is explained in Section 2.2.4.

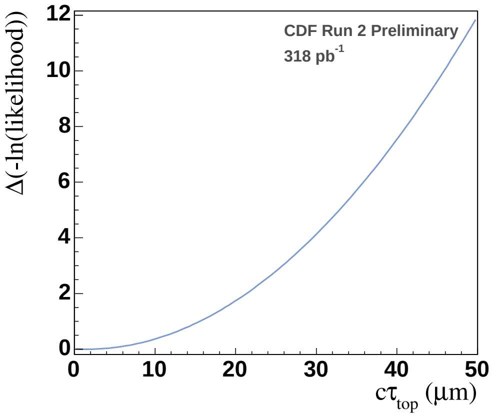

Figure 8.1: Shape of the negative log likelihood curve as a function of $c\tau_t$ (right).

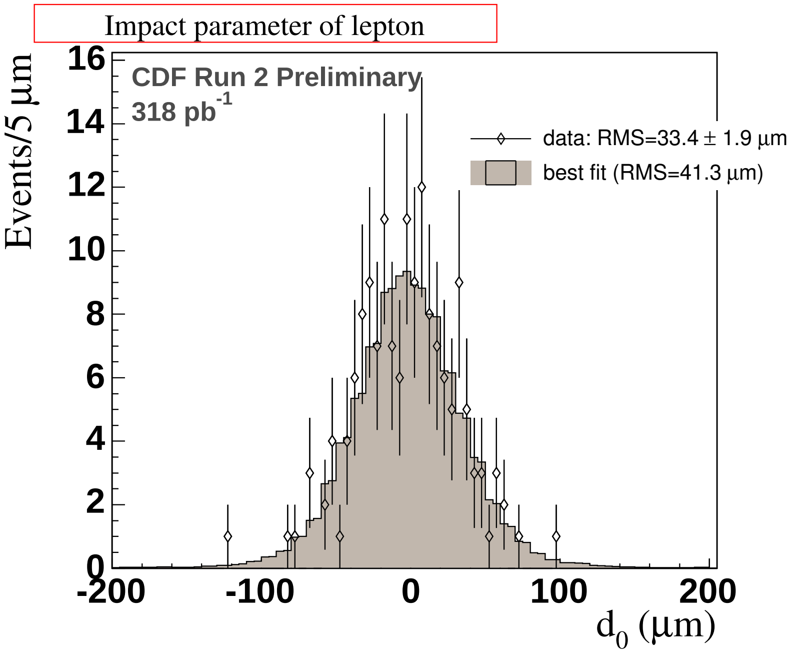

Figure 8.2: Comparison of the 157 lepton candidates to the expected distribution for $c\tau_t = 0$ μm.

pseudoexperiment trial below.

- The trial is assigned a true top mean lifetime. We scan top mean lifetimes between 0 and 500 μm.
- The background measurements are used to determine the simulated sample composition:
  - The central values of the background and t signal estimates of Chapter 6 are collected into an initial vector $\vec{N}_0 \equiv (n_t, n_{\text{prompt}}, n_\tau, n_{\text{QCD}}, n_{\text{conv}})$.
  - $\vec{N}_0$ is smeared by the systematic errors in Table 6.5 to produce another vector, $\vec{N}$. Some errors (the scale factors, efficiencies and luminosity errors) are correlated among different backgrounds, as discussed in Section 6.2, and these affect the components of $\vec{N}$ coherently. The systematic uncertainty on each parameter is assumed to represent the width of a Gaussian probability distribution for the parameter.
  - The components of the systematically smeared vector $\vec{N}$ are then used as the means of Poisson distributions to generate the trial background composition $\vec{N}_{\text{trial}}$ and the total event multiplicity $N_{\text{trial}} = \sum_{i=1}^{5} N_{\text{trial}}(i)$.
- Template shapes for the signal and each background are chosen from the template measurements in Chapter 7; the fit parameters are allowed to vary within their statistical and systematic errors.
- Having determined the sample composition and the generating distributions for this trial, we select N_{trial} impact parameters from the template shapes.

- The pseudoexperiment data is fit with the maximum likelihood procedure, using our initial estimates of the backgrounds ($\vec{N}_0$) and template parameterizations.

This procedure is repeated 2400 times for each trial value of $c\tau_t^{\rm true}$. Example distributions are shown in Figure 8.3.

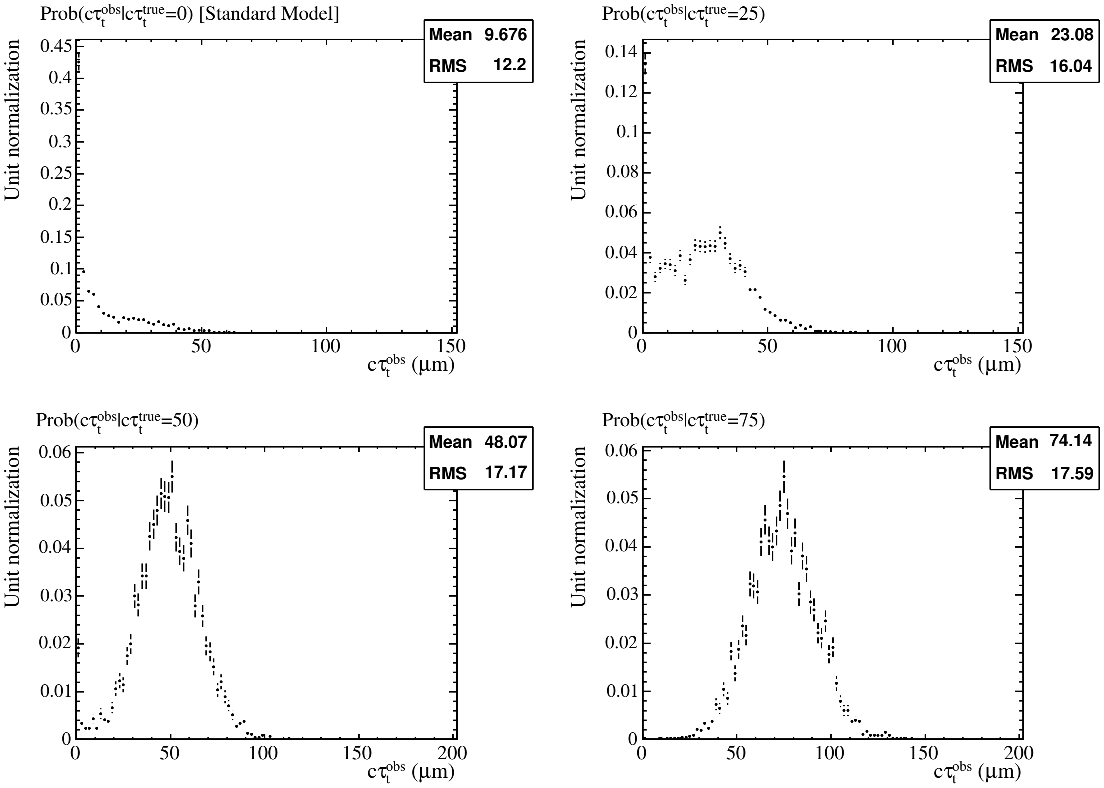

Figure 8.3: Probability distributions extracted from the function $P(c\tau_t^{\max\mathcal{L}}|c\tau_t^{\rm true})$. These are slices of the parameterized distribution function constructed via pseudoexperiments.

.

8.2.1 Error inclusion

The procedure above accounts for statistical errors and the systematic errors on the backgrounds, which were determined in Chapter 6. It is more difficult to change the signal model in every pseudoexperiment trial according to the template systematic errors from Chapter 7. These sources of error affect the top kinematic distributions, which are used to construct the signal template shapes used for every trial value of $c\tau_t^{\mathrm{true}}$. Allowing these parameters to fluctuate in every trial would involve many iterations of constructing the signal template array. The same difficulty arises for the systematic error on the resolution function.

Instead of varying these systematic parameters continuously within the pseudoexperiment trials, we determine our sensitivity to these effects using the "$\pm 1\sigma$" systematic templates described Section 7.4.1. We generate new sets of pseudoexperiments from each systematic template, and compare the generated $Prob(c\tau_t^{\mathrm{max}\mathcal{L}}|c\tau_t^{\mathrm{true}})$ from these templates to one another and to the default distribution displayed in Figure 8.3. Differences among these distributions indicate how our limit is influenced by systematic errors.

In Figures 8.4 and 8.5, we compare the probability distributions of $c\tau_t^{\mathrm{max}\mathcal{L}}$ from this procedure, for a few values of $c\tau_t^{\mathrm{true}}$. These are fit for every input $c\tau_t^{\mathrm{true}}$ value to the sum of a Gaussian distribution and a exponential centered at $c\tau_t^{\mathrm{max}\mathcal{L}}=0$. An additional delta function at the origin is added, to reflect the tendency of the likelihood fitter to return exactly zero[3].

---

[3] This occurs when the width of the generated distribution fluctuates lower than the width of the resolution function. Since the fitter returns zero even when the fitted log likelihood curve has a minimum at negative values, there is a discontinuity in this bin.

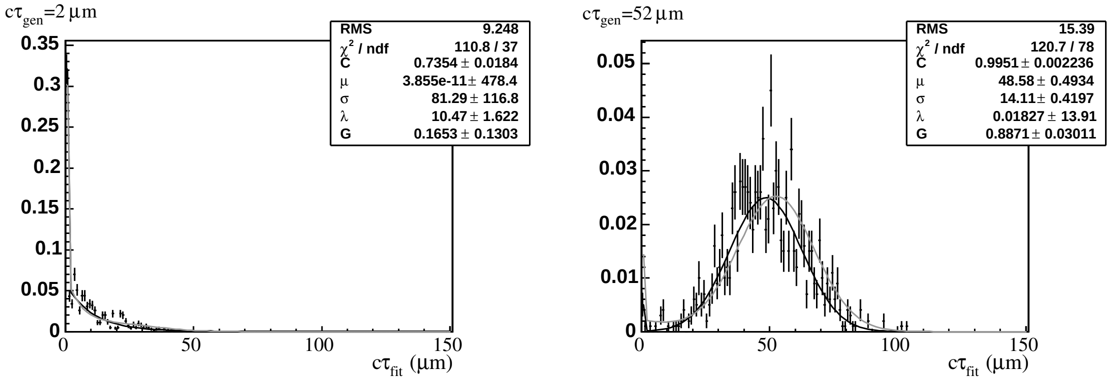

(a) PDF systematic study. $+1\sigma$(black, points); -1σ (grey).

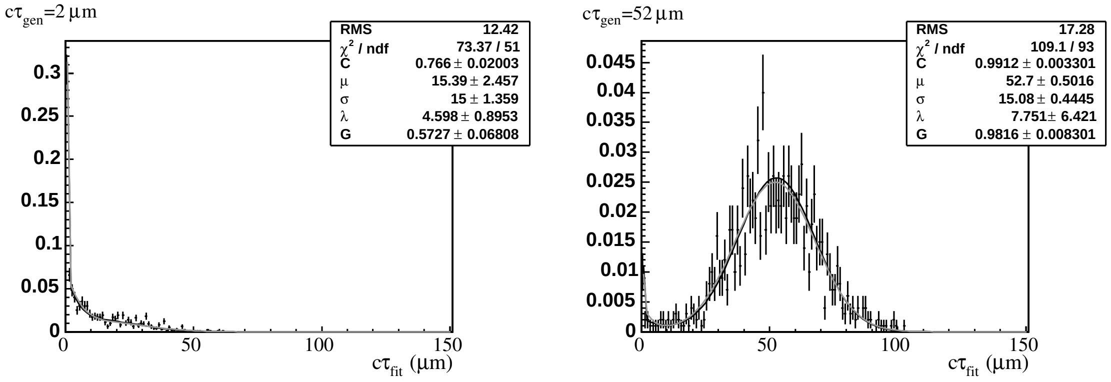

(b) Jet energy scale: $+1\sigma$(black, points); -1σ (grey).

Figure 8.4: Comparison of probability distributions for $c\tau_t^{\max\mathcal{L}}$ extracted from the systematic samples, for given values of $c\tau_t^{\text{true}}$. For clarity the points are only shown for the first sample, but all fits are shown.

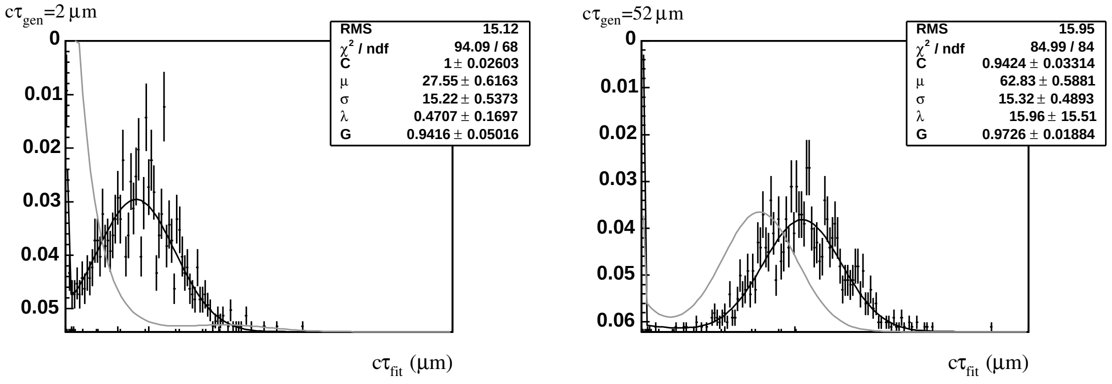

(c) Resolution function: $+1\sigma$(black, points); -1σ (grey).

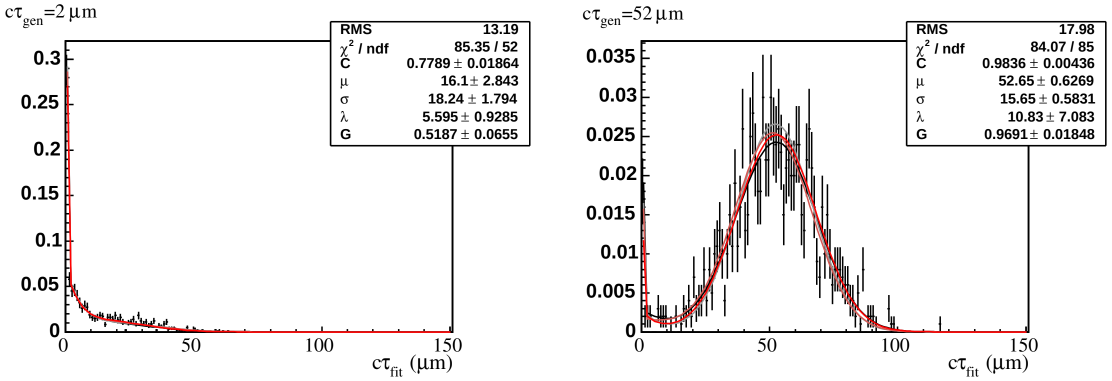

(d) Parton showering: more FSR(black, points); less(grey); more ISR(red); less(pink).

Figure 8.5: Comparison of probability distributions for $c\tau_t^{\max\mathcal{L}}$ extracted from the systematic samples, for given values of $c\tau_t^{\text{true}}$. The dominant systematic is the uncertainty in $g(d_0^{\text{obs}} - d_0^{\text{true}})$, with most pronounced effects for small values of $c\tau_t^{\text{true}}$.

We use the difference in the fit parameters for each pair of $\pm1\sigma$ systematic samples to determine the dependence of the probability distribution on each systematic effect. We then apply the variation in fit parameters as a smearing of the probability distributions used in the likelihood-ratio ordering procedure.

8.3 Results

From the maximum-likelihood fit we have found that $c\tau_t^{\max\mathcal{L}}= 0$, so the Standard Model is not challenged by our measurement. To more fully interpret this result, we use the pseudoexperiment trials to express our uncertainty in the true parameter $c\tau_t^{\mathrm{true}}$ by quoting an interval $(c\tau_t^{\min}, c\tau_t^{\max})$ which has a given probability α of containing the true parameter[4]. We quote limits for $\alpha = 95\%$ and 90%.

The Neymann construction provides a way to extract such intervals from the $Prob(c\tau_t^{\max\mathcal{L}}; c\tau_t^{\mathrm{true}})$ function. For every value of $c\tau_t^{\mathrm{true}}$, we choose a subset of the possible $c\tau_t^{\max\mathcal{L}}$ values such that $\int d(c\tau_t^{\max\mathcal{L}})Prob(c\tau_t^{\max\mathcal{L}}|c\tau_t^{\mathrm{true}})e = \alpha$ (because our parameterization is discrete, the integral may be slightly larger than α). Our limit, based on our observation $c\tau_t^{\mathrm{obs}}$, is the range of $c\tau_t^{\mathrm{true}}$ for which $c\tau_t^{\mathrm{obs}}$ is within the chosen subset.

By using the likelihood ratio (Feldman-Cousins) ordering principle [80] to determine the set we accomplish two desirable goals – we automatically include the value of $c\tau_{\mathrm{true}}$ for which the fit result is most probable within the interval, and we avoid the necessity of choosing in advance between constructing one-sided and two-sided

---

[4] Here it should be understood that the interval, and not the true parameter, is the random element.

intervals. Our confidence belts, derived using the systematically smeared probability distributions $Prob(c\tau_t^{\max\mathcal{L}} — c\tau_t^{\text{true}})$, are shown in Figure 8.6. From the confidence range at $c\tau_t^{\max\mathcal{L}} = 0$, we derive a limit:

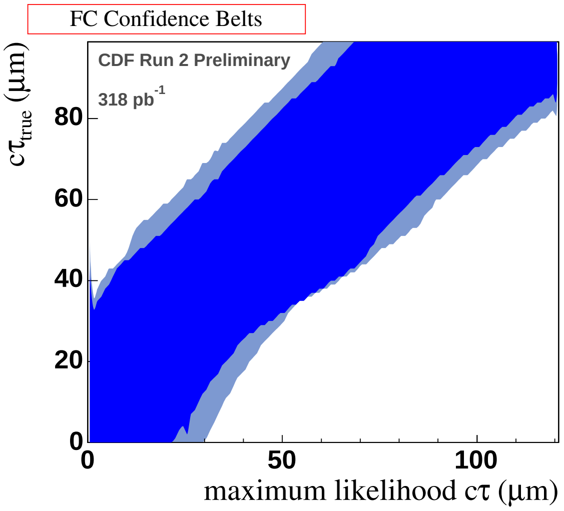

Figure 8.6: Feldman-Cousins confidence intervals for the true top lifetime, as a function of the fit result $c\tau_{\text{fit}}$. The dark region represents the 90% C.L. intervals; the lighter regions extend this to 95%. These contours are constructed from the pseudo-experiment procedure described in the text, which accounts for background systematics. The parameterized probability distribution functions from which these intervals are made is smeared to incorporate the "shape" systematic errors.

$$\begin{aligned} c\tau_t &< 52.5\mu\text{m} \,@\, 95\% \text{ C.L.} \\ c\tau_t &< 43.5\mu\text{m} \,@\, 90\% \text{ C.L.} \end{aligned} \tag{8.1}$$

8.4 Conclusions

Our measurement has demonstrated that the impact parameter distributions of leptons in the venerable lepton+jets top sample are consistent with the detector resolution and the Standard Model backgrounds. While the limit we have calculated is dependent on the simple long-lived top model we concocted, the actual measurement technique was applied with very few assumptions about the top candidate events. It is hardly surprising that our data is not well-explained by a long-lived top template, but the agreement with the standard model template is nevertheless compelling: while there is still plenty of room for an anomalous top lifetime in the data, we have ruled out any top lifetimes that might artificially increase the efficiency to b-tag $t\bar{t}$ events, or increase the measured value of m_t in track-based top mass analyses.

Future improvements The analysis suffers most from the small $t\bar{t}$ sample size and from the systematic uncertainty in the resolution function $g_e(d_0^{\mathrm{obs}} - d_0^{\mathrm{true}})$. This function is especially uncertain for electron tracks because the sample in which we measured the resolution might be biased against electrons that have radiated and which therefore have poor impact parameter resolution. Studies comparing these effects for electrons from top candidate events and from (Z^0) candidates should benefit from increased statistics. As more data is collected at CDF, the measurement could also be performed using muon+jets top candidate events exclusively.

Projections The error from the likelihood fit procedure decreases like a statistical error, as $\frac{1}{\sqrt{N}}$ when the dataset is increased N times. Most the systematic errors on the background templates will also scale like statistical errors. The Tevatron is expected to deliver 4 pb^{-1} of integrated luminosity to CDF before Run II ends; with a dataset this size we might achieve an upper limit on $c\tau_t$ of about 33 μm, conservatively assuming that the signal template shape systematic errors were not improved at all.

Further studies This measurement invites two interesting complementary analyses. The first is a similar measurement in the $t\bar{t}$ dilepton decay channel. By comparing the impact parameters of the two leptons to one another, the analysis would probe a different set of possible long-lived backgrounds to t production. The other analysis would be a study of the t lifetime relative to the timescale of soft QCD interactions. As explained in Section 2.3.1, the demonstration of $t\bar{t}$ spin correlations, which would be washed out by QCD interactions for t quarks with lifetimes exceeding 10^{-22} s, might be the most fruitful indirect search strategy.

Ultimately, the detection of single top pair-production at the Tevatron or the LHC will lay the idea of long-lived top to rest. Nevertheless, the lepton impact parameter method might survive it as an independent and useful probe of unexpected backgrounds.

Appendix A

Background and signal in W+jets

For the background normalization measurement, we perform a simultaneous determination of the number of $t\bar{t}$ events, the QCD background (excluding electrons from photon conversions, which are measured separately), and the non-top W+jets background. Here we outline this procedure, which is based on the method used to measure the non-resonant W+jets production rates in [77]. We take the backgrounds estimated from Monte Carlo (dibosons, single top, and $Z^0 \rightarrow \tau\tau$) into account.

Our method should be roughly equivalent to the iterative method usually used to find the W+jets background in the top cross section measurement[76], but this formulation makes the statistical dependence of the top cross section on the $W^{\pm}$ and QCD backgrounds explicit, and allows us to easily include the Z^0+jets background with a floating normalization[1].

---

[1] As for the W+jets background, we cannot accurately fix the $p + \bar{p} \rightarrow Z + \geq 3P$ cross section that matches our generated $Z + \geq 3P$ events.

A.1 Missing energy and isolation

The separation of true $W^{\pm}$ processes (including $t\bar{t}$) from the QCD background relies on the assumption that missing energy and lepton isolation are uncorrelated variables in an event. The joint distribution of these variables for our pre-tag sample is plotted in Figure A.1. The apparent correlation is a property of our mixed sample, which includes processes with different $\not\!\!E_T$ and I distributions. Specifically, there is a set of events in which the lepton and a large missing energy have the same source: the $W^{\pm}$ boson. If the remainder of the events in this sample have the same $\not\!\!E_T$ distributions, dominated by the missing transverse energy resolution, then we need only remove the $W^{\pm}$ events to determine this $\not\!\!E_T$ shape. Since the anti-isolation cut removes most $W^{\pm}$ events, the missing energy distribution of the non-$W^{\pm}$ background should be measurable with non-isolated lepton events.

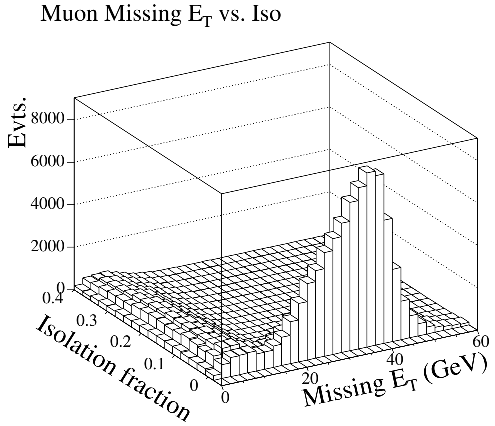

Figure A.1: Correlation between missing energy and isolation variables. The pre-tag muon sample described in Chapter 5 is used for illustration.

We can check that the isolation and $\not\!\!E_T$ are intrinsically uncorrelated with the conversion sample (the selection of this sample is explained in Appendix B). This data should have small contamination from $W^{\pm}$ events. The missing transverse energy in conversion events is plotted in Figure A.2, for two different regions of electron isolation. Except for some probable W events at high missing E_T, the agreement is acceptable. We thus use the relation

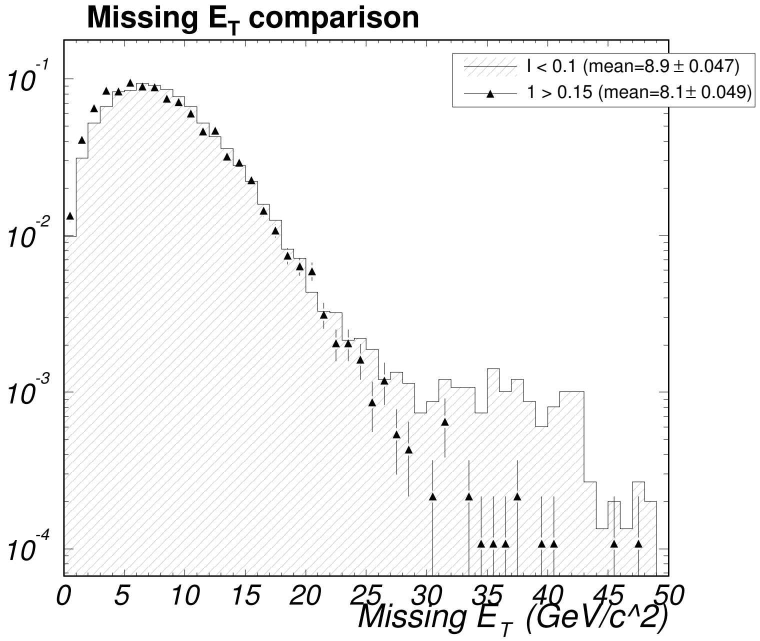

Figure A.2: The $\not\!\!E_T$ of conversion events with isolation > 0.1 is compared to the $\not\!\!E_T$ of events with electron isolation > 0.15. The sample selection is described in Appendix B.

$$\frac{\boxed{N_{\mathrm{QCD}}}^{D}}{\boxed{N_{\mathrm{QCD}}}^{B}} = \frac{\boxed{N_{\mathrm{QCD}}}^{C}}{\boxed{N_{\mathrm{QCD}}}^{A}} \tag{A.1}$$

in Section 6.1.5 to extract the non-W backgrounds.

A.2 Untangling contributions to the W+jets sample

Our method can be thought of as a fit to the two-dimensional $\not\!\!E_T$-I distribution of the data set, using Monte Carlo models for the shapes of W+jets, $t\bar{t}$, and most backgrounds, and a parameterized shape with three unknowns for the QCD background. In fact, our two-dimensional $\not\!\!E_T$-I distribution is coarsely binned into four noncontiguous bins, and most backgrounds are fixed or constrained so that only $\boxed{N_{\rm W}}$, $\boxed{N_{t\bar{t}}}$, and the three QCD background parameters $\boxed{N_{\rm QCD}}^{A}$, $\boxed{N_{\rm QCD}}^{B}$ and $\boxed{N_{\rm QCD}}^{C}$ can float. Since there are five data points (the total event yields in each region – $\boxed{N_{\rm obs}}_{A}$, $\boxed{N_{\rm obs}}_{B}$, $\boxed{N_{\rm obs}}_{C}$ and $\boxed{N_{\rm obs}}_{D}$ – and the number of secondary vertex tagged events in the signal region $\boxed{N_{+,\rm obs}}_{D}$) the fit is unconstrained[2]. The system of five equations amounts to Equation A.1 and

$$
\begin{aligned}
\sigma_W \cdot {\rm Br}(W^{\pm} \to \ell\nu)/\sigma_Z \cdot {\rm Br}(Z^0 \to \ell\ell) &= 10.69 \equiv \rho \qquad \text{(A.2)}\\
\sigma_W \cdot {\rm Br}(W^{\pm} \to \ell\nu)/\sigma_W \cdot {\rm Br}(W^{\pm} \to \tau\nu) &= 1.\\
\boxed{N_{\rm obs}}^{D} - \sum_{bg} \boxed{a_{\rm bg}}^{D} \boxed{N_{\rm bg}} - \sum_{ewk} \boxed{a_{\rm ewk}}^{D} \mathcal{L}\sigma_{ewk} - \boxed{N_{\rm QCD}}^{D} &= \boxed{a_{\rm top}}^{D} \mathcal{L}\sigma_{t\bar{t}}\\
&\equiv \boxed{N_{\rm top}}\\
\boxed{N_{+}}^{D} - \sum_{bg} \boxed{a_{+,\rm bg}}^{D} \boxed{N_{\rm bg}} - \sum_{ewk} \boxed{a_{+,\rm ewk}}^{D} \mathcal{L}\sigma_{ewk} - \boxed{N_{+,\rm QCD}}^{D} &= \boxed{a_{+,\rm top}}^{D} \mathcal{L}\sigma_{t\bar{t}}\\
&\equiv \boxed{N_{+,\rm top}}^{D}
\end{aligned}
$$

where the product of the acceptance and efficiency for events of type "bg" in $\not\!\!E_T$-I

---

[2] Performing this decomposition in different N_{jet} bins could allow a constrained fit, if the $N_{\rm jet}$ distribution is predicted well for several processes.

region “X” is denoted $\boxed{a_{\text{bg}}}^X$. Note that Equation A.2 holds when the inclusive W/Z production processes involve the same QCD corrections; we use fixed-order Alpgen $W/Z+N$ parton simulations to ensure that these constraints will be satisfied.

We solve the system of equations below.

$$\begin{aligned}
\boxed{N_{\text{obs}}}_J^X &= \boxed{N_{\text{W}}}_J^X + \boxed{N_{\text{Z}}}_J^X + \boxed{N_{W\triangleright\tau}}_J^X + \boxed{N_{\text{top}}}_J^X + \boxed{N_{\text{MC}}}_J^X + \boxed{N_{\text{QCD}}}_J^X \\
&= \boxed{N_{\text{W}}}(\boxed{a_{\text{W}}}_J^X + \rho\boxed{a_{\text{Z}}}_J^X + \boxed{a_{W\triangleright\tau}}_J^X) + \boxed{N_{\text{top}}}_J^X + \boxed{N_{\text{MC}}}_J^X + \boxed{N_{\text{QCD}}}_J^X \\
&= \frac{\boxed{N_{\text{W}}}_J^D}{\boxed{a_{\text{W}}}_J^D}(\boxed{a_{\text{W}}}_J^X + \rho\boxed{a_{\text{Z}}}_J^X + \boxed{a_{W\triangleright\tau}}_J^X) + \boxed{N_{\text{top}}}_J^X + \boxed{N_{\text{MC}}}_J^X + \boxed{N_{\text{QCD}}}_J^X
\end{aligned} \tag{A.3}$$

Representing the probability of tagging an event of type “bg” by p^+_{bg}, we can wrute

$$\begin{aligned}
\boxed{N_{\text{top}}} &= \frac{\boxed{N_{+,\text{obs}}}_3^D - \boxed{N_{+,\text{W}}}_3^D - \boxed{N_{+,\text{Z}}}_3^D - \boxed{N_{+,W\triangleright\tau}}_3^D - \boxed{N_{+,\text{MC}}}_3^D - \boxed{N_{+,\text{QCD}}}_3^D}{p^+_{\text{top}}\boxed{a_{\text{top}}}_3^D} \\
&= \frac{1}{p^+_{\text{top}}\boxed{a_{\text{top}}}_3^D} \times \left(\boxed{N_{+,\text{obs}}}_3^D - \frac{\boxed{N_{\text{W}}}_3^D}{\boxed{a_{\text{W}}}_3^D}(p^+_W\boxed{a_{\text{W}}}_3^D + p^+_Z\rho\boxed{a_{\text{Z}}}_3^D + p^+_{W\triangleright\tau}\boxed{a_{W\triangleright\tau}}_3^D)\right) \\
&\quad - \frac{1}{p^+_{\text{top}}\boxed{a_{\text{top}}}_3^D} \times \left(p^+_{MC}\boxed{N_{\text{MC}}}\boxed{a_{\text{MC}}}_3^D + p^+_{QCD}\boxed{N_{\text{QCD}}}_3^D\right).
\end{aligned} \tag{A.4}$$

When $J=3$, we can solve exactly for the backgrounds:

$$\boxed{N_{\text{obs}}}_3^X - \boxed{N_{\text{MC}}}_3^X = \frac{\boxed{N_{\text{W}}}_3^D}{\boxed{a_{\text{W}}}_3^D}(\boxed{a_{\text{W}}}_3^X + \rho\boxed{a_{\text{Z}}}_3^X + \boxed{a_{W\triangleright\tau}}_3^X) + \boxed{N_{\text{top}}}_3^X + \boxed{N_{\text{QCD}}}_3^X$$

Since

$$\begin{aligned}\boxed{N_{\text{top}}}_3^X \quad = \quad & \boxed{a_{\text{top}}}_3^X \frac{\boxed{N_{+,\text{obs}}}_3^D}{p^+_{\text{top}}\boxed{a_{\text{top}}}_3^D} - \frac{\boxed{a_{\text{top}}}_3^X}{p^+_{\text{top}}\boxed{a_{\text{top}}}_3^D}\frac{\boxed{N_{\text{W}}}_3^D}{\boxed{a_{\text{W}}}_3^D}\left(p^+_W\boxed{a_{\text{W}}}_3^D + p^+_Z\rho\boxed{a_{\text{Z}}}_3^D + p^+_{W\triangleright\tau}\boxed{a_{W\triangleright\tau}}_3^D\right) \\ & - \frac{p^+_{MC}\boxed{a_{\text{top}}}_3^X}{p^+_{\text{top}}\boxed{a_{\text{top}}}_3^D}\boxed{N_{\text{MC}}}_3^D - \frac{p^+_{QCD}\boxed{a_{\text{top}}}_3^X}{p^+_{\text{top}}\boxed{a_{\text{top}}}_3^D}\boxed{N_{\text{QCD}}}_3^D\end{aligned} \tag{A.5}$$

we have

$$\begin{aligned}& \boxed{N_{\text{obs}}}_3^X - \boxed{N_{\text{MC}}}_3^X + \boxed{N_{\text{MC}}}_3^D \frac{p^+_{MC}\boxed{a_{\text{top}}}_3^X}{p^+_{\text{top}}\boxed{a_{\text{top}}}_3^D} - \frac{\boxed{a_{\text{top}}}_3^X}{p^+_{\text{top}}\boxed{a_{\text{top}}}_3^D}\boxed{N_{+,\text{obs}}}_3^D = \\ & \frac{\boxed{N_{\text{W}}}_3^D}{\boxed{a_{\text{W}}}_3^D}\left[\left(\boxed{a_{\text{W}}}_3^X - \boxed{a_{\text{top}}}_3^X \frac{p^+_W\boxed{a_{\text{W}}}_3^D}{p^+_{\text{top}}\boxed{a_{\text{top}}}_3^D}\right) + \left(\rho\boxed{a_{\text{Z}}}_3^X - \boxed{a_{\text{top}}}_3^X \frac{p^+_Z\boxed{a_{\text{Z}}}_3^D}{p^+_{\text{top}}\boxed{a_{\text{top}}}_3^D}\right) + \right. \\ & \left.\left(\boxed{a_{W\triangleright\tau}}_3^X - \boxed{a_{\text{top}}}_3^X \frac{p^+_{W\triangleright\tau}\boxed{a_{W\triangleright\tau}}_3^D}{p^+_{\text{top}}\boxed{a_{\text{top}}}_3^D}\right)\right] - \frac{p^+_{QCD}\boxed{a_{\text{top}}}_3^X}{p^+_{\text{top}}\boxed{a_{\text{top}}}_3^D}\boxed{N_{\text{QCD}}}_3^D + \boxed{N_{\text{QCD}}}_3^X\end{aligned} \tag{A.6}$$

We insert the solution for region D into the other three equations, with the simplification

$$q_X = \frac{\dfrac{p^+_{QCD}\boxed{a_{\text{top}}}_3^X}{p^+_{\text{top}}\boxed{a_{\text{top}}}_3^D}}{1 - \dfrac{p^+_{QCD}}{p^+_{\text{top}}}} \tag{A.7}$$

to obtain

$$\begin{aligned}
&\boxed{N_{\mathrm{obs}}}_3^X - \boxed{N_{\mathrm{MC}}}_3^X + \boxed{N_{\mathrm{MC}}}_3^D \frac{p_{MC}^{+}\boxed{a_{\mathrm{top}}}_3^X}{p_{\mathrm{top}}^{+}\boxed{a_{\mathrm{top}}}_3^D} - \frac{\boxed{a_{\mathrm{top}}}_3^X}{p_{\mathrm{top}}^{+}\boxed{a_{\mathrm{top}}}_3^D}\boxed{N_{+,\mathrm{obs}}}_3^D - \\
&q_X \times \left(\boxed{N_{\mathrm{obs}}}_3^X - \boxed{N_{\mathrm{MC}}}_3^X + \boxed{N_{\mathrm{MC}}}_3^D \frac{p_{MC}^{+}\boxed{a_{\mathrm{top}}}_3^X}{p_{\mathrm{top}}^{+}\boxed{a_{\mathrm{top}}}_3^D} - \frac{\boxed{a_{\mathrm{top}}}_3^X}{p_{\mathrm{top}}^{+}\boxed{a_{\mathrm{top}}}_3^D}\boxed{N_{+,\mathrm{obs}}}_3^D\right) \\
&\quad = \frac{\boxed{N_{\mathrm{W}}}_3^D}{\boxed{a_{\mathrm{W}}}_3^D}\left[\left(\boxed{a_{\mathrm{W}}}_3^X - \boxed{a_{\mathrm{top}}}_3^X \frac{p_W^{+}\boxed{a_{\mathrm{W}}}_3^D}{p_{\mathrm{top}}^{+}\boxed{a_{\mathrm{top}}}_3^D}\right)\right. \\
&\qquad \left. + \left(\rho\boxed{a_{\mathrm{Z}}}_3^X - \boxed{a_{\mathrm{top}}}_3^X \frac{p_Z^{+}\boxed{a_{\mathrm{Z}}}_3^D}{p_{\mathrm{top}}^{+}\boxed{a_{\mathrm{top}}}_3^D}\right) + \left(\boxed{a_{W\triangleright\tau}}_3^X - \boxed{a_{\mathrm{top}}}_3^X \frac{p_{W\triangleright\tau}^{+}\boxed{a_{W\triangleright\tau}}_3^D}{p_{\mathrm{top}}^{+}\boxed{a_{\mathrm{top}}}_3^D}\right)\right] \\
&\qquad - q_X \times \frac{\boxed{N_{\mathrm{W}}}_3^D}{\boxed{a_{\mathrm{W}}}_3^D}\left[\left(\boxed{a_{\mathrm{W}}}_3^D - \boxed{a_{\mathrm{top}}}_3^D \frac{p_W^{+}\boxed{a_{\mathrm{W}}}_3^D}{p_{\mathrm{top}}^{+}\boxed{a_{\mathrm{top}}}_3^D}\right) + \left(\rho\boxed{a_{\mathrm{Z}}}_3^D - \boxed{a_{\mathrm{top}}}_3^D \frac{p_Z^{+}\boxed{a_{\mathrm{Z}}}_3^D}{p_{\mathrm{top}}^{+}\boxed{a_{\mathrm{top}}}_3^D}\right)\right. \\
&\qquad \left. + \left(\boxed{a_{W\triangleright\tau}}_3^D - \boxed{a_{\mathrm{top}}}_3^D \frac{p_{W\triangleright\tau}^{+}\boxed{a_{W\triangleright\tau}}_3^D}{p_{\mathrm{top}}^{+}\boxed{a_{\mathrm{top}}}_3^D}\right)\right] + \boxed{N_{\mathrm{QCD}}}_3^X .
\end{aligned} \tag{A.8}$$

A.2.1 Systematics from $W/Z + (2p)$ events in $W/Z + 3j$ data

The procedure relies on two important assumptions. First, lepton identification scale factors and marginal trigger efficiencies should be the same for $W \to \ell\nu$, $W \to \tau\nu$, and $Z \to \ell\ell$ events once additional leptons are vetoed. It also depends on the assumption that the fraction of events with fewer than N partons migrating into the $\geq N$ jet sample is the same for each electroweak background.

For the $Z^0 \to e^+e^-$ background, there is a large probability that the second electron will be reconstructed as a tight jet, as shown in Figure A.3. Since we only use $W^{\pm}/Z^0 + N$ parton Monte Carlo samples to model the $\ell + \not{E}_T + N$ jet bin, these "promoted" Z events are an unaccounted-for background. For our purposes, counting electroweak $N-1$ parton events in the N parton sample is harmless as long as the

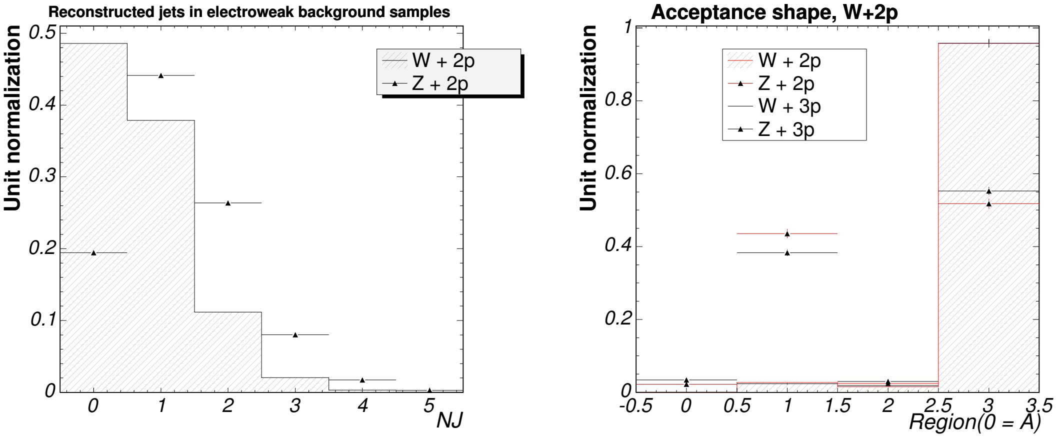

Figure A.3: Left: Comparison of accepted event fraction vs. number of *reconstructed* jets for $W^{\pm} + 2p$ and $Z^0 + 2p$ Monte Carlo events passing all analysis cuts. Note that despite the Z^0 veto cut, the second electron in Z^0 events increases the average number of jets in each event. Right: W backgrounds and Z^0 backgrounds (triangles) have different distributions in the $\not{E}_T$ *vs.* isolation plane, but these distributions are not strongly correlated to the number of partons generated.

W/Z ratio is unchanged, since all such events will be grouped together in the prompt template[3].

If we assume $\sigma_{3p}/\sigma_{2p} = 0.27$ for both processes, these backgrounds would change the effective W/Z ratio to 9.29. We adjust the constraint in Equation A.2 accordingly and recalculate the backgrounds, neglecting any difference in acceptances for the four kinematic regions in the 2- and 3-parton backgrounds. As documented in Table A.1 the effect is very slight, and can be safely ignored.

---

[3] There would also be no effect if Z and W events had the same distribution over the $\not{E}_T$ *vs.* Isol plane, because in this case the dependence of the cross-section calculation on the W/Z ratio would vanish. The second plot of Figure A.3 shows that this is not the case.

	Fraction before background correction	Fraction after correction
Signal	0.769	0.770
Prompt	0.183	0.182
QCD	0.038	0.037
Tau	0.011	0.011

Table A.1: Effect on signal sample composition of rescaling the W/Z ratio constraint to account for backgrounds from $W^{\pm}/Z^{0}+2$ partons.

Appendix B

The conversion background

To estimate the conversion contamination of our pre-tag sample, we must know the inefficiency of the conversion veto described in Section 5.2.3. This is simply the conversion finding algorithm's inefficiency [59]. We must also measure the b-jet tagging rate in conversion events, to determine the number of tagged conversion events we expect in the signal sample. These measurements are discussed below.

B.1 Efficiency of the conversion finder

The conversion finding efficiency was measured to be 73.0 ±0.7% in an earlier version of the offline software (release `4.11.1`). This measurement used a low p_T electron sample [59]. For our measurement, we constructed a 208.2 pb^{-1} sample of high-p_T electrons, including conversion candidates, from the same trigger stream used to select signal events. The cuts used to define this sample are listed in Table B.1: except for the conversion selection, they are the same electron identification cuts used in the mean lifetime measurement. We can repeat the calculation of e_{conv} in this sample, which better reflects our signal sample. We use the same method to calculate the efficiency as previous authors [59].

Electron E_T	$\geq$ 20 GeV
Track p_T	$\geq$ 10 GeV/c
Isolation fraction	$\leq$ 0.1
$E_{\text{cluster}}/P_{\text{track}}$ ($p_T <$ 50 GeV/c)	$\leq$ 2.0 c
$E_{\text{cluster}}/P_{\text{track}}$ ($p_T \geq$ 50 GeV/c)	no requirement
$E_{\text{hadronic cal.}}/E_{\text{CEM}}$	$\leq 0.055 + \frac{0.00045\text{GeV}}{E}$
$q * \delta X$	$<$ 1.5 cm and $>$ -3.0 cm
$\lvert\delta Z\rvert$	$<$ 3.0 cm
χ^2_{strip}	$<$ 10
$Lshr_{\text{track}}$	$<$ 0.2
"fiducial"	($\lvert X_{\text{CES}}\rvert <$ 21 cm, 9 $< \lvert Z_{\text{CES}}\rvert <$ 230 cm, tower $\neq$ 9)
Separation (sep)	$<$ 0.2 cm
$\delta \cot\theta$	$<$ 0.04

Table B.1: Conversion electron identification criteria. The electron identification cuts are the same as those in Table 5.1. The conversion identification cuts are described in Section 4.1.4.

We do not know the fraction of electrons in the original sample that are conversions, so we use another selector, a silicon hit cut ($N_{\text{Si hits}} = 0$), to constrain the sample. This cut should be more efficient for conversions than other electrons because conversion tracks often begin outside of the silicon detector, or between the barrels where the material density is high. We only need to know the *over-efficiency* of this silicon hit cut, which should be related to the generic silicon tracking efficiency ϵ^{SI} as $1 - \epsilon^{SI}$. We measure $\epsilon^{SI} = 0.844 \pm 0.002$ in a sample of generic tracks fiducial to the CES.

We can then write

$$\epsilon = \frac{N_{\text{conv;SI}} - \epsilon^{SI} N_{\text{conv}}}{N_{\text{ele;SI}} - \epsilon^{SI} * N_{\text{ele}}} \tag{B.1}$$

This method of measuring the efficiency uses the fraction of tracks with no silicon hits in an estimate of the total number of conversions, but our signal sample includes a $N_{\text{Si hits}} \geq 3$ cut. Hence we first measure the efficiency for generic electron tracks (with no $N_{\text{Si hits}}$ requirement), and then use Monte Carlo "truth" information to determine the inefficiency for tracks with ≥ 3 axial silicon hits. Using the numbers in Table B.2 we find $e_{\text{conv}} = 0.70 \pm 0.01$.

Assuming the ratio of the overall conversion finding efficiency to the efficiency for tracks with silicon hits is well modeled in Monte Carlo, $N_{\text{missed}} = N_{\text{found}} \times$ (0.664 ±0.050).

We must still extrapolate N_{found} in the 208.2 pb^{-1} inclusive electron strip to the full 318.5pb^{-1} dataset. Since 20 conversions with silicon hits are found in this subsample, 1.9 ±0.1 of which are expected to be missed "tridents," (18.1 ±4.5) × (0.664 ±0.050)(318.5/208.2) = 18.4 ±5 conversions are anticipated before tagging.

Sample	ϵ^{SI}	N_e	N_e^{SI}	N_C	N_C^{SI}	e
MC truth	0.886 ±0.009	5843	1148	5877	1181	0.882 ±0.004
ele data	0.844 ±0.002	609387	315369	253931	74172	0.704 ±0.004

Table B.2: Input data for the calculation of conversion finding efficiency for all electrons in `etlp0d` and `jqcd0e`. The formula is explained in [59].

N_{jets}	Region A	Region B	Region C	Region D
0	4052	10605	157	2198
1	7635	8237	195	372
2	944	757	53	79
3	129	100	15	15
4	17	12	3	4
5	1	0	0	1

Table B.3: Number of conversions with 3 or more axial silicon hits found in each kinematic region, using a 208.2 pb^{-1} subsample of the inclusive high-p_T electron data.

B.2 Tagged conversion events

We can also measure the probability to tag a conversion event using the identified conversion sample. By requiring that conversions be separated from taggable jets by $\Delta R > 0.4$, we ensure that the conversion-finding does not bias the tag probability.

We require the same event-level cuts as the $t\bar{t}$ signal region, but relax the silicon hit requirement, and invert the conversion veto and the missing E_T requirement. Although the inverted conversion veto excludes our $t\bar{t}$ candidate events, we do not use the high missing E_T region for two reasons. First, the low $\not\!\!E_T$ region has better statistics. More importantly, $t\bar{t}$ events with a trident misidentified as a conversion can artificially raise our estimate of the conversion background event tag rate in this region. In the low $\not\!\!E_T$ sample, there are 851 conversion candidates; 54 events are tagged. Our estimate of the tagging rate is thus 6.34 ±0.08 %.

B.2.1 Systematic errors

The most significant assumptions employed above in deriving the conversion background multiplicity are our reliance on the Monte Carlo to describe the correlation of silicon hit finding and conversion tagging, and our use of the low $\not\!\!E_T$ sideband to describe the tag rate of conversion events with high $\not\!\!E_T$.

Heavy flavor jets can generate missing transverse energy in semi-leptonic decays. By using the low $\not\!\!E_T$ sideband to model the conversion event b-tagging rate, we may be biased against heavy flavor events. We can compare our tag rate estimate to the conversion event tag probability in the signal region. If we calculate the conversion tagging rate in the high $\not\!\!E_T$ events, attempting to correct the b-tagging bias by subtracting the anticipated number of $t\bar{t}$ events which would have been misidentified as conversions in 208.2 pb$^-1$, we derive an estimated tag rate of 7.08 %. We use the difference between this estimate and our value, 6.34, as a measure of the possible bias due to event $\not\!\!E_T$.

Appendix C

First hadron collider measurement of τ_τ

The τ lepton, like top, can decay to isolated electrons and muons. However, the τ has a lifetime which should be observable at CDF. As a sensitivity study and a proof of the efficacy of our lifetime template fit, we apply the procedure used to measure the top mean lifetime to a sample of $\tau \to \mu\nu_\tau\nu_\mu$ decays from $Z^0/\gamma^* \to \tau_h\tau_\mu$ events.

We extract signal events from the `TAU_CMUP` and `TAU_CMX` datasets described in Section 3.2.6. Signal Monte Carlo described in Section 4.2.1 is used to refine the event selection and to determine kinematic templates for τ decays. The d_0 templates are then generated for τ lifetimes in the range [0 fs, 1.7 ps], by combining the kinematics of a simulated leptonic τ decay with a proper lifetime chosen from an exponential decay distribution. As for the top mean lifetime analysis, the "true" template d_0 is smeared with a detector resolution function g which is determined from tracks in $Z^0 \to \mu\bar{\mu}$ decays.

Reconstruction parameter	Cut applied
CES cluster E_{min}	0.25 GeV
CES cluster χ^2_{max}	100
π^0 minimum E_{EM}	0.25 GeV
calorimeter seed E_T	>10 GeV
calorimeter shoulder E_T	<1 GeV
N_{towers}	6
Tau cone size	0.4
$(p_T)_{\text{seed track}}$	>4.5 GeV/c
$\eta_{\text{seed track}}$	<1
$(p_T)_{\text{shoulder track}}$	<1GeV/c
$E_T(\pi^0)$	0.5

Table C.1: Hadronic τ reconstruction parameters. The π^0 E_T threshold is not used in cuts, and is lowered to 0.25 GeV to calculate the τ π^0 isolation.

The signal templates are added to background templates described below, with loosely constrained relative normalizations. The fraction of signal events and the lifetime of the signal are then simultaneously fit using an unbinned likelihood procedure.

C.1 Event selection

Events from the datasets described in Section 3.2.6 are processed using production release `5.3`, and reprocessed in offline software release `5.3.3_nt` to refit tracks and reconstruct the hadronically decaying τ. The τ reconstruction parameters are listed in Table C.1.

Data and Monte Carlo events are required to satisfy the same selection requirements. After offline reconstruction, trigger requirements are imposed on all samples to ensure uniformity between data and Monte Carlo samples. Each event must contain a muon candidate with transverse momentum exceeding 10 GeV and a hadronic τ can-

Fiducial:	$p_T > 10$ GeV/c $\lvert z_0 \rvert < 60$ cm (CMU,CMP) $\Delta_x <$ (15,20) cm or CMX $\Delta_x < 30$ cm COT exit radius > 137 cm
Good:	5 hits ×3+3 layer track (CMU,CMP) $\Delta_x <$ (3.0,5.0) cm or CMX $\Delta_x < 6.0$ cm Track COT χ^2 probability $> 10^{-8}$ Track Isolation $I_{\text{track}} < 1$ GeV

Table C.2: Muon quality cuts on the `TAU_MUON` samples, used for the τ lifetime analysis.

didate with corrected visible transverse momentum exceeding 15 GeV. The hadronic τ must contain an isolated seed track, where isolation is determined as in the Level 3 trigger[1].

In fiducial, trigger-confirmed events, both the hadronic τ and the isolated lepton must pass further identification cuts, have opposite electric charges, and be separated by a distance of at least 0.7 radians in $\eta - \phi$ space. The muon identification requirements are listed in Table C.2 and the hadronic τ identification requirements can be found in Table C.3. The final event selection is listed in Table C.4[2].

For events passing all other selection requirements, the track isolation of the muon candidate determines whether the event is considered signal or QCD background. This "strict" sideband is used to calculate the residual background in the signal region. By removing the τ isolation requirement, lowering the leptonic tau p_T cut

---

[1] The L3 algorithm requires that the p_T of any track within a 10 to 30 degree annulus around the seed track be less than 1.5 GeV. Tracks with z_0 greater than 15 cm from the seed track z_0 are not considered.

[2] If the background d_0 shapes can be measured for QCD events over the entire (p_T^τ, m_T) plane, these cuts can be optimized in two dimensions to dramatically increase the acceptance [82].

Fiducial seed track:	$p_T > 10$ GeV/c COT exit radius > 137 cm $9 < \lvert z_{\mathrm{CES}}\rvert < 230$ cm L3 Isolated
Fiducial cluster:	Seed tower $E_T > 10$ GeV Visible $p_T > 15$ GeV/c $\lvert \eta_{\mathrm{det}}\rvert < 1$
Good Tau object:	No isolation tracks in cone $I_{\pi^0} < 0.6$ GeV/c $E_{\mathrm{Had}} > 0.1\ p_{\mathrm{seed}}$ $M_{\mathrm{vis}} < 2.0$ GeV/c^2 $M_{\mathrm{trk}} < 1.8$ GeV/c^2 veto: electrons, muons, stubs 1 or 3 tracks in cone

Table C.3: Hadronic τ quality cuts on the `TAU_MUON` samples, used for the τ lifetime analysis.

muon + $\not\!\!E_T$:	$p_T > 25$ GeV/c $m_T < 25$ GeV/c^2
muon + τ_h	opposite charge

Table C.4: Event-level cuts on the `TAU_MUON` samples, used for the τ lifetime analysis.

by 5 GeV/c, and including wrong-sign events, we make the QCD background sample large enough to accurately characterize the impact parameters of fake muons and muons from semi-leptonic bottom and charm decays.

After all cuts, 98 events remain in the signal sample and 27 events remain in the strict QCD background sample.

C.2 Sample composition

$Z^0 \to \tau\tau$ signal	73.2 ±19.1
Z^0 and $W^\pm$ prompt muons	6.55 ±2.08
heavy and light flavor QCD muons	4.5 ±0.98

Table C.5: Sample composition describing the origin of muons in the signal region for the τ lifetime analysis. Errors include statistical and luminosity uncertainties.

We expect 84.25 ± 20 muon events in the sample, 13.1 ± 3.1 % of which are background events. Table C.5 describes the expected sample composition after all cuts, which is derived in this section.

C.2.1 Expected backgrounds

The background estimates are primarily derived from Monte Carlo and checked using selected data events. The backgrounds considered are QCD jet production, $Z^0/\gamma^* \to \mu\bar{\mu}$ and $W^\pm \to \mu\bar{\nu_\mu}$. We also check that cosmic ray muon events, which have a flat d_0 distribution that would bias the lifetime fit, are efficiently removed from the data. We neglect smaller backgrounds to $Z^0/\gamma^* \to \tau_\mu\tau_h$, such as $t\bar{t}$ production.

	CMUP	CMX
σ	2768±66 pb	
$\mathcal{L}$	317±19	304±18
A	0.00247±0.00005	
ϵ_μ	0.700±0.009	0.198±0.008
ϵ_τ	0.111±0.007	0.128±0.014
$\epsilon_{\text{event cuts}}$	0.0240±0.011	0.0294±0.0204
ϵ_{L1+L2}	.880±.022	.959±.090
SI track	.926±.031	.973±.026
N_{expected}	3.29 ±1.69	1.45±1.04
N_{scaled}	4.50 ±2.03	

Table C.6: Efficiencies for events in the `wewk6m` sample. N_{scaled} represents the expectation after the instantaneous luminosity correction is applied. Because of differences in actual and simulated run numbers we take the efficiency of silicon tracking from muons in the `etlp0d` dataset.

$W^\pm \to \mu\nu$ background

Fiducial acceptance The raw acceptance for events from the W background channel is $\frac{N_{\text{fiducial}}}{N_{\text{simulated}}} = (2.47 \pm 0.05) \times 10^{-3}$, as shown in Table C.6. We should correct this acceptance for a luminosity bias, since the fiducial cuts include the Level 3 requirement of an isolated track. While the Monte Carlo sample `wewk6m` includes multiple collisions, it only grossly represents the luminosity of the data because the simulated run range ends before run 160000. We measure the Monte Carlo acceptance as a function of N_{vertices}, the number of class 12 z vertices in the event, and use this dependence in calculating an average acceptance weighted to reflect the observed N_{vertices} in the data. The ratio of the re-weighted acceptance to the raw acceptance is 0.986 ±0.021.

Trigger efficiencies The Level 1 and Level 2 trigger efficiencies have been measured for isolated muons passing our fiducial requirements [83]. We use these efficiencies in Table C.6. The Level 3 trigger cuts are confirmed in our event selection, and we neglect any difference between trigger and offline reconstruction efficiencies in this acceptance calculation. Other studies of the Level 3 isolated track trigger [84] using similar seed track cuts for τ candidates indicate that its average efficiency is 0.989±.007.

Selection efficiency The fraction $\frac{N_{\text{accepted}}}{N_{\text{fiducial}}} = .00261 \pm .00098$ represents the raw selection efficiency for $W^{\pm}$ events, before silicon track requirements. Because multiple interactions can affect the τ candidate and the muon selection efficiencies, this fraction should also be corrected for luminosity effects. We again apply a scale factor by measuring the ratio of accepted to fiducial events as a function of N_{vertices} in the Monte Carlo, and re-weighting the Monte Carlo events to reflect the signal dataset's primary vertex distribution. The muon identification efficiency loss is compensated by a higher τ fake rate, so the ratio of the resulting efficiency to the raw efficiency is 0.962 ±0.094.

Comparison of estimate with data Many aspects of the jet-to-tau fake rate might be inadequately simulated for this background calculation. To check that the number of Monte Carlo "fiducial" τ candidates are reasonable, we compare the Monte Carlo W yield in the region of high missing E_T to the data in Figure C.1.

$Z^0/\gamma^* \rightarrow \mu\bar{\mu}$ background

Fiducial acceptance. The raw acceptance for events from the Z^0 background channel is $\frac{N_{\text{fiducial}}}{N_{\text{simulated}}} = (6.47 \pm 0.03) \times 10^{-3}$, as shown in Table C.7. We correct this

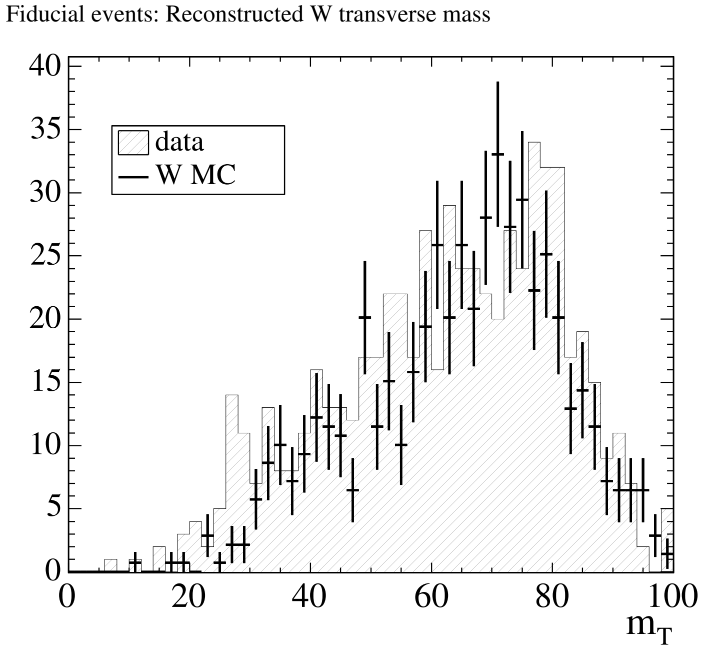

Figure C.1: $W^\pm$ transverse mass distribution for fiducial events in data and $W^\pm \rightarrow \mu\bar{\nu}_\mu$ Monte Carlo (normalized to the prediction.)

	CMUP	CMX
σ	467 ±13	
$\mathcal{L}$	317±19	304±18
A	0.00647±0.00005	
ϵ_μ	0.648±0.00338	0.254±0.003
ϵ_τ	0.0708±0.0022	0.0729±0.0037
$\epsilon_{\text{event cuts}}$	0.0328±0.0059	0.070±0.013
ϵ_{L1+L2}	.880±.022	.959±.090
SI track	.926±.031	.973±.026
N_{expected}	1.02±.319	1.12±.247
N_{scaled}	2.05 ±.44	

Table C.7: Efficiency calculation in the `zewk6m` background Monte Carlo sample.

acceptance in the same way as for W background events. The raw efficiency must be scaled down by 0.986 ±0.067 to account for the difference in luminosities.

Trigger efficiencies. Again, Level 3 trigger cuts are confirmed in our event selection, so we have accounted for the L3 efficiency. Because we reject events in all samples when more than one reconstructed muon passes fiducial requirements, the same trigger efficiency applies to this sample as to the $W^{\pm}$ background and $Z \rightarrow \tau\tau$ signal.

Selection efficiency. The raw selection efficiency for Z events is $(2.8 \pm 0.3) \times 10^{-3}$. We repeat the calculation performed for W Monte Carlo to derive a combined luminosity scale factor for τ and μ identification in Z^0 simulated events, 0.974 ±0.042.

Comparison of estimate with data. We remove the veto on a second fiducial muon to compare the predicted distribution of the dimuon mass in Z^0 events to the data. When the fiducial scale factor is applied, the ratio of background-subtracted events in the region $86 < m_Z < 106$ is 78.1% ±7.3% where the error includes statistical and luminosity uncertainties[3].

QCD background

The QCD background is derived from the data, based on the different distribution of muon track isolation in QCD and signal or electroweak background events. Figure C.3 shows the muon track isolation for data in the signal region, in the QCD-enhanced region of muon $p_T + \not{E}_T < 20$, and in signal Monte Carlo. 27 events are observed

---

[3] We add a 1.6% systematic uncertainty to the background because of this difference.

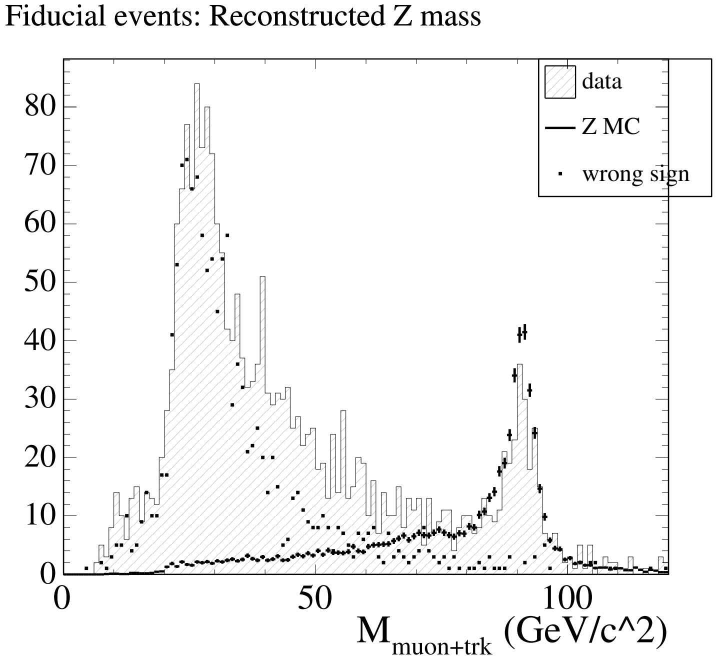

Figure C.2: Muon + track mass distribution for fiducial events in data and Monte Carlo (normalized to the prediction.)

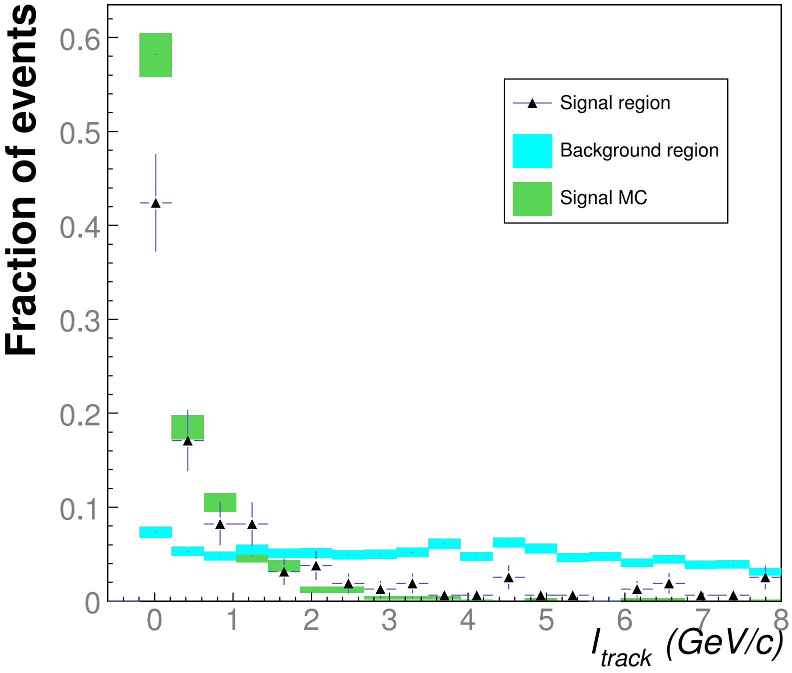

Figure C.3: Comparison of muon track isolation for simulated signal events (green), data in the kinematic region dominated by QCD events (blue), and data in the signal region (triangles). These plots are normalized to equal area.

in the strict QCD sideband (2 GeV $< I_{\text{track}} <$ 8GeV). Modeling the QCD isolation shape as a flat distribution, we expect 4.50 ±0.98 QCD events in the signal region[4].

Cosmic ray background.

We check that cosmic ray contamination in the sample is small enough to be neglected. Removing the cosmic ray veto, we fit the tails $|d_0| > 2$ mm of the muon impact parameter distribution for fiducial events. The fits are shown in Figure C.4. A flat component consistent with cosmic ray muons can be discerned, making up 0.93%

---

[4] We have added an additional 10% systematic to the statistical uncertainty to account for the assumption of flatness.

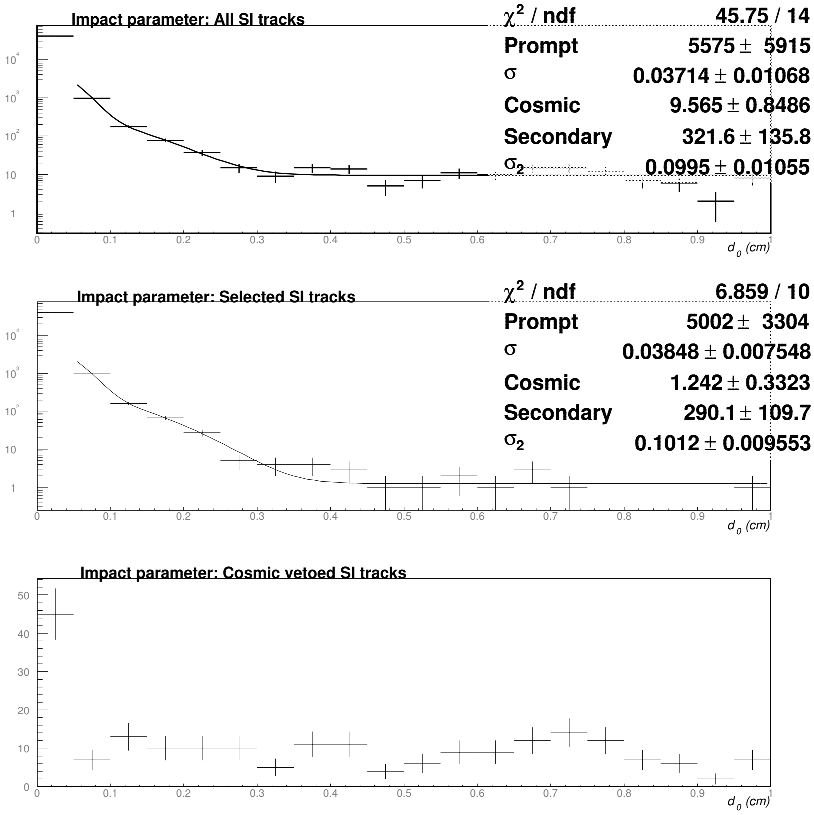

Figure C.4: Determination of cosmic ray contamination in the fiducial `etlp0d` sample. The upper plot shows the impact parameter of all silicon tracks, the center shows the distribution for tracks in events passing the veto, and the bottom plot shows the removed events.

of all muons. An estimated 23.98 cosmic muons will pass the loose $|d_0|$ cut on our sample. After applying the cosmic ray veto, an estimated 1.24 ±0.33 remain. While no cosmic-flagged events pass all other sample cuts, we can use the ratio $\frac{N_{\text{passed}}}{N_{\text{fiducial}}} = (2.2 \pm 0.3) \times 10^{-3}$ from Z Monte Carlo events as a rough estimate of the efficiency for cosmic ray muon events. If a fiducial cosmic ray event has the same probability as a fiducial Z^0 event to be accepted, less than .003 cosmic rays are expected in the final sample.

	CMUP	CMX
σ	467 ±13	
$\mathcal{L}$	317±19	304 ±18
A	0.00295 ±0.00004	
ϵ_μ	0.776 ±0.007	0.089 ±0.004
ϵ_τ	0.616 ±0.008	0.591 ±0.026
$\epsilon_{\text{event cuts}}$	0.452 ±0.0112	0.391 ±0.0333
ϵ_{L1+L2}	.880±.022	.959±.090
SI track	.926±.031	.973±.026
N_{expected}	76.9±19.7	8.02±1.37
N_{scaled}	73.2 ±19.9	

Table C.8: Efficiency calculation in the `zewk8t` signal Monte Carlo sample.

C.2.2 Signal yield

Fiducial acceptance. The raw acceptance for signal events is $\frac{N_{\text{fiducial}}}{N_{\text{simulated}}} = 2.95 \pm .04 \times 10^{-3}$, as shown in Table C.7. We correct this acceptance in the same way as for background events. Like the $W^\pm$ sample, the signal MC sample used is still incomplete and hence the range of runs is much smaller than the run range of the data. The scale factor accounting for this effect on the isolated seed cut is 0.926 ±0.014.

Trigger efficiencies. The Level 1 and Level 2 trigger efficiencies are applied as for $W^\pm$ and $Z^0 \to \mu\mu$ background events. The Level 3 trigger efficiency is taken to be 1.0 for fiducial events.

Selection efficiency. The raw signal selection efficiency is 0.237 ± 0.007. The luminosity scale factor for τ and μ identification is 0.931 ±0.032 in this sample. The full acceptance × efficiency calculation is summarized in Table C.8.

In the Appendix, several distributions sensitive to the $Z^0 \to \tau\tau$ component are plotted from the signal region.

C.3 Template generation

We construct the impact parameter of muons from simulated τ decays in the same way as the lepton d_0 in simulated top events. The calculation is described in Section 7.2.

C.3.1 Detector resolution

The detector resolution is incorporated by smearing the true d_0 distribution with the impact parameters of muons from Z^0 decays. We find $Z^0 \to \mu\mu$ decays in events from the high-p_T muon sample `bhmu0d`, and use the d_0 of any muon satisfying the muon identification cuts in Table C.2 in the parent distribution. The impact parameters of the identified Z^0 decay products are plotted in Figure C.5. The data is well modeled by a single Gaussian distribution, which is used in constructing the prompt background template.

In Figure C.6 we compare the impact parameters of silicon tracks from $Z^0/\gamma^* \to \tau\bar{\tau}$ muons in Monte Carlo to the generated d_0 distribution using a τ lifetime $c\tau = 87\mu$m and the measurement resolution encoded in the impact parameter distribution of muons in Z^0 and $W^\pm$ Monte Carlo.

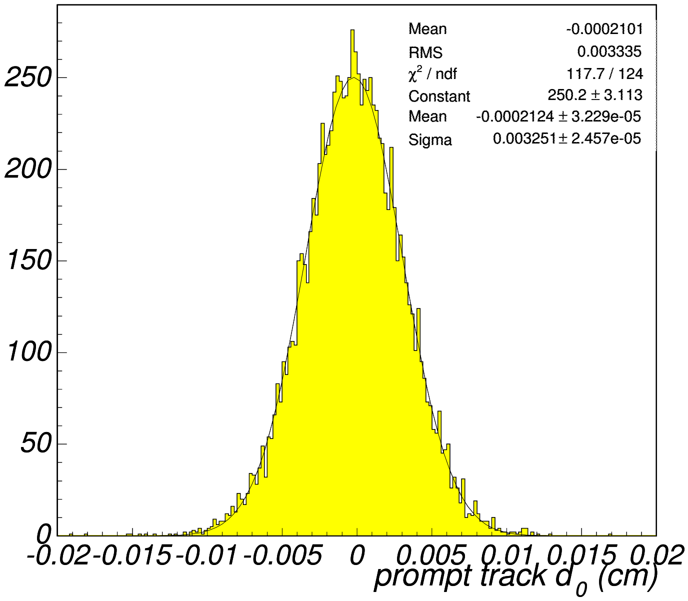

Figure C.5: Impact parameter resolution template for the τ mean lifetime analysis.

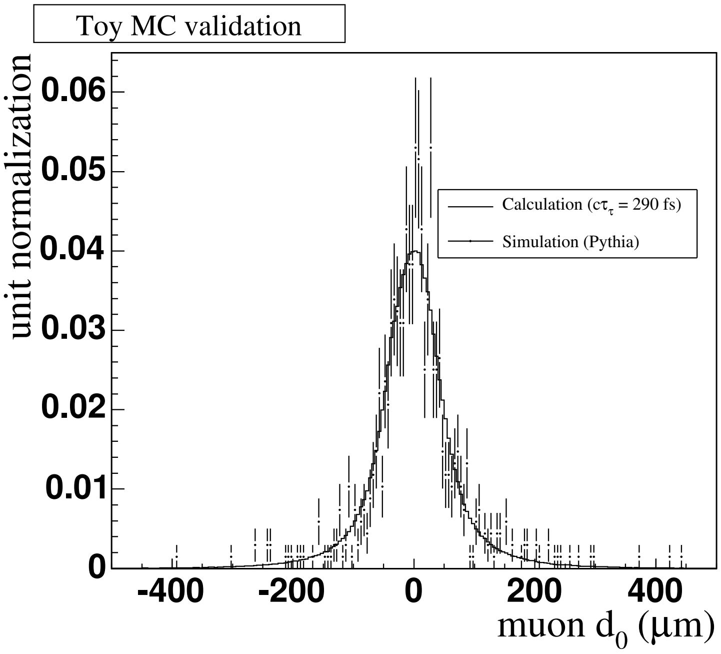

Figure C.6: Comparison of the 291 fs template (generated from Pythia $Z^0 \to \tau\tau$ Monte Carlo kinematics) and the d_0 distribution created by the full detector simulation for the same events.

C.3.2 Background templates

The background templates comprise two components, prompt and displaced backgrounds. All of the electroweak backgrounds are modeled by normalizing the d_0 distribution derived from $Z^0/\gamma^* \to \tau\bar{\tau}$ data to the total number of expected electroweak events. The QCD background is a mixture of prompt and displaced tracks, which is modeled with the following procedure.

We utilize the QCD-dominated "isolation sideband," those events passing all analysis cuts except the track isolation cut on the muon. Besides a small component of signal and electroweak events, this region contains muon tracks from heavy-flavor quark decays, pion and kaon decays, Drell-Yan events, and hadronic fakes. We assume that these latter processes contribute to the events passing and failing the isolation cut in similar *relative* proportion. Specifically, we assume that the mixed sample composition does not generate a correlation between muon track isolation and the muon's impact parameter.

To check that the muon track isolation is not appreciably correlated to d_0 in QCD background events, we consider the "kinematic sideband", those events failing the $p_T^{\text{muon}} + \not{E}_T > 25$ cut. For these events, we compare track isolation distributions for muons passing a tight d_0 cut, and for muons failing a loose d_0 cut, which are mostly heavy flavor. The comparison is shown in Figure C.7. Since the shape of the track isolation distribution is unchanged (the slight excess of prompt muons over displaced muons in the $I_{\text{track}} = 0$ bin can be explained by residual electroweak events), we conclude that the isolation sideband is an appropriate sample for measuring the QCD background d_0 template.

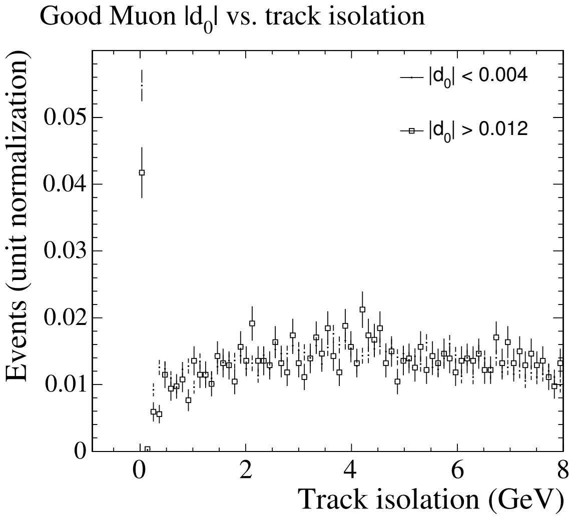

Figure C.7: Study of correlations between muon track isolation and muon impact parameter in QCD data events.

The isolation sideband has few events, so we slightly loosen the $p_T^{\text{muon}} + \not{E}_T > 25$ cut, remove the tau π^0 isolation and opposite-sign requirements, and *fit* the d_0 distribution to generate a smooth, well-modeled QCD template. The data is fit to a narrow Gaussian plus the sum of two exponentials.

The contributions to the overall background template and the fit to the QCD component are displayed in Figure C.8.

C.4 Template fit

We have described a procedure for generating an array of signal templates $T_{c\tau}(d_0)$ and a single background template $T_B(d_0)$. We use them to fit the data for two unknown parameters: the amount of background, and the lifetime of the signal. From the event yield study described in Section C.2, we predict a total background fraction

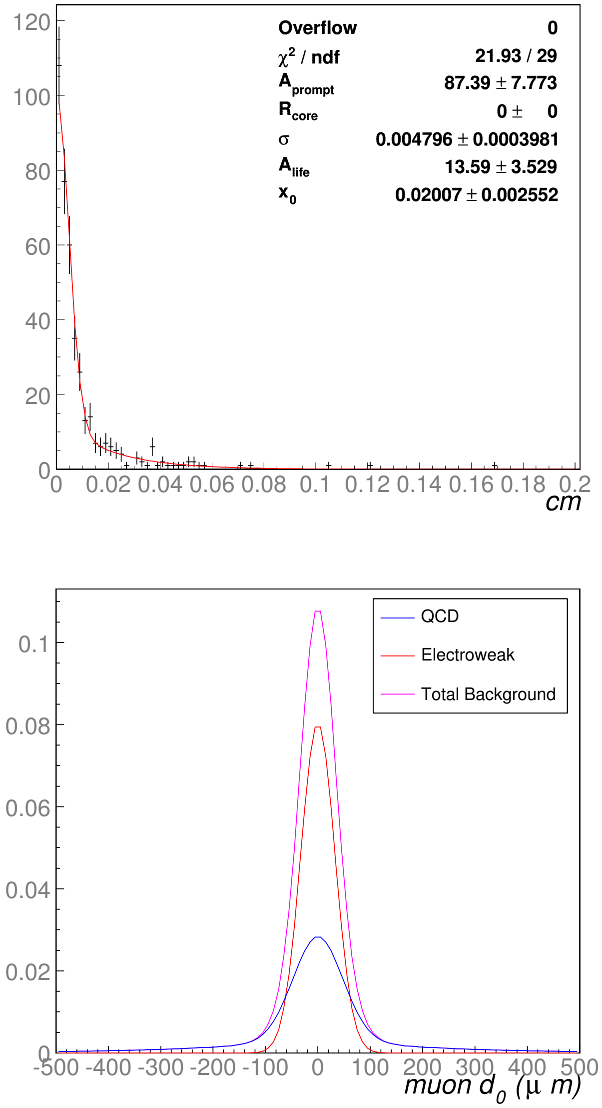

Figure C.8: Construction of the background template used in fitting $c\tau$. Top: QCD fit. Bottom: total background template.

$(f_B)_0$ and apply it to the fit as a Gaussian constraint. Hence our method numerically minimizes $-0.5 \ln \mathcal{L}$ where $\mathcal{L} = e^{(f_B-(f_B)_0)^2/2\sigma_B^2)} * \Pi_{trks}\left[(1-f_B)T_{c\tau}(d_0) + f_B T_B(d_0)\right]$ as a function of $c\tau$ and f_B.

C.4.1 Template bias

Pseudoexperiment studies reveal the sensitivity and bias of the template method. We generate 98 events from a parent template constructed from a signal shape with τ lifetime τ_{pseudo} and a background shape normalized to f_B. The first test determines the resolution and bias in the fitting procedure when $(f_B)_0 = (f_B)_{pseudo}$. $c\tau_{\text{fit}}$ is plotted in Figure C.9 against $c\tau_{\text{pseudo}}$. The second (Figure C.10) determines the bias in the fitting procedure as a function of $(f_B)_0 = (f_B)_{pseudo}$. We conclude that when the background is well understood, and less than about 50%, the lifetime measurement is unbiased. The expected resolution in these ideal conditions is 17 μm.

C.4.2 Errors from template fitting

Background normalization constraint error

The background fraction fit is dominated by the prior constraint. Entirely removing the constraint biases the average fitted lifetime by $+5.4$ μm, and increases the RMS by a factor of 1.7, while even a gentle constraint essentially removes this bias. Hence, we consider the error incurred by constraining the background fraction to an incorrect value. In 800 pseudoexperiments using the expected lifetime and background, when we constrain to a background fraction incorrect by $+1\sigma$, the fit background shifts up by 1σ as expected, but the fit lifetime changes by only $+1.5$

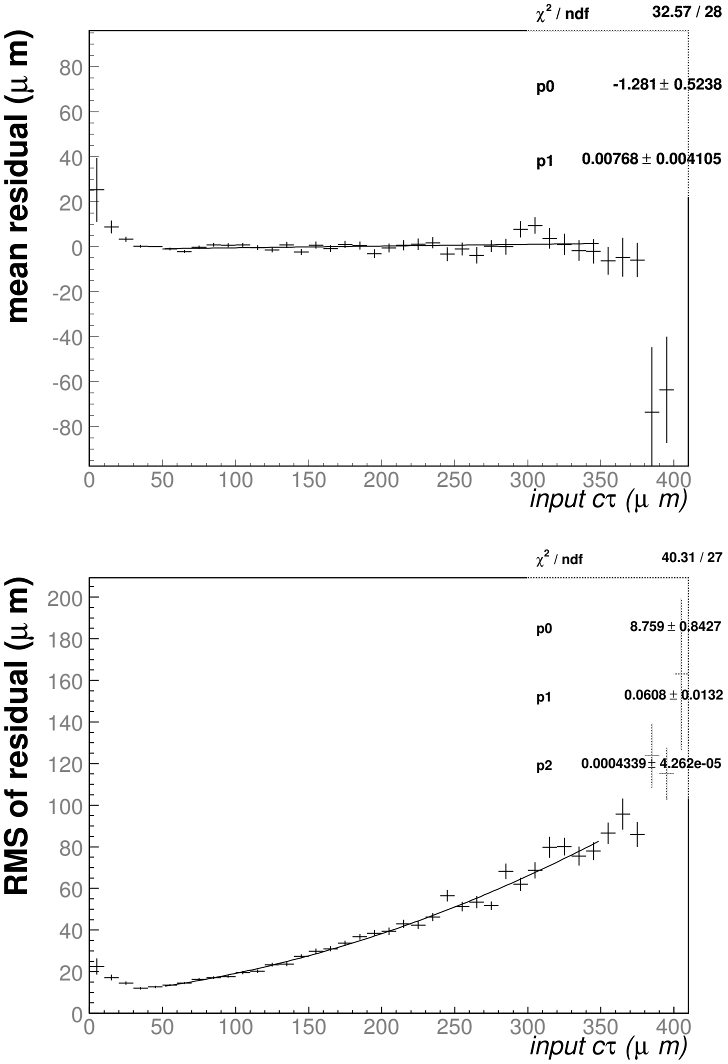

Figure C.9: Pseudoexperiment studies of the $c\tau$ bias and variance from the fitting procedure. The mean and variance of the difference between the generated and fit $c\tau$ are plotted as a function of generated c_τ.

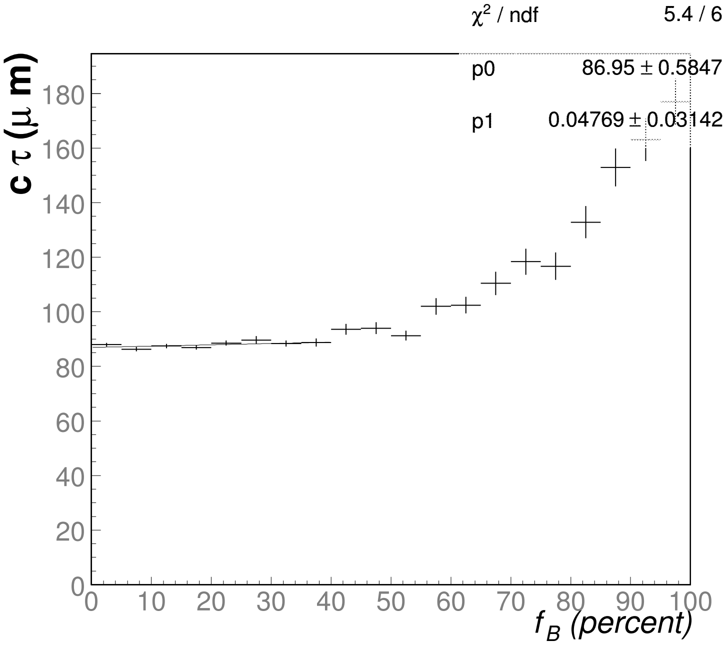

Figure C.10: Pseudoexperiment studies of the $c\tau$ bias as a function of generated f_B. The average $c\tau$ is plotted against f_B.

± 0.9 μm, with unchanged RMS.

C.5 Results

C.5.1 Tau lifetime

The fit returns a τ lifetime of 85.5^{+23}_{-17} μm, where the errors are simply calculated from the shape of the likelihood function. The comparison of the data to the best-fit template is shown in Figure C.11. The variance from the fit matches the expectation from pseudoexperiment studies, so we use this to represent the statistical error. We also incorporate a systematic error from the bias due to the background uncertainty, which is increased by 1.6% (absolute) to account for the Z yield discrepancy. Hence we measure that the τ mean lifetime is 285^{+77}_{-58} fs.

C.5.2 Data-Monte Carlo comparisons

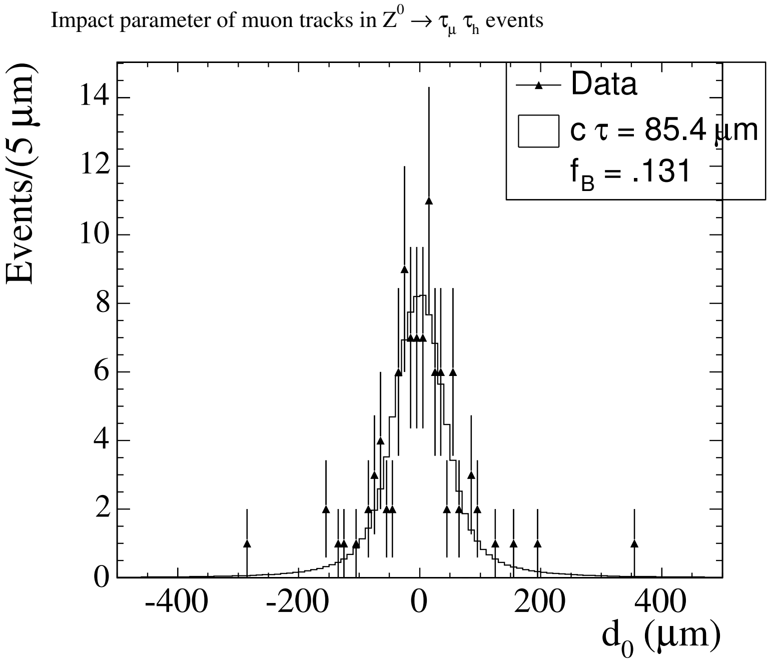

Figure C.11: Comparison of the τ d_0 data to the best-fit template.

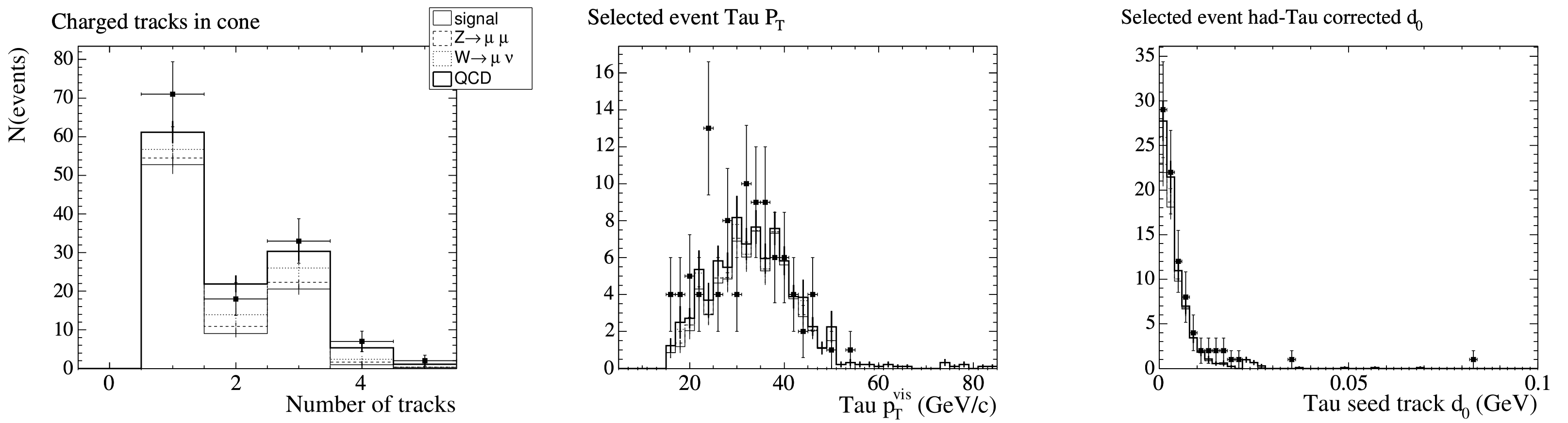

Figure C.12: Comparison of prediction and observation for distributions from the signal region. 1. Tau prongs (opposite sign cut has been removed), 2. tau momentum, 3. Hadronic τ seed track d_0. The legend applies to the three distributions, as well as the distributions in Figure C.13.

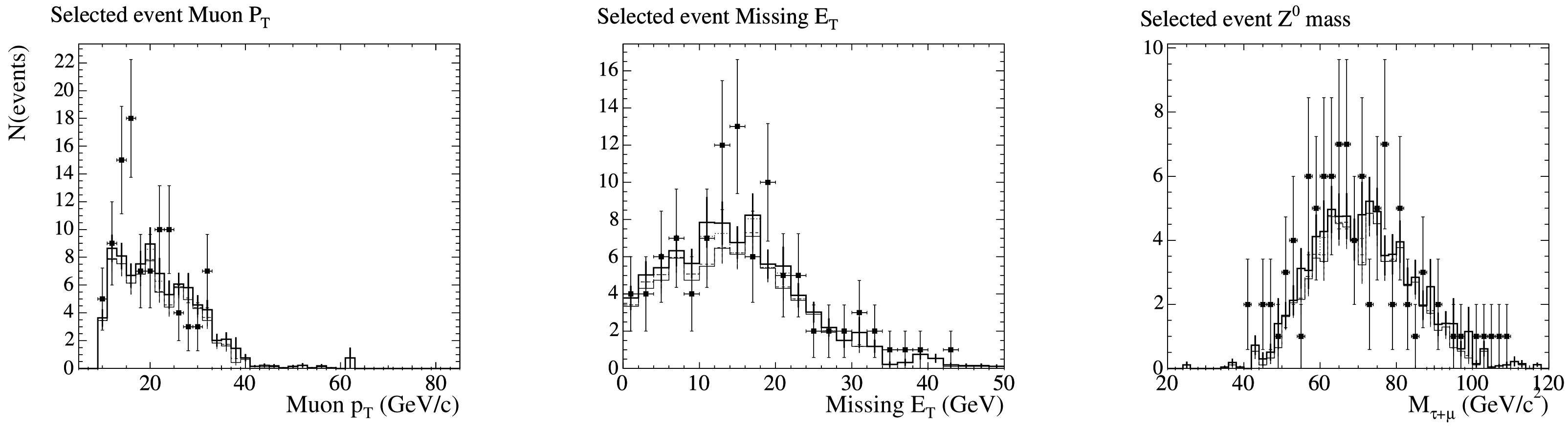

Figure C.13: Comparison of prediction and observation for distributions from the signal region. 1. Muon momentum, 2. missing transverse energy, 3. reconstructed Z^0 mass. The legend in Figure C.12 applies to these figures.

Bibliography

[1] S. L. Glashow, J. Iliopoulos, and L. Maiani. Weak interactions with lepton - hadron symmetry. *Phys. Rev.*, D2:1285–1292, 1970.

[2] J. E. Augustin et al. Discovery of a narrow resonance in e+ e- annihilation. *Phys. Rev. Lett.*, 33:1406–1408, 1974.

[3] S. W. Herb et al. Observation of a dimuon resonance at 9.5-GeV in 400-GeV proton - nucleus collisions. *Phys. Rev. Lett.*, 39:252–255, 1977.

[4] F. Abe et al. Evidence for top quark production in anti-p p collisions at s**(1/2) = 1.8-TeV. *Phys. Rev.*, D50:2966–3026, 1994.

[5] J. Abdallah et al. A precise measurement of the tau lifetime. *Eur. Phys. J.*, C36:283–296, 2004.

[6] David J. Griffiths. *Introduction to Elementary Particles.* WILEY, NEW YORK, USA, 1987.

[7] I.J.R. Aitchison and A.J.G Hey. *Gauge Theories in Particle Physics, 2nd Edition.* IOP Publishing Ltd, 1989.

[8] E. Eichten. Theoretical expectations at collider energies. Based on lectures given at 1985 Theoretical Adv. Study Inst., New Haven, CT, Jun 9 - Jul 5, 1985.

[9] H. L. Lai et al. Global QCD analysis and the CTEQ parton distributions. *Phys. Rev.*, D51:4763–4782, 1995.

[10] J. Pumplin et al. New generation of parton distributions with uncertainties from global QCD analysis. *JHEP*, 07:012, 2002.

[11] Nikolaos Kidonakis and Ramona Vogt. Next-to-next-to-leading order soft-gluon corrections in top quark hadroproduction. *Physical Review D*, 68:114014, 2003.

[12] M. Cacciari, S. Frixione, M. L. Mangano, P. Nason, and G. Ridolfi. The t anti-t cross-section at 1.8-TeV and 1.96-TeV: A study of the systematics due to parton densities and scale dependence. *JHEP*, 04:068, 2004.

[13] The CDF collaboration. Updated combination of CDF top mass results using up to 750 pb^{-1} of data. CDF Public Note # 8222.

[14] Steven Weinberg. A model of leptons. *Phys. Rev. Lett.*, 19(21):1264–1266, Nov 1967.

[15] S. Eidelman et al. Review of Particle Physics. *Physics Letters B*, 592:1+, 2004.

[16] Michael E. Peskin and D. V. Schroeder. *An Introduction to Quantum Field Theory.* Addison-Wesley, Reading, USA, 1995.

[17] The ALEPH, DELPHI, L3, OPAL, SLD Collaborations, the LEP Electroweak Working Group, the SLD Electroweak and Heavy Flavour Groups. Precision Electroweak Measurements on the Z Resonance. 2005.

[18] The Lep W Working Group. Combined preliminary results on the mass and width of the W boson measured by the LEP experiments, 2003.

[19] The Tevatron Electroweak Working Group. Combination of CDF and D0 results on the W-boson width, 2005.

[20] Tevatron Electroweak Working Group. Combination of cdf and d0 results on the mass of the top quark. 2006.

[21] Erik Brubaker. Top quark mass measurements at CDF. 2006.

[22] Makoto Kobayashi and Toshihide Maskawa. CP violation in the renormalizable theory of weak interaction. *Prog. Theor. Phys.*, 49:652–657, 1973.

[23] D. Acosta et al. Measurement of B(t→Wb)/B(t→Wq) at the collider detector at fermilab. *Phys. Rev. Lett.*, 95:102002, 2005.

[24] Ikaros I. Y. Bigi, Yuri L. Dokshitzer, Valery A. Khoze, Johann H. Kuhn, and Peter M. Zerwas. Production and decay properties of ultraheavy quarks. *Phys. Lett.*, B181:157, 1986.

[25] King-Man Cheung. Probing non-standard top couplings using spin-correlation. *Phys. Rev.*, D55:4430–4434, 1997.

[26] Lynne H. Orr, T. Stelzer, and W. James Stirling. Gluon radiation in t anti-t production at the Tevatron p anti-p collider. *Phys. Rev.*, D52:124–132, 1995.

[27] Hitoshi Murayama. Supersymmetry phenomenology, 2000.

[28] Nima Arkani-Hamed and Savas Dimopoulos. Supersymmetric unification without low energy supersymmetry and signatures for fine-tuning at the LHC. *JHEP*, 06:073, 2005.

[29] Manuel Toharia and James D. Wells. Gluino decays with heavier scalar superpartners. *JHEP*, 02:015, 2006.

[30] P. Gambino, G. F. Giudice, and P. Slavich. Gluino decays in split supersymmetry. *Nucl. Phys.*, B726:35–52, 2005.

[31] JoAnne L. Hewett, Ben Lillie, Manuel Masip, and Thomas G. Rizzo. Signatures of long-lived gluinos in split supersymmetry. *JHEP*, 09:070, 2004.

[32] Fermilab Visual Media Services. Graphic arts: Graphics and illustrations – Tevatron drawings. http://www-visualmedia.fnal.gov.

[33] Tevatron Beams Division. Accelerator information: Supertable II. http://www-bd.fnal.gov/SDAMisc/new_supertableII.html.

[34] S. Lai, J. Guimar aes, W. Wagner, P.K. Sinervo, and R. Culbertson. An updated measurement of the beam width at CDF. CDF Internal Note #6492.

[35] Anyes Taffard. Run II cosmic ray tagger. CDF Internal Note #6100.

[36] Christopher S. Hill. Operational experience and performance of the CDFII silicon detector. *Nucl. Instrum. Meth.*, A530:1–6, 2004.

[37] A. Sill. CDF Run II silicon tracking projects. *Nucl. Instrum. Meth.*, A447:1–8, 2000.

[38] Anthony A. Affolder et al. CDF Central Outer Tracker. *Nucl. Instrum. Meth.*, A526:249–299, 2004.

[39] D. Acosta et al. A time-of-flight detector in CDF-II. *Nucl. Instrum. Meth.*, A518:605–608, 2004.

[40] L. Balka et al. The CDF Central Electromagnetic Calorimeter. *Nucl. Instrum. Meth.*, A267:272, 1988.

[41] Tania Moulik. Offline Central PreRadiator reconstruction in RunIIa. CDF Internal Note #6192.

[42] L. Nodulman et al. Central Shower Counter prototype for the Fermilab Collider Detector Facility. *Nucl. Instr. Meth.*, 204:351, 1983.

[43] M. G. Albrow et al. The CDF plug upgrade electromagnetic calorimeter: Test beam results. *Nucl. Instrum. Meth.*, A480:524–546, 2002.

[44] P. de Barbaro et al. CDF end plug hadron calorimeter upgrade: Design, production and quality control results. *IEEE Trans. Nucl. Sci.*, 42:510–517, 1995.

[45] G. Ascoli et al. CDF Central Muon Detector. *Nucl. Instrum. Meth.*, A268:33, 1988.

[46] G. Gomez-Ceballos et al. Event builder and Level 3 at the CDF experiment. *Nucl. Instrum. Meth.*, A518:522–524, 2004.

[47] Yoshio Ishizawa and Jason Nielsen. Trigger efficiencies for high E_T electrons. CDF Internal Note #7401.

[48] V. Martin. High-Pt muon ID cuts and efficiencies for use with 5.3.1 data and 5.3.3 MC. CDF Internal Note #7367.

[49] Jack Cranshaw, Mark Lancaster, Jim Kowalkowski, Paolo Calafiura, Marjorie Shapiro, Dennis Box, and Robert Harris. A calibration database schema for CDF II. CDF Public Note # 5088.

[50] Chris Hays, Peter Tamburello, Ashutosh Kotwal, Peter Wittich, and Rick Snider. The COT pattern recognition algorithm and offline code. CDF Internal Note #6992.

[51] P. Azzi, G. Busetto, P. Gatti, and A. Ribon. Histogram tracking in the COT. CDF Internal Note #5562.

[52] K. Bloom and W.-M. Yao. “Outside-In” silicon tracking at CDF. CDF Internal Note #5991.

[53] B. Flaugher and J.Mueller. A guide to JetClu: The CDF jet cluster algorithm. CDF Internal Note #1814.

[54] Anwar Bhatti and Florencia Canelli. Jet energy corrections at CDF. CDF Internal Note #7543. To be submitted to NIM.

[55] K. Burkett, J. Guimar aes, and S. Rappoccio. First look at SecVtx using event primary vertex finder PrimeVtx. CDF Internal Note #6417.

[56] Daniel Sherman, Sal Rappoccio, and Jo ao Guimarães da Costa. Measurement of the SecVtx mistag asymmetry in 5.3.3. CDF Internal Note #7585.

[57] Jo ao Guimarães da Costa and Salvatore Rappoccio. SecVtx tag matrices for 5.3.3_nt. CDF Internal Note #7326.

[58] Robert G. Wagner. Understanding and using Lshr. CDF Internal Note #6249.

[59] E. Halkiadakis, C. Hays, M. Tecchio, and W. Yao. A conversion removal algorithm for the 2003 winter conferences. CDF Internal Note #6250.

[60] Jim Bellinger, Ken Bloom, W. David Dagenhart, Andreas Korn, Slava Krutelyov, Victoria Martin, and Michael Schmitt. A guide to muon reconstruction for Run 2. CDF Internal Note #5870.

[61] S. Baroiant et al. The CDF-II tau physics program: Triggers, tau ID and preliminary results. 2003.

[62] Torbjorn Sjostrand et al. High-energy-physics event generation with PYTHIA 6.1. *Comput. Phys. Commun.*, 135:238–259, 2001.

[63] G. Corcella, I.G. Knowles, G. Marchesini, S. Moretti, K. Odagiri, P. Richardson, M.H. Seymour, and B.R. Webber. HERWIG 6: An event generator for hadron emission reactions with interfering gluons (including supersymmetric processes). *JHEP*, 01:010, 2001.

[64] Michaelangelo Mangano. ALPGEN, a generator for hard multiparton processes in hadronic collisions. *JHEP*, 307:1, 2003.

[65] R. Brun, R. Hagelberg, M. Hansroul, and J. C. Lassalle. GEANT: Simulation program for particle physics experiments. User guide and reference manual. CERN-DD-78-2-REV.

[66] Aaron Dominguez. Realistic MC. http:// www-cdf.fnal.gov/internal/physics/ joint_physics/docs/ RealMC_update_20Sep2002, CDF Note in preparation.

[67] H. Bachacou, C. Ferretti, J. Nielsen, and W. Yao. Heavy flavor contributions to the SECVTX-tagged W + jets sample. CDF Internal Note #7007.

[68] S. Jadach, Z. Was, R. Decker, and Johann H. Kuhn. The tau decay library TAUOLA: Version 2.4. *Comput. Phys. Commun.*, 76:361–380, 1993.

[69] Monica D'Onofrio, Regis Lefevre, Mario Martinez, and Oriol Salto. Good Run List page. http://www-cdf.fnal.gov/internal/dqm/goodrun/good.html.

[70] D. Allspach, D. Ambrose, M. Binkley, K. Burkett, R. Kephart, R. Madrak, T. Miao, A. Mukherjee, R. Roser, and R. L. Wagner. Aging in the large CDF axial drift chamber. CDF Internal Note #7406.

[71] Willis Sakumoto. Event $|z_{\mathrm{vtx}}| \leq 60$ cm cut acceptance for Run II. CDF Internal Note #7935.

[72] C. Hill, J. Incandela, , and C. Mills. Electron identification in offline release 5.3. CDF Internal Note #7309.

[73] A. Holloway, D. Sherman, S. Rappoccio, J. Guimar aes da Costa, and S. Grinstein. SecVtx tagging scale factor for 5.3.3 analyses. CDF Internal Note #7445.

[74] T. Wright. SecVtx b-tag efficiency using muon transverse momentum. CDF Internal Note #7448.

[75] H. Bachacou, P. Lujan, J. Nielsen, W.Yao, A. Holloway, D. Sherman, S. Rappoccio, J. Guimar aes da Costa, S. Grinstein, T. Wright, and S. Levy. Combining the SecVtx b-tagging scale factors for 5.3.3 analyses. CDF Internal Note #7480.

[76] Andrew Foland, Melissa Franklin, Joao Guimaraes Da Costa, Salvatore Rappoccio, and Daniel Sherman. Measurement of top pair production cross section in lepton plus jets events with SecVtx tags. CDF Internal Note #7536.

[77] Ben Cooper and Andrea Messina. Estimation of the background to $W \rightarrow e\nu +$ n jet events. CDF Internal Note #7760.

[78] S. Jindariani, S. Klimenko, J. Konigsberg, G. Lungu, V. Necula, L. Pinera, A. Pronko, R. Rossin, A. Sukhanov, D. Tsybychev, and S.M. Wang. Luminosity uncertainty for Run 2 up until August 2004. CDF Internal Note #7446.

[79] Young kee Kim and Un ki Yang. Initial state gluon radiation studies on Drell-Yan data for top-pair production in hadron collider. CDF Internal Note #6804.

[80] Gary J. Feldman and Robert D. Cousins. A unified approach to the classical statistical analysis of small signals. *Phys. Rev.*, D57:3873–3889, 1998.

[81] F. James and M. Roos. MINUIT: A system for function minimization and analysis of the parameter errors and correlations. *Comput. Phys. Commun.*, 10:343–367, 1975.

[82] T. Akimoto et al. Measurement of the Z production cross-section in the tau channel. CDF Internal Note #7589.

[83] S. Baroiant et al. Update on the lepton + track trigger in Run II - definition and physics goals. CDF Internal Note #6325.

[84] S. Baroiant et al. Lepton+track triggers: Measurement of the Level 3 trigger efficiency for taus. CDF Internal Note #6553.